EXPERIMENTAL STUDY OF GAS TURBINE BLADE FILM COOLING AND INTERNAL TURBULATED HEAT TRANSFER AT LARGE REYNOLDS NUMBERS

A Dissertation

by

SHANTANU MHETRAS

Submitted to the Office of Graduate Studies of
Texas A&M University
in partial fulfillment of the requirements for the degree of

DOCTOR OF PHILOSOPHY

August 2006

Major Subject: Mechanical Engineering

EXPERIMENTAL STUDY OF GAS TURBINE BLADE FILM COOLING AND INTERNAL TURBULATED HEAT TRANSFER AT LARGE REYNOLDS NUMBERS

A Dissertation

by

SHANTANU MHETRAS

Submitted to the Office of Graduate Studies of
Texas A&M University
in partial fulfillment of the requirements for the degree of

DOCTOR OF PHILOSOPHY

Approved by:

Chair of Committee,	Je-Chin Han
Committee Members,	Sai C. Lau
	Gerald L. Morrison
	Hamn-Ching Chen
Head of Department,	Dennis O'Neal

August 2006

Major Subject: Mechanical Engineering

ABSTRACT

Experimental Study of Gas Turbine Blade Film Cooling and Internal Turbulated Heat Transfer at
Large Reynolds Numbers. (August 2006)
Shantanu Mhetras, B.E., University of Mumbai, India;
M.S., Texas A&M University
Chair of Advisory Committee: Dr. Je-Chin Han

Film cooling effectiveness on a gas turbine blade tip on the near tip pressure side and on the squealer cavity floor is investigated. Optimal arrangement of film cooling holes, effect of a full squealer and a cutback squealer, varying blowing ratios and squealer cavity depth are also examined on film cooling effectiveness. The film-cooling effectiveness distributions are measured on the blade tip, near tip pressure side and the inner pressure and suction side rim walls using a Pressure Sensitive Paint (PSP) technique. A blowing ratio of 1.0 is found to give best results on the pressure side whereas the other tip surfaces give best results for blowing ratios of 2. Film cooling effectiveness tests are also performed on the span of a fully-cooled high pressure turbine blade in a 5 bladed linear cascade using the PSP technique. Film cooling effectiveness over the entire blade region is determined from full coverage film cooling, showerhead cooling and from each individual row with and without an upstream wake. The effect of superposition of film cooling effectiveness from each individual row is then compared with full coverage film cooling. Results show that an upstream wake can result in lower film cooling effectiveness on the blade. Effectiveness magnitudes from superposition of effectiveness data from individual rows are comparable with that from full coverage film cooling.

Internal heat transfer measurements are also performed in a high aspect ratio channel and from jet array impingement on a turbulated target wall at large Reynolds numbers. For the channel, three dimple and one discrete rib configurations are tested on one of the wide walls for Reynolds numbers up to 1.3 million. The presence of a turbulated wall and its effect on heat transfer enhancement against a smooth surface is investigated. Heat transfer enhancement is found to decrease at high Re with the discrete rib configurations providing the best enhancement but highest pressure losses. Experiments to investigate heat transfer and pressure loss from jet array impingement are also performed on the target wall at Reynolds numbers up to 450,000. The heat transfer from a turbulated target wall and two jet plates is investigated. A target wall with short pins provides the best heat transfer with the dimpled target wall giving the lowest heat transfer among the three geometries studied.

ACKNOWLEDGMENTS

I would like to express my sincere appreciation to Dr. J. C. Han for his guidance and sharing of his expertise in my 4 years as a Research Assistant in his group. I have learned innumerable things from him and I hope to continue receiving guidance from him in my future career. I would also like to thank Dr. S. C. Lau, Dr. G. L. Morrison, and Dr. H. C. Chen for giving their precious time on the advisory committee. Their advice and suggestions are greatly appreciated. Part of my research was supported by Siemens Power Generation, Inc. and I would also like to extend my sincere thanks towards their heat transfer group.

Acknowledgments are due to my colleagues from the Turbine Heat Transfer Laboratory and TURBOLAB. It was a pleasure to know and to work with everybody and I hope I can keep in touch with them in the future. Special thanks are due to Mr. Eddie Denk for his advice and help without which I would not have been able to achieve my goals.

Finally, I want to thank my parents, Prakash Mhetras and Neeta Mhetras, my sister, Puja Maji, and my fiancé Sunila Churi for their continual support and patience.

NOMENCLATURE

A	Area [m^2]
c_p	Specific heat of air [J/(kg.K)]
C_D	Discharge Coefficient
C	Oxygen Concentration
C_x	Axial chord length of the blade
d	Diameter of film-cooling holes
D_h	Hydraulic diameter of the channel [0.142m]
Δp	Pressure drop [N/m^2]
f	Friction factor
h	Regional heat transfer coefficient [$W/(m^2.K)$]
H	Blade span
I	Pixel intensity for an image
I_{ph}	Phase current supplied to the heaters [A]
k	Thermal conductivity [W/(m.K)]
K	Loss Coefficient
M	Blowing ratio ($=\rho_c V_c / \rho_m V_m$)
Ma	Mach number
M_i	Local blowing ratio ($=\rho_{c,local} V_{c,local} / \rho_{m,local} V_{m,local}$)
Nu	Nusselt number
P	Local static pressure
Pr	Prandtl Number
P_t	Total pressure
P_{O_2}	Partial pressure of oxygen
q"	Heat flux [W/m^2]
Re	Reynolds number
s	Distance between adjacent holes in a hole row (= 5.3mm)
s_{eq}	Equivalent slot width for hole row ($= 22\left(\pi d^2/4\right)/H$)
T	Temperature (°C)
Tu	Turbulence intensity level at the cascade inlet

x	Distance (cm)
x_{arc}	Surface distance measured from blade stagnation (cm)
V	Velocity (m/s)
$\overline{V}$	Mean velocity [m/s]
V_{ph}	Phase voltage across the heaters [V]
y	Distance along blade span measured from hub (cm)
η	Local film-cooling effectiveness
ρ	Density of coolant air (kg/m^3)
μ	Dynamic viscosity of air [kg/ms]

Subscript

0	reference, fully developed turbulent flow in a smooth tube
air	mainstream air with air as coolant
aw	adiabatic wall
b	bulk mean
blk	image without illumination (black)
c	coolant
cond	conduction
f	film
i,j	location
loss	loss to the surroundings through insulation
m	mainstream
mix	mainstream air with nitrogen as coolant
ref	reference image with no mainstream and coolant flow
s	superposition
w	wall

Acronyms

LE	Leading edge of the blade
PS	Pressure side
SS	Suction side
ST	Stagnation

TABLE OF CONTENTS

Page

LIST OF FIGURES

Page

Page

1. INTRODUCTION

Film cooling on the blade tip and span is investigated for a typical gas turbine blade in the present study. Internal heat transfer measurements are also performed in a high aspect ratio channel and from jet array impingement on a turbulated target wall. Thus, the present study is divided into four parts.

Film cooling effectiveness on a gas turbine blade tip from shaped holes on the near tip pressure side and cylindrical holes on the squealer cavity floor is investigated. Effect of a full squealer and a cutback squealer is examined with two blade geometries. Optimal arrangement of film cooling holes is investigated. Effects of varying blowing ratios and squealer cavity depth are also examined on film cooling effectiveness. The film-cooling effectiveness distributions are measured on the blade tip, near tip pressure side and the inner pressure side and suction side rim walls using Pressure Sensitive Paint technique. The internal coolant-supply passages of the squealer tipped blade are modeled similar to those in the GE-E^3 rotor blade with two separate serpentine loops supplying coolant to the film cooling holes. Cylindrical film cooling holes are used on the tip cavity floor while another row of shaped film cooling holes is arranged along the pressure side just below the tip. The average blowing ratio of the cooling gas is controlled to be 0.5, 1.0, 1.5 and 2.0. A blowing ratio of 1.0 is found to give best results on the pressure side whereas the other tip surfaces give best results for $M = 2$. A smaller squealer depth causes the average effectiveness magnitudes to decrease slightly.

Film cooling effectiveness on the span of a fully-cooled high pressure turbine blade in a 5 bladed linear cascade on film cooling effectiveness is studied using the Pressure Sensitive Paint (PSP) technique. Effect of showerhead injection at the leading edge and the presence of compound angled, cylindrical holes on the pressure and suction side are also examined. Four rows of compound angled film cooling holes are provided on the pressure side while two such rows are provided on the suction side of the blade. Another three rows of holes are drilled at 30^o to the surface on the leading edge to capture the effect of showerhead film coolant injection.

This dissertation follows the style of ASME Journal of Heat Transfer.

The coolant is injected at different average blowing ratios ranging from 0.3 to 1.5. Film cooling effectiveness over the entire blade region is determined from full coverage film cooling with coolant blowing from all rows and from each individual row. The effect of superposition of film cooling effectiveness from each individual row is then compared with full coverage film cooling. Showerhead cooling is also studied. Presence of wake due to an upstream vane is studied by placing a periodic set of rods upstream of the test blade. The stationary wake is controlled by using two different rod diameters of 3.2mm and 4.8mm. Effect of wake is recorded at four phase locations with equal intervals. Results show that the presence of a stationary upstream wake can result in lower film cooling effectiveness on the blade especially on the suction side of the blade. Varying blowing ratios can have a significant impact on film-cooling effectiveness distribution with a blowing ratio of 0.9 showing highest effectiveness. Results also show that the effectiveness magnitudes from superposition of effectiveness data from individual rows are comparable with that from full coverage film cooling.

Experiments to investigate heat transfer and pressure loss are also performed in a rectangular channel with an aspect ratio of 6 at very high Reynolds numbers under compressible flow conditions. Reynolds numbers upto 1.3 million are tested. The presence of a turbulated wall and its effect on heat transfer enhancement against a smooth surface is investigated. Three dimpled configurations including spherical and cylindrical dimples are studied on one wide wall of the channel. The presence of discrete ribs on the same wide wall is also investigated. A steady state heat transfer measurement method is used to obtain the heat transfer coefficients while pressure taps located at several streamwise locations in the channel walls are used to record the static pressures on the surface. Experiments are performed for a range of Reynolds numbers from 60,000 to 1,300,000 to cover the incompressible as well as compressible flow regimes. Heat transfer enhancement is found to decrease at high Re with the discrete rib configurations providing the best enhancement but highest pressure losses. Local measurements using the steady state, hue-detection based liquid crystal technique are also performed in the fully developed region for case 1 with dimples. Good comparison is obtained between averaged local heat transfer coefficient measurements and from thermocouple measurements.

In the fourth part of this study, experiments to investigate heat transfer and pressure loss from jet array impingement are performed on the target wall at high Reynolds numbers. Reynolds numbers upto 450,000 are tested. The presence of a turbulated target wall and its effect on heat transfer enhancement against a smooth surface is investigated. Two different jet plate configurations are used with closely spaced holes and with angled as well as normal impingement holes. Heat transfer and pressure loss measurements are performed on a smooth target wall as well as turbulated target walls. Three turbulators configurations are used with streamwise riblets, short pins and spherical dimples. A steady state heat transfer measurement method is used to obtain the heat transfer coefficients while pressure taps located in the plenum and at several streamwise locations are used to record the pressure losses across the jet plate. Experiments are performed for a range of Reynolds numbers from 50,000 to 450,000 based on average jet hole diameters. A target wall with short pins provides the best heat transfer with the dimpled target wall giving the lowest heat transfer among the three turbulators geometries studied.

2. TURBINE BLADE TIP FILM COOLING

2.1. INTRODUCTION

The concept of cooling a surface subjected to high mainstream temperatures by perforating the surface with several discrete holes and passing cold air (film-cooling) through them is a popular technique used in several applications. The surface under test can be maintained at a cooler temperature due to formation of a thin protective film of relatively colder air on the surface. This technique has been successfully employed for cooling of gas turbine blades subjected to very high mainstream gas temperatures. A high and uniform film-cooling effectiveness on the blade surface will ensure superior performance and thermal fatigue life for the blade, thus making it an important parameter in its design. Hot gases from the combustor enter the turbine, resulting in a significant heat load on the turbine components. One of the components more susceptible to thermal failure is the blade tip region due to its severe environment and difficulty in cooling. Large leakage flow occurs on the tip due to a high pressure differential from pressure to suction side. This leakage mass flow can be reduced by using a labyrinth-like recessed cavity also known as the squealer tip. Presence of film cooling on the tip further reduces heat transfer from the mainstream gas to the blade tip. A comprehensive compilation of the available film cooling techniques used in the Gas Turbine industry has been encapsulated by Han et al. [1].

Experimental investigations performed in the general area of film-cooling on a blade tip are limited with few papers available in open literature. Film cooling on a blade tip was first studied by Kim and Metzger [2] and Kim et al. [3] by using a 2-D rectangular tip model to simulate leakage flow between the tip and the shroud. Various film-cooling configurations were examined using a transient liquid crystal technique and the results for heat transfer coefficients and film-cooling effectiveness were reported. Kwak and Han [4,5] studied the local heat transfer distribution and film-cooling effectiveness using hue detection based transient liquid crystal technique on the blade tip for plane and squealer tip geometry. A GE-E^3, 5-blade linear cascade was used similar to the one used in the present paper. They used three tip gap clearances (1.0%, 1.5% and 2.5% of blade span) along with three average blowing ratios (0.5, 1.0 and 2.0) for the coolant. Increasing blowing ratio increased film effectiveness but overall heat transfer coefficients decreased. Their results also showed that the squealer geometry showed higher film cooling effectiveness and lower heat transfer coefficients compared to the plane tip geometry due to its smaller leakage flow.

Ahn et al. [6] presented film cooling effectiveness results using the PSP technique on a plane and squealer blade tip with one row of holes on the camber line and another row of angled holes near the pressure side tip. They used the same high flow cascade as the present study and investigated the effects of tip gap clearance (1.0%, 1.5% & 2.5% blade span) and blowing ratio (M = 0.5, 1 & 2). They noted that higher blowing ratios give higher effectiveness. Results with plane tip showed clear traces of the coolant path while for squealer tip, coolant accumulation effects were observed on the cavity floor. Christophel et al. [7,8] studied film cooling and heat transfer using the infrared technique on a plane tip under low speed conditions. They used four different coolant flow rates (0.47%, 0.58%, 0.68% and 1.0% passage flow) for two tip gaps. A row of holes was located on the pressure side just below the tip with two more dirt purge holes on the tip itself. They found that a smaller tip gap and larger coolant flow showed better cooling. They also found that higher blowing ratios resulted in higher augmentations on tip heat transfer but with an overall net heat flux reduction when combined with adiabatic effectiveness measurements. Mhetras et al. [9] studied film cooling effectiveness on all surfaces of a squealer tipped blade in a linear high flow cascade using the PSP technique. Coolant was injected through shaped holes near the pressure side similar to the present study and cylindrical holes on the cavity floor. The shaped holes on the pressure side near the tip showed a large coolant spread consequently resulting in good film coverage. The coolant from the tip holes was directed towards the pressure side inner squealer rim wall to provide additional cooling.

Some experimental investigations have also been performed to study heat transfer on the blade tip under rotating conditions. Heat transfer coefficients on the blade tip and the shroud were measured by Metzger et al. [10] using heat flux sensors in a rotating turbine rig. Dunn and Haldeman [11] measured time-averaged heat flux at a recessed blade tip for a full-scale rotating turbine stage at transonic vane exit conditions. Their results showed that the heat transfer coefficient at the mid and rear portion of the cavity floor is of the same order as the blade leading edge value. A recent study by Rhee and Cho [12, 13] investigated the mass transfer characteristics for a flat tip on the tip, shroud and near tip regions. Heat transfer on the tip under rotating conditions was found to be about 10% lower than the stationary case due to relative motion between the shroud and tip.

There are many papers available in open literature, which discuss heat transfer coefficients on the blade tip and near tip regions. Several of these papers present results under engine representative mainstream flow conditions. Local heat transfer coefficients on a turbine blade tip model with a recessed cavity (squealer tip) were studied by Yang and Diller [14] in a stationary transonic linear cascade. Bunker et al. [15] utilized a hue detection based liquid crystal technique to obtain local heat transfer distributions on a plane blade tip in a stationary cascade. They studied the effects of tip gap clearance and free-stream turbulence intensity levels. Azad et al. [16,17] used transient liquid crystal technique to study heat transfer. They compared squealer tip and plane tip geometry and concluded that the overall heat transfer coefficients were lower for squealer tip case. Bunker and Bailey [18] studied the effect of squealer cavity depth and oxidation on turbine blade tip heat transfer. Azad et al. [19] and Kwak et al. [20] investigated the heat transfer on several different squealer geometries. A suction side squealer tip was found to give the lowest heat transfer among all cases studied. Heat transfer coefficient distributions for plane and squealer tip and near tip regions were presented by Kwak and Han [21, 22] in two papers. By using a squealer tip, heat transfer was found to decrease on the tip and near tip regions.

A few of the many papers on blade tip heat/mass transfer performed under low speed conditions are also discussed. Investigations comparing a rotating and stationary shroud were performed by Mayle and Metzger [23]. They noted that the effect of shroud rotation could be neglected to measure the blade tip heat transfer over the entire range of parameters considered in the study. Heyes et al. [24] studied tip leakage flow on plane and squealer tips in a linear cascade and concluded that the use of a squealer tip, especially a suction-side squealer tip, was more beneficial than a flat tip. Heat transfer coefficients and static pressure distributions of a large-scale turbine blade tip were measured by Teng et al. [25] in a low-speed wind tunnel facility using a transient liquid crystal technique. Mass transfer technique was used by Papa et al. [26] to study local and average mass/heat transfer distributions on a squealer tip and winglet-squealer tip in a low-speed wind tunnel. Jin and Goldstein [27, 28] also used this technique on a simulated high-pressure turbine blade tip and near tip surfaces. They observed that the average mass transfer from the tip surface was much higher than that on pressure and suction side surfaces. Saxena et al. [29] investigated the effect of various tip sealing geometries on blade tip leakage flow and heat transfer of a scaled up HP turbine blade in a low-speed wind tunnel facility using a steady state HSI-based liquid crystal technique. They noted that the trip strips placed against the leakage flow produce the lowest heat transfer on the tips compared to all the other cases.

Some numerical investigations have also been carried out to study heat transfer and film-cooling effectiveness on blade tip. Effects of tip clearance and casing recess on heat transfer and stage efficiency for several squealer blade tip geometries were predicted by Ameri et al. [30]. Ameri and Rigby [31] also calculated heat transfer coefficients and film-cooling effectiveness on turbine blade models. Numerical results for heat transfer and flow obtained by Ameri et al. [32] were compared to the experimental results from Bunker et al. [15] for a power generation gas turbine.

Numerical techniques were also utilized by Yang et al. [33,34] to study flow and heat transfer past a turbine blade with plane and squealer tip. Film-cooling effectiveness for a flat and squealer blade tip with film cooling holes on tip pressure side were predicted by Acharya et al. [35]. Hohlfeld et al. [36] predicted film-cooling flow from dirt purge holes on a turbine blade tip. They found that the flow exiting the dirt purge holes helped in blocking the leakage flow across the gap. As the blowing ratio increased for a large tip gap, tip cooling increased only slightly whereas film cooling on the shroud increased significantly. Effects of different hole locations on film-cooling effectiveness and heat transfer were predicted by Yang et al. [37].

The main focus of the present study was to investigate the film cooling effectiveness from pressure side and tip injection on a cutback squealer tipped blade. Film cooling on the squealer rim walls and the squealer cavity floor was determined at two different cavity depths. Currently, no data is available in open literature for film cooling effectiveness on the pressure side outer and inner rim walls. Heat transfer data is also limited in this region mainly due to large experimental uncertainty because of heat conduction errors in the thin rim wall. Two blade designs were used to optimize the arrangement of film cooling holes and to maximize film coverage. Blade 1 employed a full squealer on the tip whereas in blade 2, the pressure side rim wall near the trailing edge was removed to allow accumulated coolant in the squealer cavity to escape and cool the trailing edge tip region. The combined effect of the above mentioned designs were tested under relatively high flow conditions. By maximizing film cooling coverage, contact of the hot gases with the squealer tip surfaces can be reduced thus reducing the

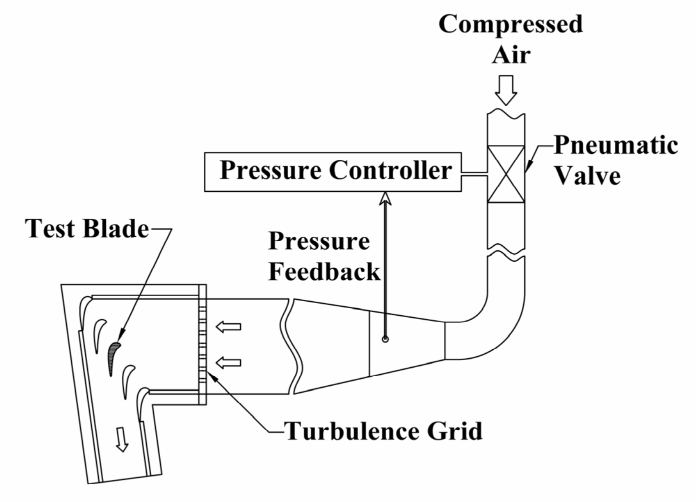

Fig. 2.1 Schematic of test section and blowdown facility

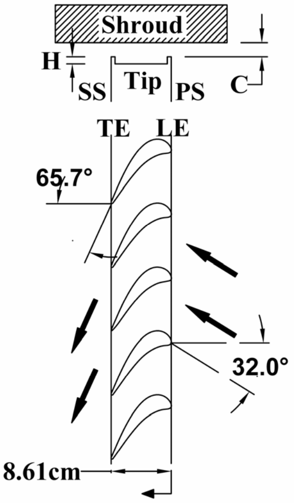

Fig. 2.2 Definition of blade tip and shroud

blade metal temperature. This will prevent blade tip oxidation as well as marginally reduce the heat flux into the blade.

A scaled up blade tip model of a first stage rotor blade (GE-E^3) of a modern aircraft gas turbine was used in this study, with a row of 9 shaped film cooling holes on the near tip pressure side and another set of 10 cylindrical holes on the cavity floor. The hole location, shape, orientation and internal coolant flow path is different from Ahn et al. [6] and much closer to a real gas turbine blade tip design. Film cooling effectiveness was studied on the rim, cavity floor, inner cavity walls and the near tip pressure side. Moreover, the PSP technique is based on mass transfer analogy, which eliminates any heating/conduction errors present in other optical measurement techniques such as liquid crystal and IR camera. The experimental results for pressure and effectiveness will aid future engineers to design more efficient turbine blades and help to calibrate CFD codes.

2.2. EXPERIMENTAL SETUP

The test section consisted of a 5-blade linear cascade with blade tip profiles placed in a blow-down loop. A schematic of the test section and the blow-down loop is shown in Figure 2.1. Inlet cross-section of the test section was 31.1cm (width) x 12.2cm (height). A turbulence-generating grid (rectangular bar mesh type) with a porosity of 57% was placed before the inlet. Turbulence intensity was recorded 6cm upstream of the middle blade (or 20.7cm downstream of the grid) using a hot-wire probe. Turbulence intensity (Tu) at this location was found to be 9.7% due to the presence of the grid and turbulence length scales were estimated to be 1.5cm, which is slightly larger than the grid bar size. The bottom and sides on the test section were machined out of 1.27cm thick polycarbonate sheets whereas a 1.27cm thick acrylic plate was used for the top for better optical access to the blade tip. The top plate also acted as a shroud for the blades. Flow conditions in adjacent passages of the center blade were ensured to be identical by adjusting the trailing edge tailboards for the cascade. A comprehensive discussion on the flow conditions, including flow periodicity in the cascade and pressure distribution along the blade has been reported by Azad et al. [16, 17] and Kwak and Han [20, 21].

During the blow-down test, the cascade inlet air velocity and exit velocity were 78 m/s and 220 m/s respectively. The Reynolds number based on the axial chord length and exit velocity was $1.48\text{x}10^6$. Overall pressure ratio (P_t/P) was 1.29 (where P_t is inlet total pressure and P is exit static pressure) and inlet and exit Mach numbers were 0.23 and 0.65 respectively. The blow-down facility could maintain steady flow in the cascade for about 40 seconds. Compressed air stored in tanks entered a high flow pneumatic control valve, which could maintain steady flow by receiving downstream pressure feedback. The control valve could maintain a velocity within ± 3% of desired value.

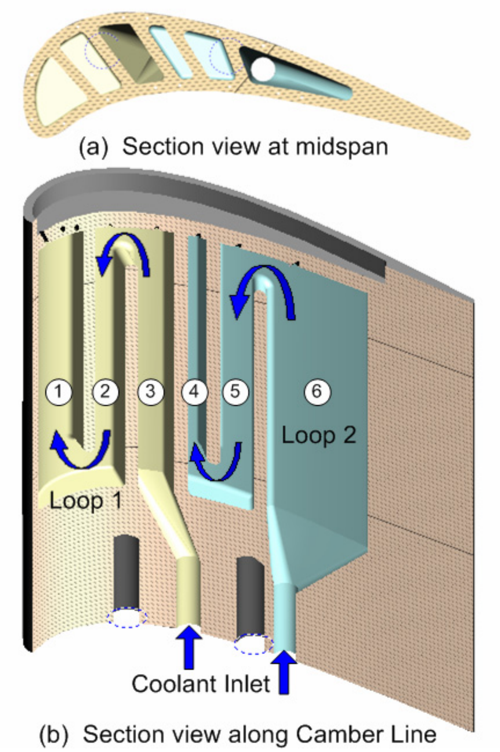

Fig. 2.3 Internal passage geometry of test blade

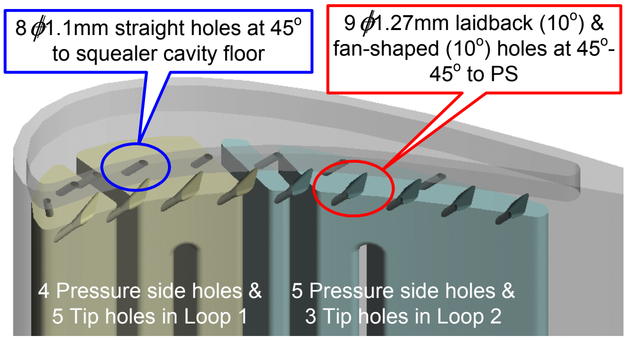

Fig. 2.4 Orientation of tip and PS holes for blade 1

A 3X scaled model of the GE-E^3 blade was used with a blade span of 12.2cm and an axial chord length of 8.61cm. Since the blades were placed in a linear cascade, they were machined for a constant cross-section for its entire span corresponding to the tip profile of the actual GE-E^3 blade. Figure 2.2 shows the blade profiles, the inlet and exit angles for air and the blade tip and shroud definitions. The test blade was made using Stereo lithography (SLA) as conventional

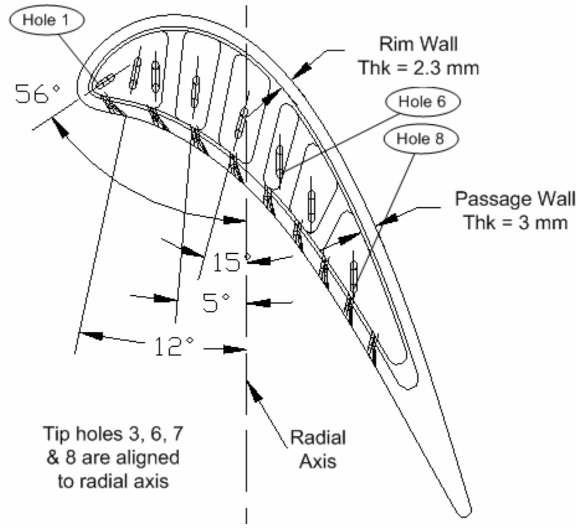

Fig. 2.5 Tip hole orientation for blade 1

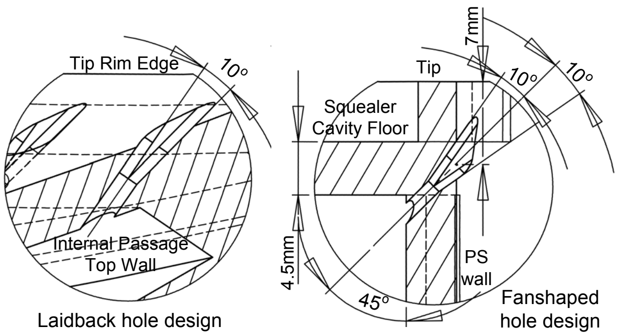

Fig. 2.6 Detail geometry of a PS shaped hole for blade 1

machining methods were unsuitable for such a complicated geometry. The four guide blades placed in the test section were made of aluminum. Figure 2.3 shows the film-cooling measurement blade with the internal passage geometry. The passages are numbered from 1 to 6 with passage 1 closest to leading edge and passage 6 closest to trailing edge. Coolant was supplied to the test blade through two loops with three serpentine passages with a 3mm wall thickness in each loop as shown. The design of the passages was based on the E^3, stage 1, HPT rotor blade cooling system as discussed by Halila et al. [38]. The leading edge impingement wall in their design was removed to simplify the passage flow analysis.

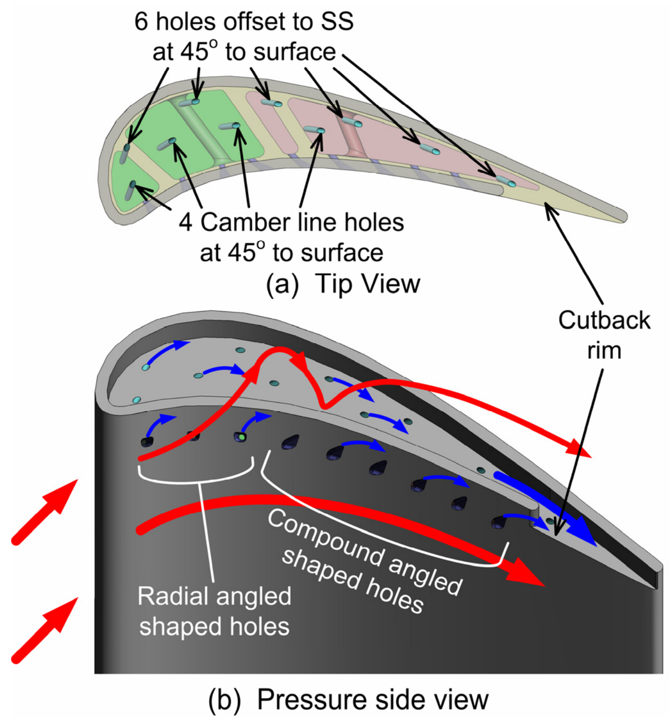

Fig. 2.7 Orientation of tip and PS holes for blade 2

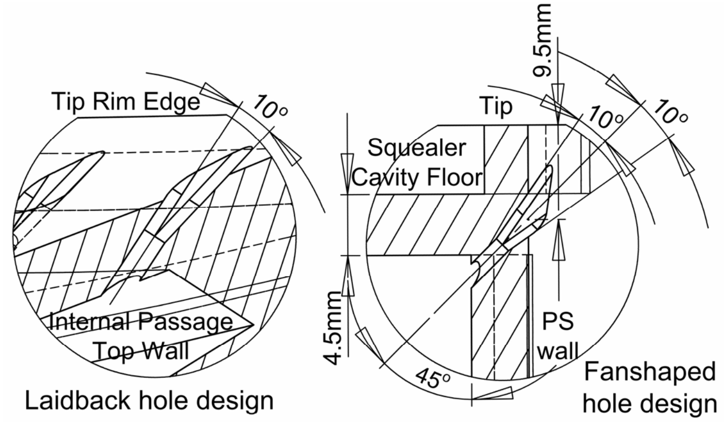

Fig. 2.8 Detail geometry of a PS shaped hole for blade 2

Figure 2.4 shows the geometry and orientation of the film cooling holes on the pressure side and on the squealer blade tip for blade 1. Eight cylindrical tip holes with a diameter of 1.1 mm (L/d = 5.78) were provided on the tip such that they break out along the camber line of the blade on the internal passage top wall. The thickness of the wall between the internal passages and the cavity floor was 0.45cm. Figure 2.5 shows tip hole orientation with respect to the radial axis. The first tip hole near the leading edge was drilled at 60° to the cavity floor giving a length of diameter ratio (L/d) of 4.7. The remaining 7 holes were drilled at 45^o to the cavity floor with an L/d = 5.8. The angles with respect to the radial axis are shown in Fig. 2.5. The location and arrangement of the tip holes was similar to that described by Halila et al. [38] for the HPT rotor blade. The first 5 tip holes were connected to loop 1 (near LE) and the remaining three to loop 2 (near TE). Nine film-cooling holes with a diameter of 1.27 mm and a hole spacing of 0.89 cm were provided for coolant to pass through on the airfoil pressure side. The pressure side holes were located 0.7 cm below the tip surface at a compound angle of 45^o to the blade span and 45^o with respect to the airfoil pressure surface with L/d = 4. Figure 2.6 shows the detail views of the shaped holes. A laidback and fan-shaped design was employed for these 9 holes with the holes expanding by 10^o in the three directions (10-10-10) with the expansion starting from the middle of the hole length.

Figure 2.7 shows the geometry and orientation of the film cooling holes on the pressure side and on the squealer blade tip for blade 2. Ten cylindrical tip holes with a diameter of 1.27 mm (L/d = 3.34) were provided on the tip. Out of these 10 holes, four were drilled such that they break out at 45^o along the camber line of the blade on the cavity floor. The remaining six holes were drilled at 45^o along a curve offset to the suction surface of the blade by 5.08mm and were equally spaced by 18.3mm. The holes were inclined to the cavity floor in the direction of the bulk fluid flow. The first 5 tip holes were connected to loop 1 (near LE) and the remaining five to loop 2 (near TE). Nine film-cooling holes with a diameter of 1.27 mm were provided for coolant to pass through on the airfoil pressure side. The pressure side holes have a laidback and fan-shaped design expanding by 10^o in the three directions (10-10-10) with the expansion starting from the middle of the hole length and were located 9.5mm below the tip surface with a hole-to-hole spacing of 8.9mm. This design is similar to the design used in blade 1. The first three holes near the leading edge were drilled at a radial angle of 45^o to maximize the coolant spread whereas the remaining six holes were drilled at a compound angle of 45^o to the blade span and 45^o with respect to the airfoil pressure surface with L/d = 4. Figure 2.8 shows the detailed views of the shaped holes. All 9 holes on the near tip pressure side in blade 1 were drilled at a compound angle of 45^o. Coolant to the first four holes was supplied through loop 1 while the remaining 5 holes were connected to loop 2. Two squealer tipped blades with same hole geometry but with recesses of 4.2% and 2.1% of blade span were used to investigate the effect of cavity depth. The pressure side rim wall near the trailing edge is cutback by about 20% of the blade chord for both blades to allow accumulated coolant to escape.

This study was performed for a tip gap of 1.5% of blade span (12.2cm), which was maintained on the middle three blades. Coolant injection through tip and pressure side holes (TP) as well as pressure side holes (P) only was studied. Experiments were performed with four different average blowing ratios (M) of 0.5, 1.0, 1.5 and 2.0. The blowing ratio was defined as $M = \rho_c V_c / \rho_m V_m$. If the density is same, the ratio is reduced to a velocity ratio. During testing, it was observed that the leakage flow velocity could vary from hole-to-hole on the tip and near tip surfaces. The mainstream mass flux at each hole location was measured locally by static pressure measurement from PSP on the tip surface and pressure taps on the near tip pressure surface. The coolant mass flow for all holes was determined for a particular blowing ratio from the local mainstream mass flux and the coolant flow rate for each loop was set by adding the coolant mass flows for each individual open hole in that loop.

2.3. FILM-COOLING EFFECTIVENESS MEASUREMENT THEORY AND DATA ANALYSIS

Data for film cooling effectiveness was obtained by using the PSP technique. PSP is a photo-luminescent material which emits light when excited, with the emitted light intensity inversely proportional to the partial pressure of oxygen. This light intensity can be recorded using a CCD camera and can then be calibrated against the partial pressure of oxygen. Details of using PSP for pressure measurement are given in McLachlan and Bell [39]. The image intensity obtained from PSP by the camera during data acquisition is normalized with a reference image intensity taken under no-flow conditions. Background noise in the optical setup is removed by subtracting the image intensities with the image intensity obtained under no-flow conditions and without excitation. The resulting intensity ratio can be converted to pressure ratio using the pre-determined calibration curve and can be expressed as:

$$\frac{I_{ref} - I_{blk}}{I - I_{blk}} = f\left(\frac{\left(P_{O_2}\right)_{air}}{\left(P_{O_2}\right)_{ref}}\right) = f\left(P_{ratio}\right) \tag{2.1}$$

where I denotes the intensity obtained for each pixel and $f\,(P_{ratio})$ is the relationship between intensity ratio and pressure ratio obtained after calibrating the PSP.

Calibration for PSP was performed using a vacuum chamber at several known pressures varying from 0 to 1.8atm with intensity recorded for each pressure setting. The calibration curve is shown in Fig. 2.9. The same optical setup was chosen for calibration as well as for data acquisition during the experiments. PSP is sensitive to temperature with higher temperatures resulting in lower emitted light intensities. Hence, the paint was also calibrated for different temperatures. It was observed that if the emitted light intensity at a certain temperature was normalized with the reference image intensity taken at the same temperature, the temperature sensitivity can be minimized. During testing, it was ensured that temperatures of mainstream air, coolant and test section were same while taking reference, air and nitrogen images to minimize uncertainty. Thermocouples (T-type) located upstream of the test section and in the coolant flow recorded temperatures of air and nitrogen gas. Experiments were conducted in an air-conditioned room (20^{o}C) and temperatures of mainstream air, coolant air and nitrogen gas were maintained at 20^{o}C.

To obtain film cooling effectiveness, air and nitrogen were used alternately as coolant. Nitrogen which has nearly the same molecular weight as that of air displaces the oxygen molecules on the surface causing a change in the emitted light intensity from PSP. By noting the difference in partial pressure between the air and nitrogen injection cases, the film cooling effectiveness can be determined using the following equation.

$$\eta = \frac{C_{mix} - C_{air}}{C_{N_2} - C_{air}} = \frac{C_{air} - C_{mix}}{C_{air}} = \frac{\left(P_{O_2}\right)_{air} - \left(P_{O_2}\right)_{mix}}{\left(P_{O_2}\right)_{air}} \tag{2.2}$$

where C_{air}, C_{mix} and C_{N2} are the oxygen concentrations of mainstream air, air/nitrogen mixture and nitrogen on the test surface respectively. The definition for film effectiveness in Eq. (2.2) based on mass transfer analogy is of similar form as that for adiabatic film cooling effectiveness given in Eq. (2.3).

$$\eta = \frac{T_{mix} - T_m}{T_c - T_m} \tag{2.3}$$

The accuracy of the PSP technique for measuring film-cooling effectiveness has been compared by Wright et al. [40] on a flat plate with compound angled ejection holes using steady-state Infra-Red (IR) technique and steady-state Temperature Sensitive Paint (TSP) technique. Results were obtained for a range of blowing ratios and show reasonable agreement with each other with IR, TSP as well as PSP giving effectiveness results within 15% of each other. Larger uncertainties for heat transfer techniques such as IR and TSP methods were observed due to lateral heat conduction in the flat plate as corrections for heat conduction were not included in the presented results.

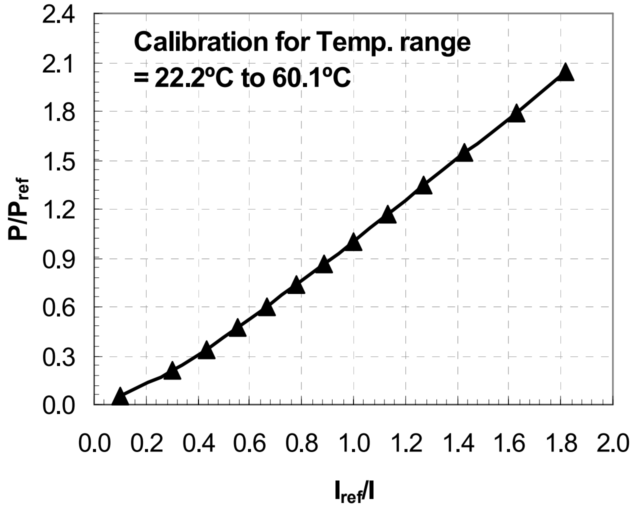

Fig. 2.9 Calibration curve for PSP

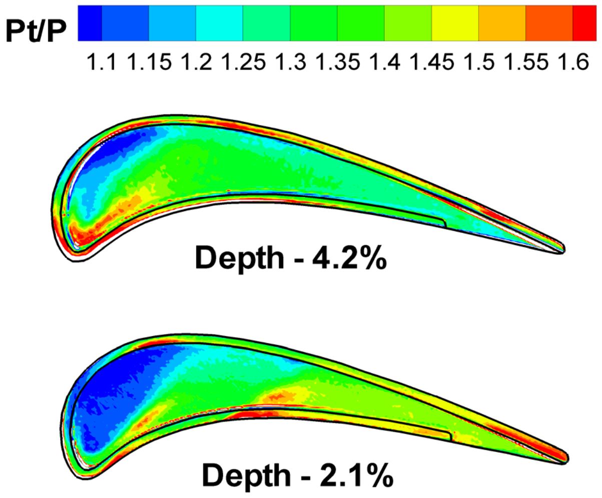

Fig. 2.10 Pressure ratio on tip

The center test blade under investigation was layered with PSP using an air brush. This coated surface was excited using a strobe light fitted with a narrow bandpass interference filter with an optical wavelength of 520nm. A dual fiber optic guide was used to get a uniform incident light distribution on the test surface. Upon excitation from this green light, the PSP coated surface emitted red light with a wavelength higher than 600nm. A 12-bit scientific grade CCD camera (Cooke Sensicam QE with CCD temperature maintained at -15^{o}C using 2-stage peltier cooler) was used to record images and was fitted with a 35mm lens and a 600nm longpass filter. The filters were chosen to prevent overlap between the wavelength ranges such that the camera filter blocked the reflected light from the illumination source. Coolant mass flow to each loop was set using two separate Rota-meters to a flow rate corresponding to the blowing ratio. A pneumatic valve was opened and the pressure controller was set to the desired flow-rate for the mainstream air. The images were taken when the mainstream flow was fully developed, i.e. after the initial developing time for flow. The camera and the strobe light were triggered simultaneously using a TTL signal from a function generator at 10 Hz. A total of 140 TIF images were captured for each experiment with air and nitrogen injection and the pixel intensity for all images was averaged. The image resolution obtained from the camera was 0.6 mm/pixel. After the images were captured, the pneumatic valve was closed. The duration of a single experiment was about 30 seconds. A computer program was used to convert these pixel intensities into pressure using the calibration curve and then into film cooling effectiveness.

Uncertainty calculations were performed based on a confidence level of 95% and are based on the uncertainty analysis method of Coleman and Steele [41]. Lower effectiveness magnitudes have higher uncertainties. For an effectiveness magnitude of 0.3, uncertainty was around ±2% while for effectiveness magnitude of 0.07, uncertainty was as high as ±10.3%. This uncertainty is the result of uncertainties in calibration (4%) and image capture (1%). The absolute uncertainty for effectiveness varied from 0.01 to 0.02 units. Thus, relative uncertainties for very low effectiveness magnitudes can be very high (>100% at effectiveness magnitude of 0.01). However, it must be noted that very few data points exist with such high relative uncertainty magnitudes. Uncertainties for the blowing ratios are estimated to be 4%.

2.4. TIP PRESSURE RATIO DISTRIBUTIONS

Figure 2.10 shows the pressure ratio (P_t/P) distributions on the blade tip for the two cavity depths tested obtained from PSP measurements. A higher pressure ratio indicates a higher surface velocity. The pressure side squealer rim acts as a backward facing step to the leakage flow causing the formation of a recirculation zone inside the squealer cavity. Flow reattachment on the tip can be observed near the leading edge from the sharp gradient in the pressure ratio distributions. As expected, the reattachment length is much shorter for a cavity depth of 2.1% resulting in a large low velocity region near the leading edge. The downstream cavity region is completely engulfed by the recirculation vortex. Higher pressure ratios can be observed on the

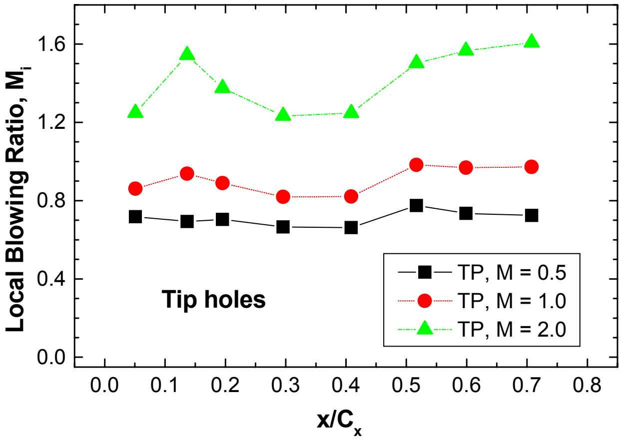

Fig. 2.11 Local M for tip holes for TP cases for blade 1

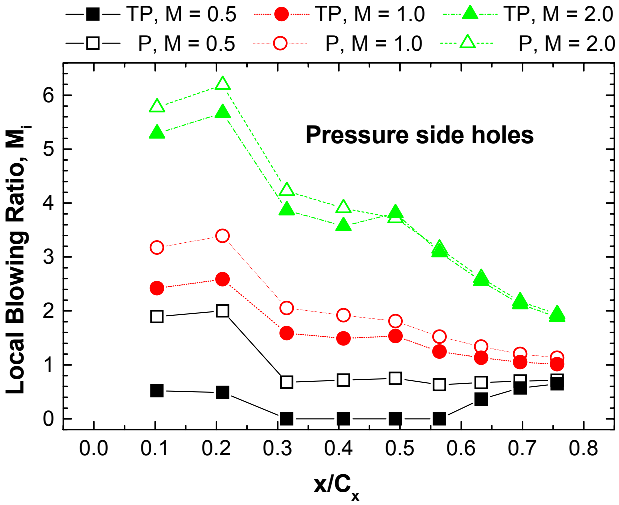

Fig. 2.12 Local M for PS holes for TP & P cases for blade 1

cavity floor towards the trailing edge for the 2.1% cavity depth indicating that the recirculation velocity is higher.

2.5. LOCAL BLOWING RATIOS

To better explain the results for effectiveness, local blowing ratios through each hole on the tip and airfoil pressure side for blade 1 have been plotted in 1.11 & 1.12 respectively. Local mass flux on the surface of the blade was found using the inlet total pressure and local static pressure. The local surface static pressure distribution for the tip was found using PSP (Fig.

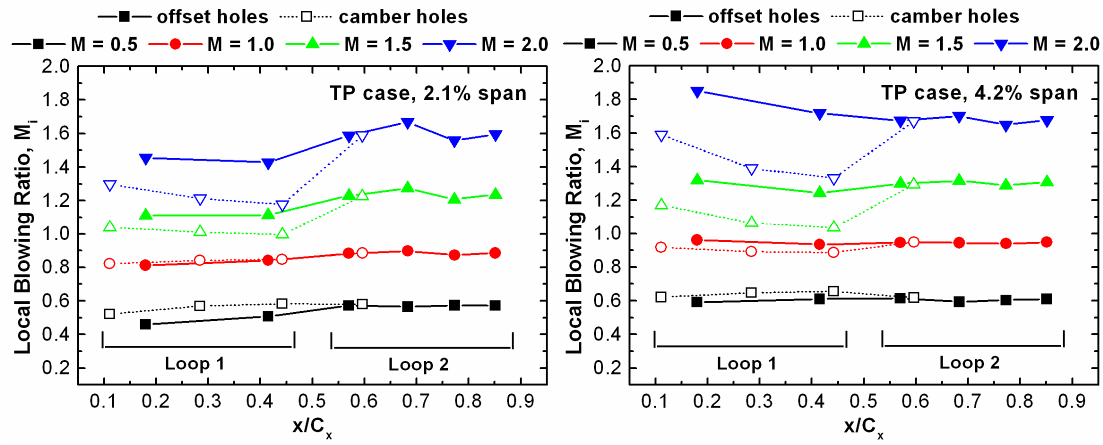

Fig. 2.13 Local M for tip holes for TP cases for 4.2% and 2.1% cavity depth for blade 2

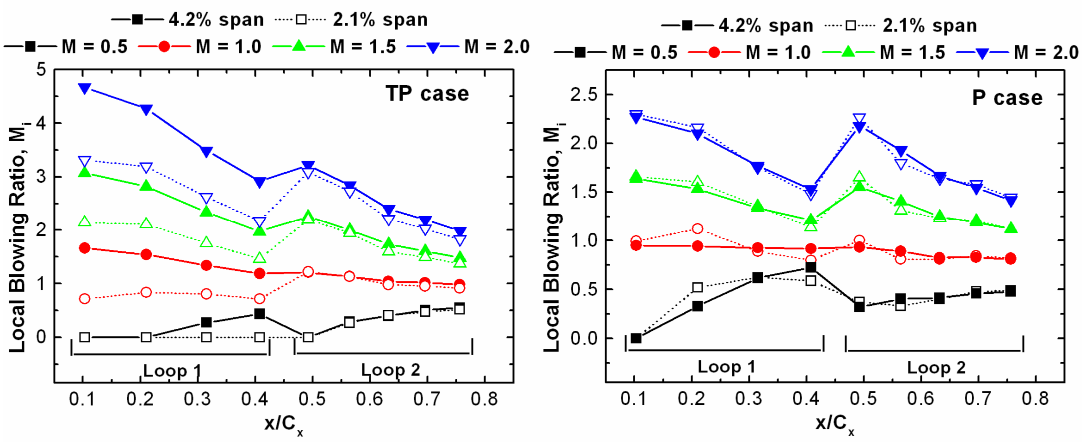

Fig. 2.14 Local M for PS holes for TP & P cases for both cavity depths for blade 2

2.10) whereas static pressure taps located at 97% of blade span were used to measure static pressure on the near tip pressure side. The static pressure in the passages inside the blade was measured using 14 static pressure taps on the pressure and suction side inner passage walls located 3.18 mm below the passage top wall. Local blowing ratio for each hole was calculated by using the pressure differential across it. A constant discharge coefficient C_D for all open holes in a loop was assumed. It should be noted that the constant C_D assumption for all holes in the loop may not be true as C_D depends on not only the geometry but also the external and internal flow conditions. By measuring the total mass flow rate of the coolant and pressure differential for each hole and using the average discharge coefficient, the coolant mass flow for each hole was determined and the local blowing ratio, M_i was calculated.

From Fig. 2.11, for coolant injection for tip holes, the blowing ratio shows a more or less uniform distribution with slightly lower values for the fourth and fifth holes. This is mainly due to lower passage pressure in the turn region from passage 3 to 2. Pressure in passage 1 closest to leading edge is higher due to stagnation of the coolant causing slightly higher local blowing ratio for tip holes 1, 2 and 3. This also results in a high local blowing ratio for the first two pressure side holes located on passage 1 as can be observed from Fig. 2.12. The local blowing ratio gradually decreases with increasing chord due to the increase in the mainstream mass flux on the pressure side as the flow approaches the throat region. A non-uniform coolant distribution exists between the tip and pressure side holes for TP cases. The average coolant mass flow per hole through the pressure side holes is higher for higher blowing ratios as compared to tip holes but at lower blowing ratios, average coolant mass flow per hole is higher for tip holes.

Local blowing ratios through each hole on the tip and airfoil pressure side of blade 2 have been plotted in Figs. 2.13 & 2.14 respectively. Figure 2.13 shows the local blowing ratios for the tip (TP cases) for both cavity depths. It can be clearly observed that the local blowing ratios for the holes along the camber line are much lower than the holes offset to the suction side for high blowing ratios. At low blowing ratios, this difference is small. A higher mainstream mass flux due to higher velocities along the camber line near the leading edge causes this uneven distribution even though the coolant mass flow rate through these holes is higher than the corresponding offset holes. The local blowing ratio distributions for both cavity depths are similar with a depth of 2.1% giving lower blowing ratios for the first few holes near the leading edge. A bigger high pressure zone as observed in Fig. 2.10 may explain this behavior. Figure 2.13 shows the local blowing ratios for the TP and P cases and for both cavity depths for the holes located on the near tip pressure side. Pressure in passage 1 closest to leading edge is higher due to stagnation of the coolant causing high local blowing ratio for the first two pressure side holes located on passage 1 as can be observed from Fig. 2.13. Similarly, the local blowing ratio for the 6th hole in loop 2 is higher than the other holes in the same loop due to stagnation inside the passage 4. The local blowing ratio gradually decreases with increasing chord due to the increase in the mainstream velocity on the pressure side as the flow approaches the throat region. A non-uniform blowing ratio distribution exists between the tip and pressure side holes for TP cases. The local M_i through the pressure side holes is higher for higher blowing ratios as compared to tip holes, but at lower blowing ratios, M_i is higher for tip holes. However, it should be noted that the average mass flow through the tip holes for all blowing ratios is higher than the pressure side holes. Local blowing ratios for the near tip pressure side holes in Fig. 2.13 for the 2.1% cavity depth are lower than that for corresponding holes for the 4.2% cavity depth for TP cases. However, the local blowing ratios for P cases for both cavity depths are almost identical as the cavity depth does not impact the upstream flow as well as the internal passage flow distributions.

2.6. FILM-COOLING EFFECTIVENESS RESULTS

Pathlines of the coolant colored with dimensionless temperature, θ obtained from numerical predictions are shown in Fig. 2.15 on the blade tip and inside the serpentine passages. Rapid change in coolant temperature can be observed as it comes into contact with the mainstream flow. The 180^{o} turning effect in the serpentine passages can also be noticed on the flow path of the coolant. Large recirculating zones can be spotted in passages 1 and 6 due to the flow orientation and their large cross-section area.

2.6.1. Blade 1 – Combined Tip and Pressure Side Coolant Injection (TP)

Figure 2.16 shows film-cooling effectiveness distribution for a squealer blade tip for coolant flow from tip as well as from the pressure side holes. The first row in the figure shows the result on the tip for the three blowing ratios of M = 0.5, 1.0 and 2.0 arranged in column-wise fashion while the second row shows the effectiveness data obtained on the near tip pressure side.

Film cooling effectiveness is found to increase with increasing blowing ratio on the tip. It can be discerned from the contour plots from Fig. 2.15 that the coolant trace from the tip holes moves towards the pressure side trailing edge. This is probably due to a recirculation zone induced by the squealer rim. Presence of this recirculation zone can be confirmed in Fig. 2.17 which shows the stream vectors of the flow as obtained from numerical predictions for M = 1 along with the dimensionless temperature, θ at three different cross-sections on the blade tip cut normal to the chord with the first cutting plane closer to the leading edge (20% chord), the second in the middle (50% chord) and the third closer to the end of the cavity near the trailing edge (65% chord). Development of the tip vortex on the suction side can also be discerned from the stream vectors. Lower temperatures due to mixing of the colder jet with the mainstream can be observed near the pressure side inner and outer rim walls implying good film coverage.

Fig. 2.15 Numerical predictions of coolant pathlines on the blade tip and inside the coolant loops colored with dimensionless temperature for blade 1

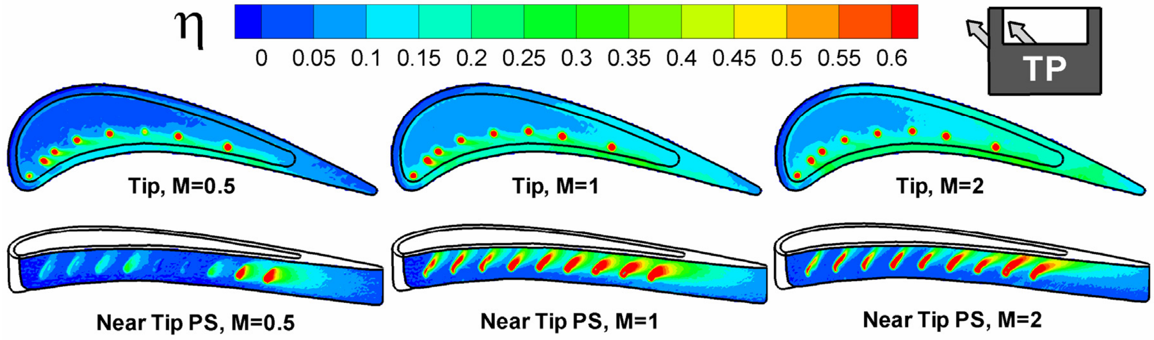

Fig. 2.16 Film cooling effectiveness distribution on tip and near tip pressure side for TP cases for blade 1

From Fig.2.16, effectiveness immediately downstream of the tip holes is very high with the magnitude dropping rapidly further downstream. Lift off of the jets can be observed for the holes on loop 2 (tip holes 5, 6, 7 and 8) for higher blowing ratios while higher effectiveness magnitudes downstream of the holes on loop 1 can be observed as the coolant jets stay closer to the cavity surface. Some coolant coverage can also be observed on the cavity floor towards the suction side/trailing edge inner rim wall. This is probably due to some coolant being trapped and re-circulated inside the squealer cavity. The pressure side rim shows relatively high

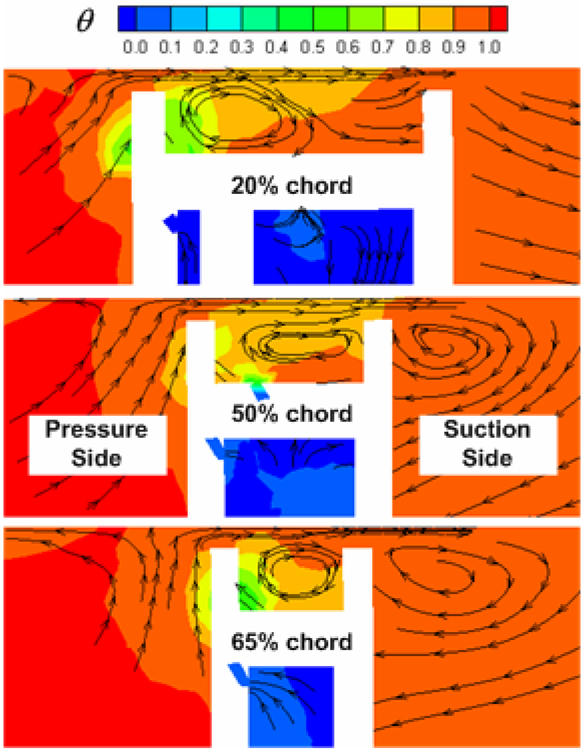

Fig 2.17 Stream vectors along with dimensionless temperature contours for 3 cross-sections along tip for blade 1

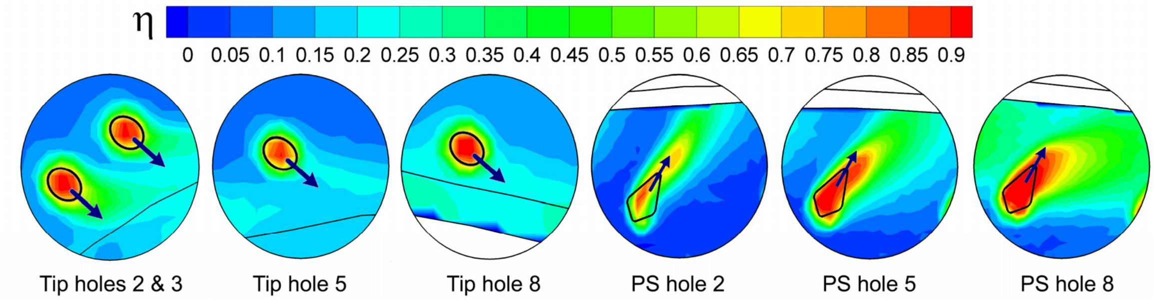

Fig. 2.18 Magnified view of effectiveness levels near some typical Tip and PS holes for M = 1 for TP case for blade 1

effectiveness magnitudes as a result of carry over of the pressure side coolant. Some coolant shooting from the tip holes for high blowing ratios may also penetrate the mainstream leakage flow to provide additional film coverage on the pressure side rim. Some traces can also be observed near the trailing edge and on the suction side rim. The effectiveness magnitudes immediately downstream of the tip holes show higher magnitudes as compared to Ahn et al. [6]. They presented data with coolant injection at 90° to the blade tip surface, which is more prone to dilution with the mainstream flow, thus lowering effectiveness. In the present study, coolant is injected at 45^{o} to the blade tip surface. Though the contour levels show a maximum effectiveness of only 0.6, the effectiveness in the hole and near hole region is very high. Magnified views for three tip holes and three pressure side holes are shown in Fig. 2.18 for M = 1. Effectiveness inside the hole was recorded to be about 0.9. Lift off of the coolant jet can be noted for tip holes 5 and 8 indicating that the high jet momentum causes direct impingement on the pressure side inner rim wall. The sudden decrease in effectiveness immediately downstream of these holes is a result of the coolant jet losing contact with the cavity surface indicating lift off.

Film cooling effectiveness on the pressure side is very low for the holes near mid-chord region for M = 0.5. Nearly equal pressures in the passage and on the outer blade surface causes very little coolant to come out through these holes. The last two pressure side holes though show much higher effectiveness due to lower static pressures on the blade surface. More spreading of the coolant coming from the last 4 holes can be observed for M = 1 as compared to M = 2 resulting in higher effectiveness. For M = 2, the high momentum coolant jet shoots towards the tip gap with little spreading. On the other hand, coolant coming out from the first 5 pressure side holes for M = 1 & 2 show little spreading and relatively lower effectiveness owing to lift off of the jet from the surface because of very high local blowing ratios for these holes. Magnified views for pressure side holes 2, 5 and 8 shown in Fig. 2.16 visibly indicate the bending of the coolant jet due to decreasing local blowing ratio as the mainstream flow moves towards the trailing edge.

Film cooling effectiveness results for the pressure side inner rim wall and suction side inner rim wall have been shown in Fig. 2.19. The tip film cooling holes are designed so that the high momentum coolant jet will impinge on the pressure side inner rim wall. Coolant jets will remove heat from the tip rim wall by increasing the heat transfer coefficients. Additional coolant coverage will decrease the surface temperature difference by preventing the mainstream hot gas coming into contact with the blade tip. Almost uniform film coverage is obtained on the pressure side inner rim wall with effectiveness magnitudes increasing with higher blowing ratios. Higher magnitudes (~0.25) can be observed where the coolant jet impinges on the rim wall. Some remnants of the coolant can also be discerned from traces on the suction side inner rim wall, which can be attributed to some coolant from the tip holes getting trapped inside the recirculation vortex in the squealer cavity.

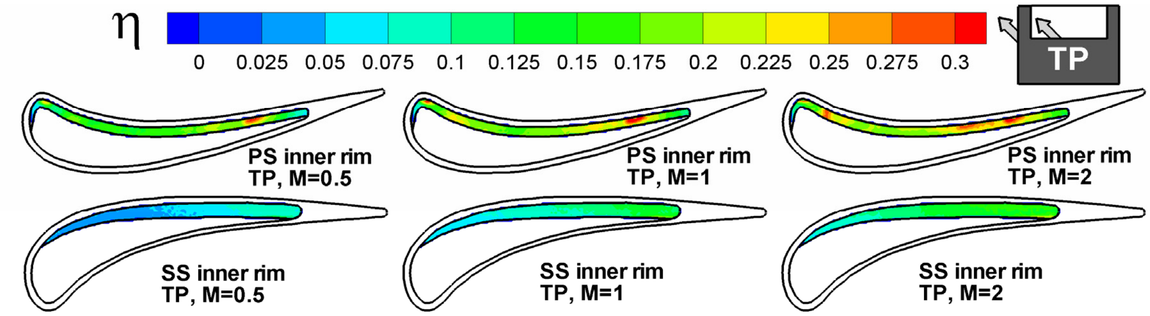

Fig. 2.19 Film cooling effectiveness distribution on inner rim walls for PS and SS for TP cases for blade 1

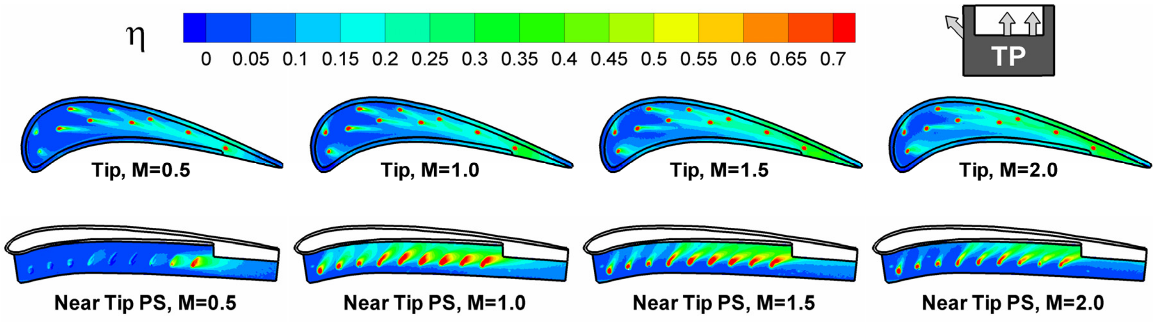

Fig. 2.20 Film cooling effectiveness distribution on tip and near tip pressure side for TP cases for a depth of 4.2% for blade 2

2.6.2. Blade 2 – Combined Tip and Pressure side injection (TP cases)

The depth of the squealer cavity is viewed as one of the key parameters affecting the film cooling effectiveness distribution. The flow field inside the squealer cavity depends on the cavity depth and consequently, the film coverage is affected. The following section discusses the film-cooling effectiveness results for TP cases for the two cavity depths for blade 2. Figure 2.20 shows the film cooling effectiveness contours for the tip and pressure side injection (TP case) and a cavity depth of 4.2% - the upper row shows the tip side and the bottom row shows the near tip pressure side. On the cavity floor region, the film coverage is seen to be improving with the blowing ratio. Coolant gets accumulated inside the squealer cavity as the ejecting coolant mass flow increases with blowing ratio. This effect is more pronounced in the region between the mid-chord and the trailing edge due to the contracting squealer passage. The accumulated coolant can be observed to cover the trailing edge cutback region resulting in high effectiveness. Effectiveness levels as high as 0.4 can be observed in the cutback region for M = 2. These levels are much higher than the effectiveness levels observed in blade 1 for a full squealer without any rim cutback. The peak level as observed by them for M = 2.0 near the trailing edge for the TP case was around 0.25. For the full squealer case, the coolant coverage near the trailing edge squealer rim is primarily due to coolant carry over from the pressure side. In the current design, both the pressure and tip injection contribute towards the film cooling effectiveness. Thus, the current cutback design is successful in providing better coverage on the trailing edge portion of the tip.

The coolant film streaks follow the mainstream flow direction inside the cavity. Even though the injection angle may be different, the mainstream flow momentum is strong enough to deflect the jets in its flow direction. The coolant trace near the upstream holes (hole 1 offset to the suction side and hole 1 along the camber line) show larger spreading and are deflected towards the rims walls. The coolant ejecting from the first hole offset to the suction side is deflected along or towards the suction side rim whereas the coolant from the other holes travels towards the pressure side rim. This directional nature can be observed at all the blowing ratios. Reattachment of the mainstream flow may occur between these two holes. The pressure side rim of the squealer acts as a backward facing step in the mainstream flow path. The flow after reattachment recirculates inwards towards the pressure side rim which may explain the coolant flow directions. The first hole offset to the suction side is outside this recirculation zone and remains unaffected. Detailed flow visualizations in the squealer cavity for a blade tip including the effect of the recirculation vortex have been done by Ameri et al. [30-32] using numerical analysis.

The rim tip region of a blade is highly susceptible to failure from oxidation due to high metal temperatures. Hence, a uniform coolant distribution is desired to reduce metal temperatures. The distributions in Fig. 2.20 reveal relatively high effectiveness levels close to the trailing edge on both the pressure and suction side rims. Coolant carry over from the pressure side holes may explain the high effectiveness on the pressure side rim. On the suction side rim, effectiveness levels as high as 0.35 are observed for M = 2.0 after the mid-chord region. The leakage flow escapes to the suction side primarily through this region. The accumulated coolant in the leakage flow helps in providing good coverage on the suction side rim. The effectiveness levels on the suction side rim though are fairly insensitive at high blowing ratios.

On the near tip pressure side (bottom row, Fig 2.20), a blowing ratio of 1.0 gives better effectiveness distribution than 1.5 and 2.0 due to more coolant spread, although the effectiveness

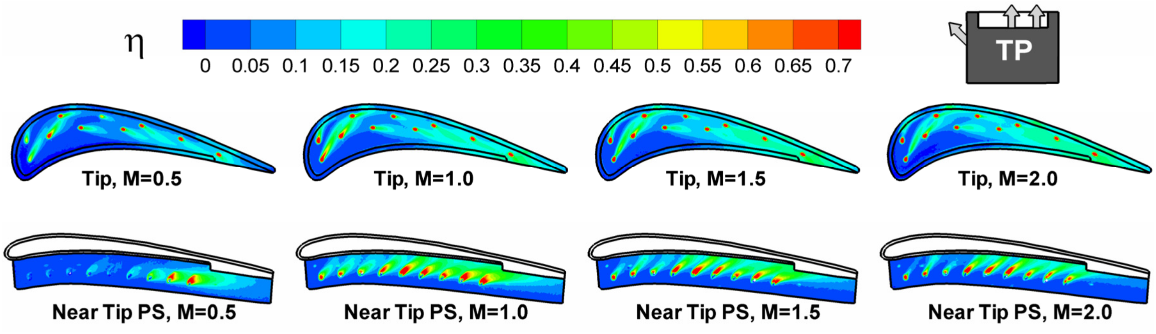

Fig. 2.21 Film cooling effectiveness distribution on tip and near tip pressure side for TP cases for a depth of 2.1% for blade 2

levels are comparable for all three. High effectiveness magnitudes can be observed on the near tip pressure side downstream of mid-chord. The compound angled shaped holes provide excellent film coverage. The first three holes on the pressure side inserted at a radial angle of 45° provide a better coolant spread for M = 1.0 than the compound angles used in blade 1 near the leading edge. For all the blowing ratios considered, the effectiveness is lower near the upstream holes due to the higher static pressure near the leading edge of the blade. This is quite apparent at M = 0.5, where the cooling effectiveness is almost negligible near the upstream holes. More coolant is diverted to the tip holes as observed from the local blowing ratio distributions in Figs. 2.13 and 2.14 for M = 0.5 due to higher surface pressures on the pressure side. Some mainstream ingestion may also occur for the first three pressure side holes for M = 0.5. At M = 2, the coolant momentum is very high causing lift off of the jet from the surface. Local blowing ratios are as high as 4.5 (Fig. 2.14) for the first hole closest to the leading edge. Lift off is indicated by a region of low effectiveness immediately downstream of the hole.

Figure 2.21 shows the effectiveness distributions for the tip and near tip pressure side with a cavity depth of 2.1% of blade span for the TP case. In the cavity floor region, the trend is similar to the one observed for the larger cavity depth, i.e., increasing effectiveness with increasing blowing ratio due to coolant accumulation. A smaller cavity depth results in a shorter reattachment length for the leakage flow entering the tip gap (Fig. 2.10). The low pressure ratio region is large enough to encompass the first two holes along the camber line and offset to the suction side. Thus, the coolant streaks injecting from these holes follow the mainstream flow path and are not diverted to the pressure side rim by the recirculation vortex as observed for the other holes. Strong traces can be observed from these upstream holes. Film effectiveness on the

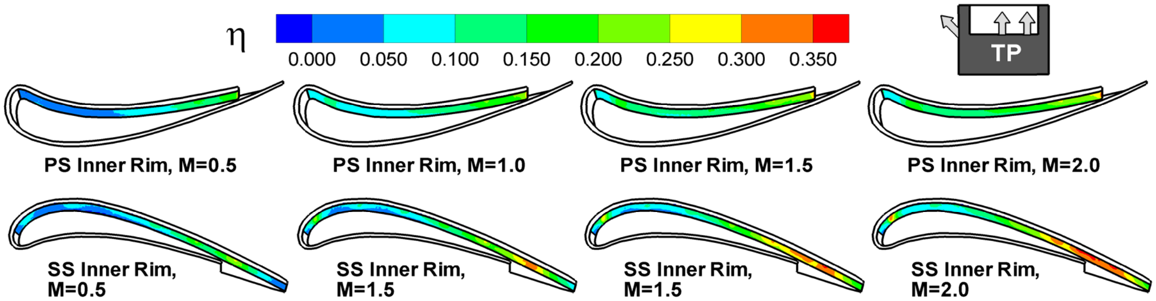

Fig. 2.22 Film cooling effectiveness distribution on inner rim walls for PS and SS for TP cases for a depth of 4.2% for blade 2

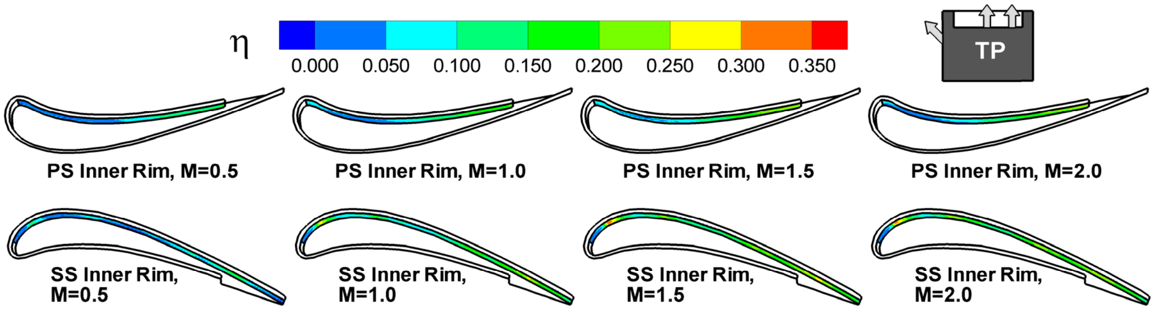

Fig. 2.23 Film cooling effectiveness distribution on inner rim walls for PS and SS for TP cases for a depth of 2.1% for blade 2

upstream cavity floor is higher for the smaller cavity depth whereas in the downstream region the effectiveness is higher for the larger cavity depth. Large shear gradients may exist due to the smaller cavity depth resulting in a fast moving recirculating vortex. This has a damaging impact on the coolant coverage resulting in lower effectiveness levels downstream of the blade mid-chord as compared to a 4.2% cavity depth (Fig. 2.20). The strong trace from the upstream holes is also felt by the suction side rim tip (a local maximum at about $x/C_x = 0.2$) resulting in higher effectiveness as compared to the 4.2% cavity depth. However, the peak magnitudes are lower at about 0.25 units. The pressure side tip rim exhibits similar behavior as that for the 4.2% cavity depth. Downstream of the mid-chord, both the pressure and suction side rims show more or less similar magnitude. The near tip pressure side distribution for the smaller cavity depth is similar to the larger cavity depth with the 2.1% cavity depth giving slightly lower effectiveness levels. Lower pressures on the tip result in larger non-uniformity in the local blowing ratios between the tip and pressure side as observed in Figs. 2.13 and 2.14. Thus, the blowing ratio for the near tip pressure side holes are lower than those for the larger cavity depth resulting in slightly lower effectiveness levels.

Figures 2.22 and 2.23 show film cooling effectiveness distribution on the inner rim walls for TP case with 4.2% and 2.1% cavity depth respectively. The effectiveness distribution on both pressure and suction side inner rim walls follow similar trends as seen for the cavity floor and rim, with the highest effectiveness in each case being near the trailing edge. The effectiveness distribution shows as increasing trend with higher blowing ratios and also increases as the recirculating flow inside the squealer cavity moves towards the trailing edge. Local high effectiveness levels can be observed on the suction side inner rim near the offset hole locations as the ejecting jets impinge laterally on these walls. Film effectiveness on the inner rim walls is lower for the smaller cavity depth. A smaller mass of coolant may get entrained in the recirculation vortex inside the squealer cavity which may explain these lower magnitudes.

2.6.3. Blade 1 – Only Pressure Side Coolant Injection (P)

Figure 2.24 depicts the contour plots for effectiveness obtained on the tip and on the near tip pressure side while Fig. 2.25 shows the effectiveness plots for the inner rim walls for three blowing ratios with coolant injection through only pressure side shaped holes. The tip holes were sealed for these cases. From Fig. 2.24, some traces of coolant can be observed on the cavity floor of squealer tip for blowing ratios of 1 and 2 near the trailing edge side. This could be due to entrainment of the coolant coming from the pressure side into the re-circulating vortex region. The effectiveness magnitudes though are very low (~ 0.1). Some coolant traces can also be discerned on the pressure side rim, which is caused by the coolant carrying over into the tip gap. . Higher effectiveness magnitudes can be noted near the trailing edge rim. Effectiveness magnitudes though are generally much lower than those for TP cases.

As observed for TP cases, more spreading of the coolant can be observed for M = 1 on the near tip pressure side as compared to M = 0.5 and M = 2 for holes near the trailing edge. Weaker jet momentum from these holes for M = 0.5 restricts the spreading of the coolant. The effectiveness on the pressure side though is much higher for M = 0.5 as compared to TP case mainly because in the latter case more coolant was diverted to the tip holes. This effect can also be discerned from the local blowing ratio plot in Fig. 2.12. M = 0.5 shows more spreading near the first few holes close to the leading edge than M = 1.0 and 2.0. High momentum jets for M = 2.0 on the other hand, do not smear as much as for M = 0.5 and 1.0 resulting in a relatively

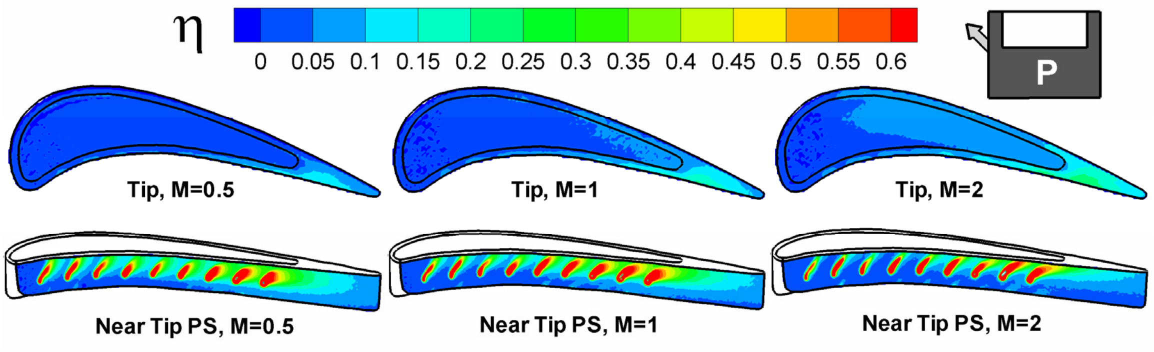

Fig. 2.24 Film cooling effectiveness distribution on tip and near tip pressure side for P cases for blade 1

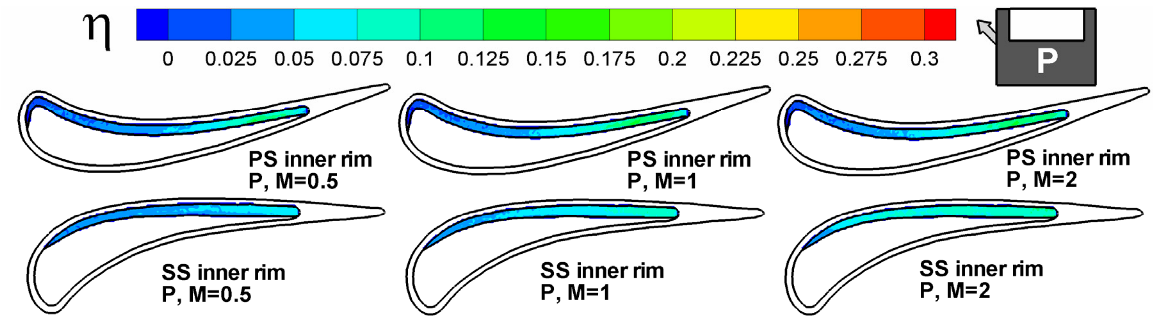

Fig. 2.25 Film cooling effectiveness distribution on inner rim walls for P cases for blade 1

straighter coolant trace. Lift off of the coolant jet can also be observed for the holes closer to the leading edge and mid chord. This effect is similar to that observed for TP cases and may be attributed to the very high local blowing ratios for these holes. Some minor traces of the coolant can also be observed for the inner rim walls from Fig. 2.24 on the pressure and suction side of the squealer cavity with higher magnitudes for higher blowing ratios.

2.6.4. Blade 2 – Only Pressure Side Coolant Injection (P)

Figures 2.26 and 2.27 show the film cooling effectiveness distributions for the P case with a cavity depth of 4.2% and 2.1% of span respectively. Most of the squealer cavity floor remains unprotected as almost no coolant from the pressure side holes gets entrained in the recirculation vortex similar to that observed for blade 1. Slight traces can be observed on the pressure side rim due to some coolant carry over. The effectiveness magnitudes for the PS rim are comparable

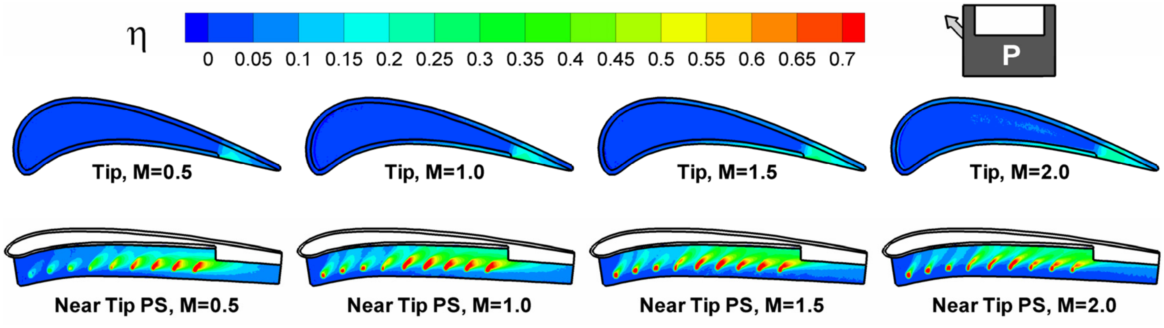

Fig. 2.26 Film cooling effectiveness distribution on tip and near tip pressure side for P cases for a depth of 4.2% for blade 2

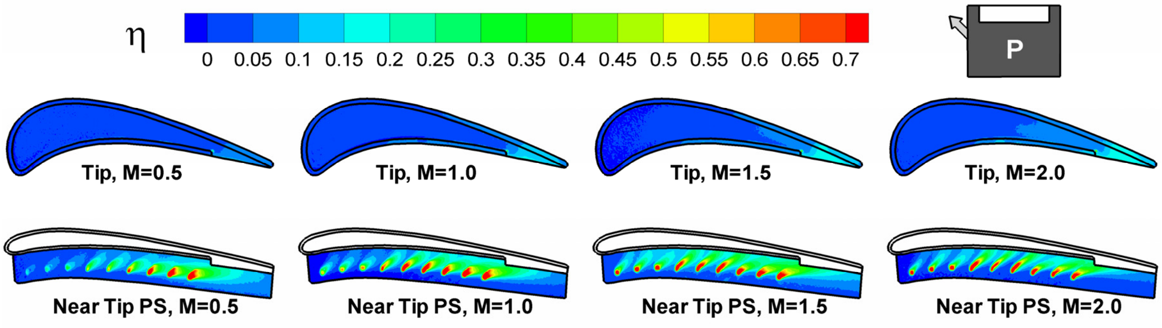

Fig. 2.27 Film cooling effectiveness distribution on tip and near tip pressure side for P cases for a depth of 2.1% for blade 2

to the TP case. Provision of the cut-back, helps the coolant from the compound shaped holes to cool the rims and the cut-back surface. Minor traces can also be observed on the suction side rim. In general, cases with a 4.2% cavity depth give higher effectiveness magnitudes in the cutback region with magnitudes increasing with blowing ratio. Optimal film cooling effectiveness on the near tip pressure side is observed for M = 1.5 as opposed to M = 1 for TP cases. Effectiveness data for M = 1.0 for TP case is comparable to data for M = 1.5 for P case. The local blowing ratios for these cases for the near tip pressure side holes are similar which may explain this result. Comparison between the TP and P cases shows that on the pressure side, the effectiveness levels for M = 0.5 and 2 are higher for the P case. For M = 0.5, local blowing ratios (Fig. 2.14) for the TP case are very low as compared to the P case which explains the higher effectiveness for the P case. On the other hand, for M = 2.0, local blowing ratios for the TP case are very high, causing lift off and resulting in lower effectiveness. For the 2.1% cavity depth, the effectiveness levels are marginally lower than for 4.2% cavity depth, both on the

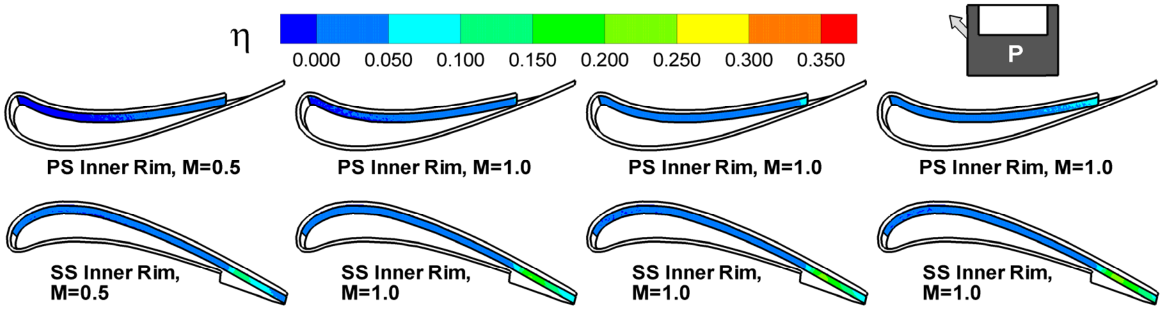

Fig. 2.28 Film cooling effectiveness distribution on inner rim walls for P cases for a depth of 4.2% for blade 2

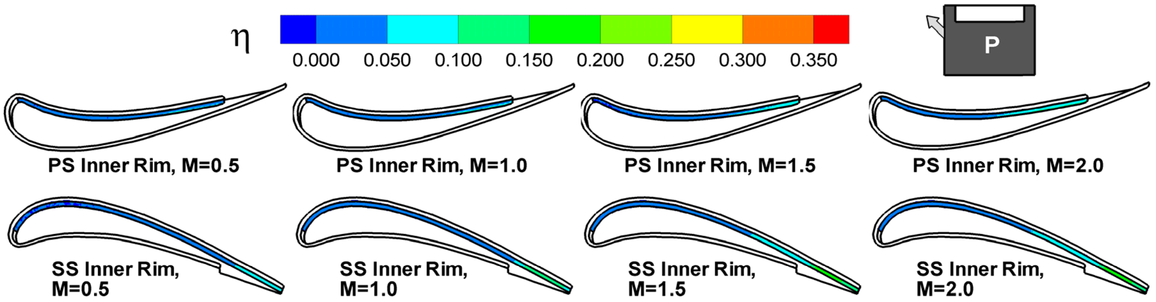

Fig. 2.29 Film cooling effectiveness distribution on inner rim walls of PS and SS for P cases for a depth of 2.1% for blade 2

pressure side and the rim. Effectiveness on the inner rim walls (Figs. 2.28 and 2.29) is seen only near the cut-back, mainly on the suction side. The effectiveness level is similar to the one on the cut-back cavity floor, which is about 0.1. As observed earlier, the lower cavity depth gives marginally lower effectiveness values.

2.6.5. Blade 1 – Averaged Film-Cooling Effectiveness Results

Figure 2.30 shows the variation of averaged film-cooling effectiveness along the axial chord for the plane and squealer blade tip for all cases. The averaged values are obtained by averaging the effectiveness magnitudes at a given x/C_x location. For the near tip pressure side holes, the averaged results were obtained by averaging from the base of the hole to the tip. Data is shown for all 6 surfaces for each case. The trends indicate that effectiveness increases with blowing ratio. High peak values for effectiveness can be noted for the near tip pressure side surface with each spike representing the presence of a hole. This is mainly due to higher effectiveness on this

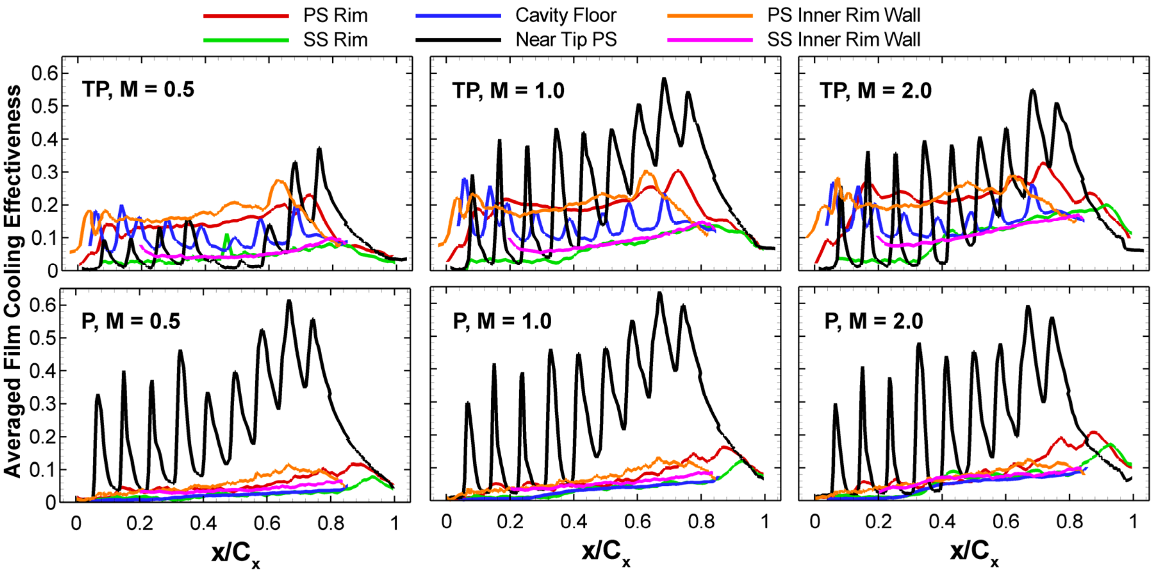

Fig. 2.30 Averaged film cooling effectiveness from experimental results for all cases for blade 1

surface due to the presence of shaped holes. The peak values near the hole locations on the cavity floor though are much lower as the area closer to the suction side inner rim wall shows low effectiveness magnitudes. Hence, after averaging, the peak values are muted. Almost uniform effectiveness of about 0.2 can be observed for the pressure side rim and inner wall for TP cases. For P cases, effectiveness values are very low (<0.1) for the cavity floor and inner rim walls. Average values for the near tip holes are similar to those for TP case. Figure 2.31 shows the area-averaged film cooling effectiveness results. It can be noted that for the near tip pressure side, a blowing ratio of M = 1 shows best performance for TP and P cases due to spreading of the coolant. For the other surfaces on the tip though, M = 2 shows highest effectiveness.

2.6.6. Blade 2 – Averaged Film-Cooling Effectiveness Results

Figures 2.32 and 2.33 depict the variation of averaged film-cooling effectiveness along the axial chord for the TP and P case respectively. Data is shown for all six surfaces for each case. In general, for TP cases, average effectiveness increases with increasing axial chord distance for all surfaces. Very close to the trailing edge (x/C_x > 0.9), the effectiveness magnitudes start dropping. Beyond x/C_x = 0.8 for the TP case, the coolant coverage in the cavity floor and the suction side rim region is better than the near tip pressure side region. This is particularly true at higher blowing ratios for both depths. This is due to the leakage flow diverting the coolant from

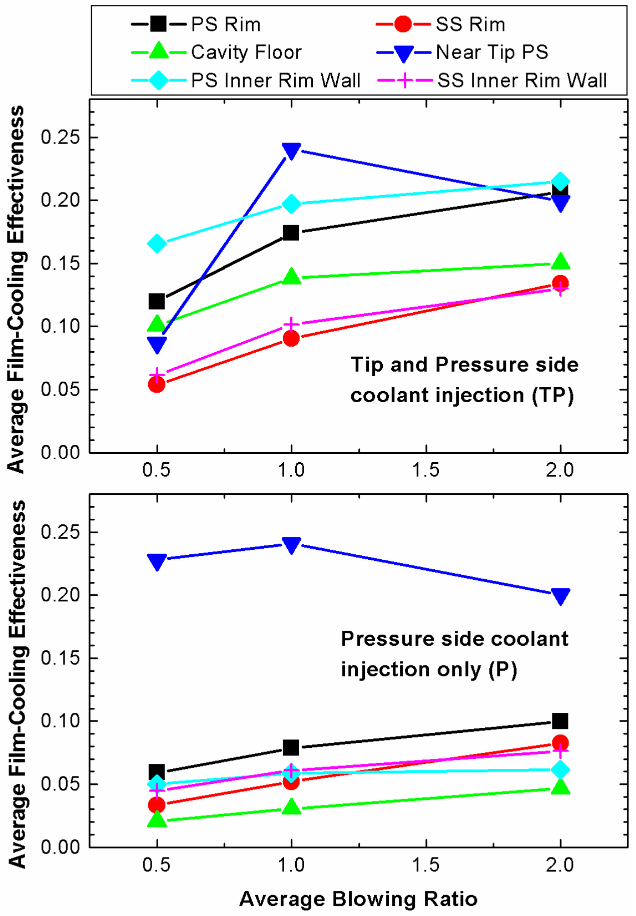

Fig. 2.31 Area averaged film cooling effectiveness for blade 1

the compound shaped holes on to the cut-back surface. For all surfaces other than the near tip PS, effectiveness increases with blowing ratio for both TP and P cases similar to that observed from Fig. 2.34 which shows the area averaged results. For the near tip pressure side, highest results are obtained for M = 1.0 for TP case and M = 1.5 for P case. For the P cases, the near tip PS effectiveness values are much higher than the rest of the blade tip regions, particularly at low blowing ratios. Similar to the TP case, a larger cavity depth gives higher effectiveness.

2.7. CONCLUSIONS

A parametric study has been performed for measuring film-cooling effectiveness on two squealer blade tip with different film cooling hole arrangements. Effectiveness was measured on the cavity floor, rim, cavity rim walls and near tip pressure side. Effects of squealer cavity

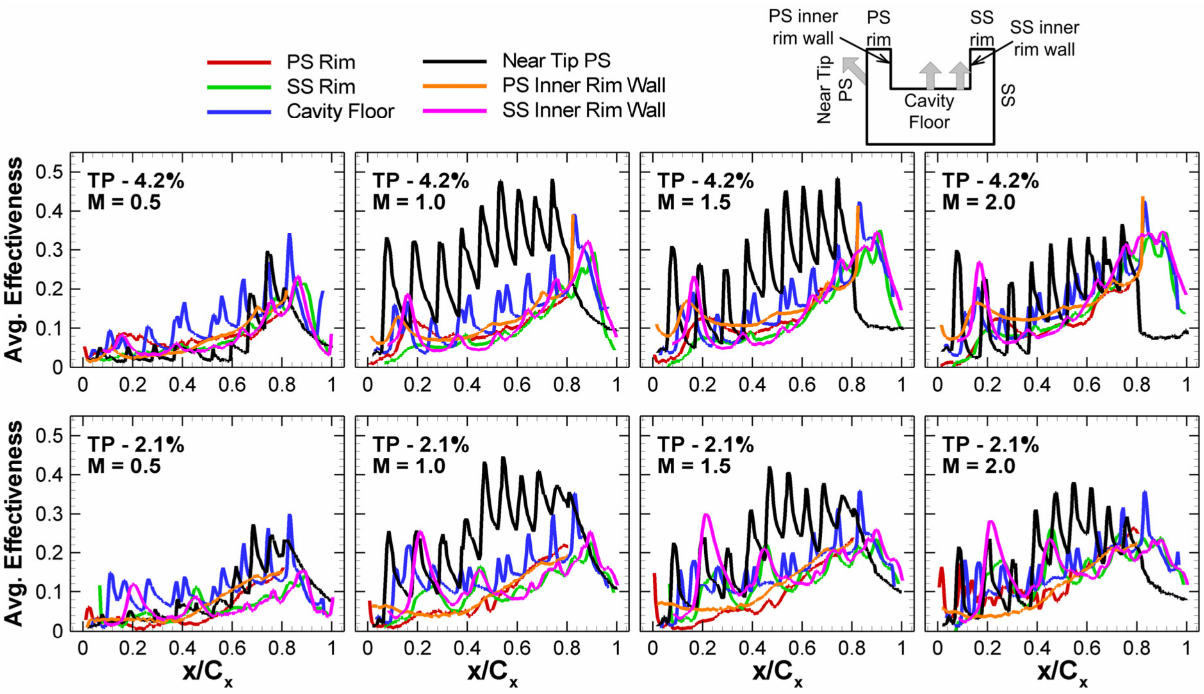

Fig. 2.32 Averaged film cooling effectiveness from experimental results for TP cases for blade 2

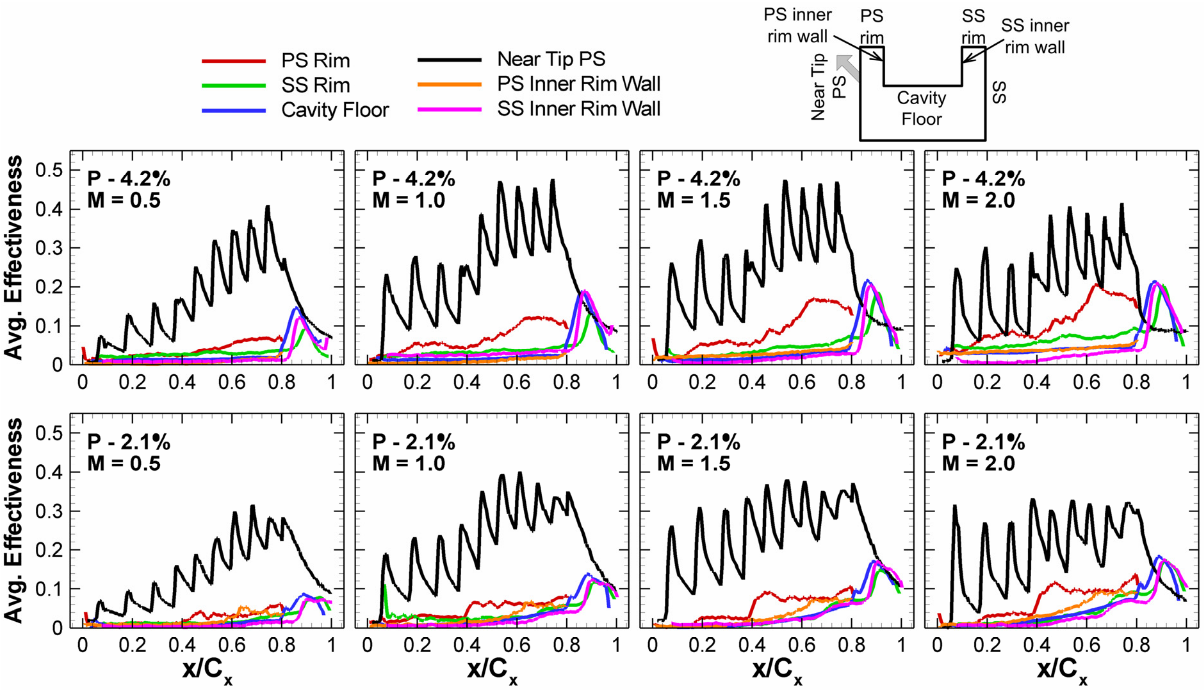

Fig. 2.33 Averaged film cooling effectiveness from experimental results for P cases for blade 2

depth, coolant injection from pressure side and tip & pressure side and varying blowing ratio

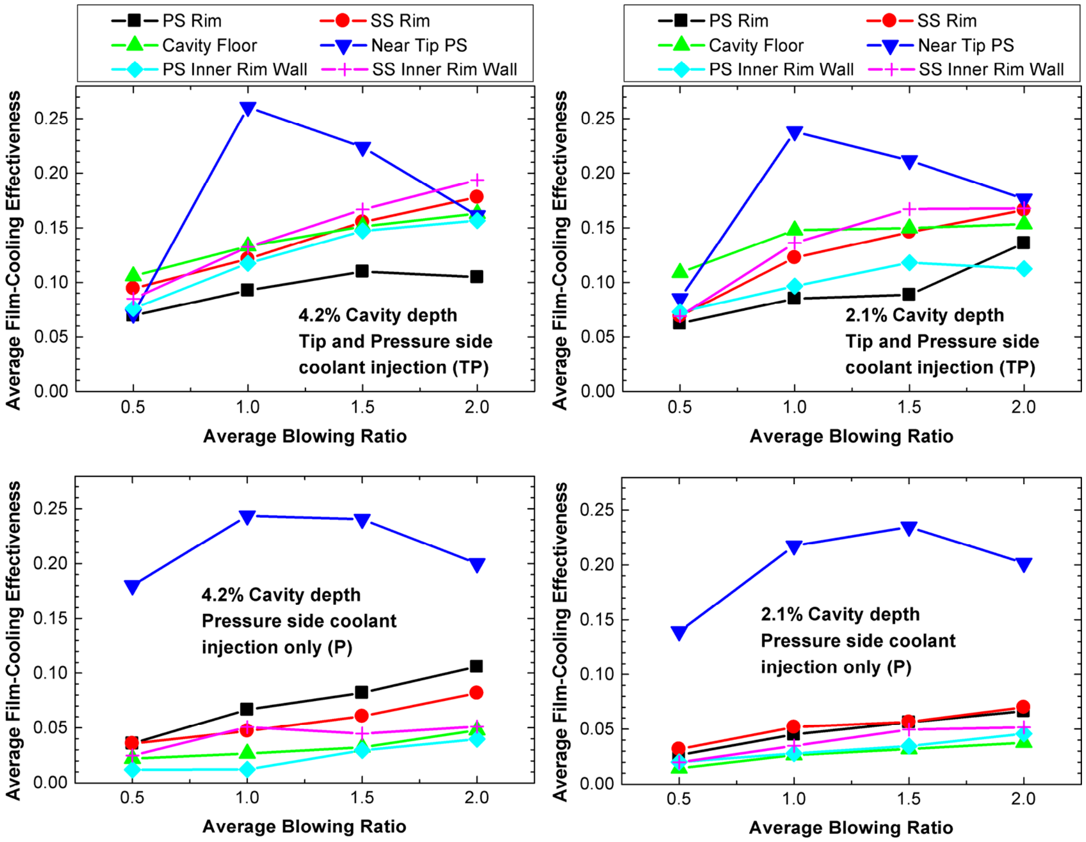

Fig. 2.34 Area averaged film cooling effectiveness for blade 2

have been studied. Major findings from the experimental results are listed below.

1. In general, higher blowing ratios give higher effectiveness on the tip rim, cavity floor and inner rim walls for both blade designs. For the near tip pressure side, M = 1 and 1.5 shows best results.
2. The pressure side rim and inner and outer squealer rim walls show high and uniform effectiveness due to the combined effect of tip and pressure side coolant injection for both blade designs.
3. Entrainment of coolant in the squealer cavity recirculation vortex can help in providing film coverage on the suction side rim and inner rim wall.
4. The film cooling hole arrangement on the tip used in blade 2 provides much better film coverage on the tip walls than the arrangement used in blade 1.
5. The cutback squealer rim used in blade 2 results in high effectiveness in the trailing edge region of the blade tip as compared to a full squealer.

6. In general, a larger cavity depth gives higher effectiveness on all tip surfaces for TP and P cases.
7. Coolant accumulation results in increasing effectiveness from blade leading edge to trailing edge for blade 2.
8. Coolant injection from only pressure side gives poor film cooling performance on the cavity floor and inner rim walls for both blade designs.
9. Presence of serpentine passages to supply coolant to the holes results in a large variation of local blowing ratios, which can have a significant impact on film cooling performance.

3. TURBINE BLADE SPAN FILM COOLING

3.1. INTRODUCTION

Thermodynamic analysis of gas turbines shows that the thermal efficiency and power output can be increased with higher turbine inlet temperatures. Continuous operation at high temperatures (~1500^{o}C) though can increase the susceptibility to failure of the hot gas path components due to build up of thermal stresses. Thus, turbine components are designed such that high metal temperatures are avoided. Internal cooling of turbine components by supplying coolant through their hollow interior and also by coating their exterior with a ceramic layer preventing direct contact with the hot gases can help in lowering metal temperatures. This lowers the heat flux entering the turbine and its components. In addition to these two methods, film cooling is often employed as an active cooling method to further reduce contact between the metal and hot gas. The surface is perforated with holes through which high pressure coolant is injected over the hot blade surface. This injected coolant displaces the mainstream boundary layer to form a film of colder air over the surface thus reducing the temperature gradient in the metal blade. This active method of cooling is termed as film cooling and is expressed in terms of the film cooling effectiveness. Thus, a high and uniform effectiveness will increase the Low Cycle Fatigue (LCF) life of the turbine component by reducing thermal stresses.

The blade span experiences some of the highest heat transfer coefficients on the external blade surface due to presence of complicated vortex structures originating from the interaction between the inlet boundary layer flow and the blade geometry. In addition, mainstream flow stagnation at the leading edge of the blade causes a very thin boundary layer in this region. The resulting heat transfer coefficients are the highest experienced on the entire blade region. The large metal area exposed to the hot mainstream also increases the heat load on the component. To reduce this high heat load, advanced internal cooling techniques are frequently used in the blade interior cavities to cool the surface. Film cooling is also used extensively. Several arrays of closely spaced film cooling holes collectively termed as showerhead film holes are used to prevent contact between the hot mainstream and metal blade on the leading edge. The pressure and suction surfaces of the blade are also dotted with several film cooling hole rows to provide

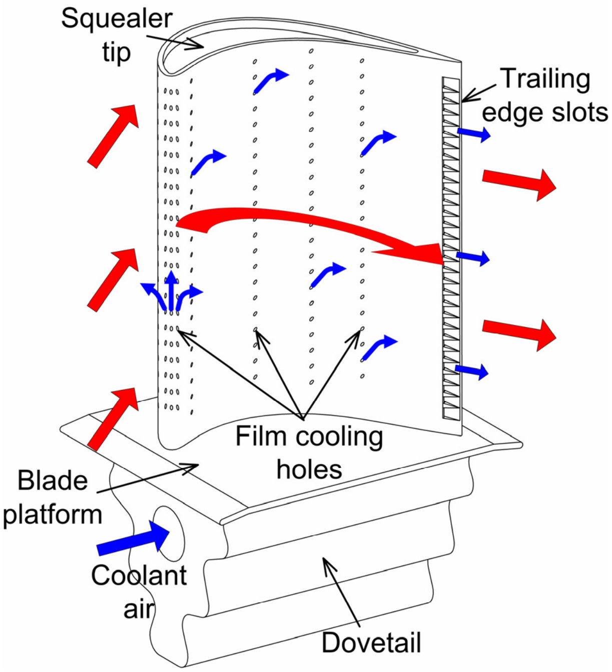

Fig. 3.1 Typical film cooling blade design

complete film coverage of the blade. Figure 3.1 shows a typical model of a fully-cooled turbine blade. High coolant velocities inside the film holes coupled with high heat transfer coefficients from developing flow in the hole entrance region also help in heat extraction from the blade span. The present paper investigates the full coverage film cooling effectiveness on a rotor blade with a typical film cooling hole array design used in commercial gas turbines. A comprehensive compilation of the available cooling techniques used on external and internal surfaces of blades and vanes used in the gas turbine industry have been encapsulated by Han et al. [1].

Experimental investigations on film cooling in rotating turbine blades and their components though are few and far between, primarily due to the difficulty in instrumenting rotating parts. Dring et al. [42] investigated film cooling performance in a low speed rotating facility. A film cooling hole was located on both the pressure and suction sides. They used ammonia and Ozalid paper to qualitatively observe the coolant trace while the quantitative tests were conducted using thermocouples. Their results show that on the suction side, the film coolant had only a small radial displacement, similar to flat plate results. On the pressure side, the film coolant trace had a large radial displacement toward the blade tip. Effectiveness distributions on the blade span for a rotating turbine blade were also provided by Takeishi et al. [43] using gas chromatography and were compared to results in a stationary cascade under similar flow conditions. Their results showed that the effectiveness on the suction surface for both the cascade and the rotating rig matched well whereas on the pressure surface, the film effectiveness under rotating conditions decreased more rapidly than under stationary conditions. They explained that this phenomenon is due to radial flow and enhanced mixing on the pressure side. Overall effectiveness magnitudes on the suction side were found to be higher than those on the pressure side. Abhari and Epstein [44] did time-resolved heat transfer measurements using thin film heat flux gages in a fully cooled transonic turbine stage with 3 rows of film cooling holes on the pressure surface and 2 rows on the suction surface. Their results indicated that film cooling on the suction surface gave a larger reduction in Nusselt numbers as compared to the pressure surface.

Several studies have also been performed for film cooling and heat transfer on the span in cascade vane as well as blade simulations. Nirmalan and Hylton [45] studied the effects of Mach number, Reynolds number, turbulence intensity, coolant-to-gas temperature ratio and coolant-to-gas pressure ratio on film cooling in a turbine vane cascade with flow parameters similar to those found in actual engines. Showerhead coolant injection with 6 rows of film holes was used with 2 additional rows on the pressure side and one more row on the suction side. Abuaf et al. [46] presented heat transfer coefficients and film effectiveness for a film cooled vane. Film injection was found to have a minimal impact on heat transfer coefficients on the pressure surface while on the suction surface, the heat transfer coefficients show a significant increase. Camci and Arts [47, 48] tested blades with a leading edge film cooling array and suction side film cooling in a short duration wind tunnel facility. They found that a lower coolant-to-freestream temperature resulted in better cooling efficiency.

Film cooling on the blade span near the endwall was studied by Goldstein and Chen [49] using gas chromatography. The passage vortex was found to significantly reduce the film effectiveness on the suction side close to the endwall with the reduction becoming progressively larger towards the trailing edge. No such effect was observed on the pressure side. Film cooling and heat transfer from three rows of showerhead holes and 2 rows of holes each, on the pressure and suction sides was studied by Mehendale et al. [50]. They studied the effect of freestream turbulence in a 5 blade cascade. Effect of rotating unsteady wake on the same cascade was investigated by Ou et al. [51] and Mehendale et al. [52]. High freestream turbulence and unsteady wake decrease film coverage but promote higher heat transfer coefficients in addition to the enhancement resulting from film injection. Ekkad et al. [53] studied the combined effect of unsteady wake and freestream turbulence on film cooling effectiveness and heat transfer coefficient with air and CO_2 film injection. Combining both gave higher heat transfer coefficients and lower film cooling effectiveness as compared to their individual effects. Local heat transfer and film cooling distributions for the same cascade were also investigated by Du et al. [54]. Ames [55, 56] studied film cooling on a turbine vane under high freestream turbulence conditions. Significant reduction in film effectiveness was observed far downstream of the holes at high turbulence levels. Drost and Bolcs [57] presented the detailed film cooling effectiveness distributions and the heat transfer enhancement due to film injection from a single row and double row coolant injection on the suction side and a single row coolant injection on the pressure side. Their results gave a significant net heat flux reduction near the holes at low blowing ratios which disappeared further downstream. On the pressure side, best effectiveness near the hole was obtained for a blowing ratio of 1.3.

A numerical simulation of a rotating, film cooled blade was performed by Garg et al. [58] and compared with results from an uncooled blade. The heat transfer coefficient on the cooled blade surface was found to be generally lower than that on the uncooled blade, except in the shower-head region and in the tip region on the suction side. Another numerical study was performed by Heidmann et al. [59] for a film cooled turbine vane with several film cooling hole geometries. Effect of a rotating, unsteady wake on film cooling effectiveness and coolant jet temperature profiles on the suction side of a turbine blade were investigated by Teng et al. [60] in a low speed cascade. The unsteady wake reduced the effectiveness magnitudes. Local heat transfer immediately downstream of the holes was found to increase by as much as 60% due to film injection. Teng and Han [61] compared heat transfer from diffuser shaped (laidback and fan-shaped) film hole rows against cylindrical holes on the suction side of a turbine blade under the presence of upstream wake. Expanded hole injections gave lower heat transfer coefficients over the surface downstream of injection location, particularly at high blowing ratios. Takeishi and Aoki [62] presented film cooling distributions from several rows of holes on the span of a turbine vane and blade in a low speed cascade. They compared film cooling from cylindrical holes and shaped holes and found that shaped holes gave higher effectiveness by about 20% on the suction side. They also studied full coverage film cooling from all holes and individual film coverage on the blade pressure side. Effectiveness with full coverage film cooling i.e. with film ejection from all hole rows, was higher than that from individual row injection due to coolant accumulation from upstream holes.

Heidmann et al. [63] studied the effect of wake passing on showerhead film cooling performance in an annular cascade. A high wake Strouhal number was found to decrease effectiveness but it was also found to divert the coolant towards the pressure side resulting in slightly better cooling on the pressure side. Film cooling effectiveness from axial cylindrical holes and axial and compound angled shaped holes was studied by Furukawa and Ligrani [64] on a symmetric airfoil in a transonic wind tunnel. Compound angled shaped holes provided the best effectiveness distributions followed by axial shaped holes and axial cylindrical holes. Cutbirth and Bogard [65, 66] in two papers studied the flow field near the coolant holes and film cooling effectiveness from showerhead film cooling in a low-speed vane cascade. They studied the effect of density ratio and freestream turbulence on the local effectiveness distribution. Coolant jets were found to separate from the leading edge even at low blowing ratios. Higher density ratios and lower freestream turbulence were found to give higher effectiveness magnitudes. The above discussed technical papers, however, have not studied the effect of superposition on film cooling.

The principle of superposition was first proposed by Sellers [67] who found that film injection from single rows when added, is equivalent to film injection from multiple rows. The superposition approach was further developed by Choe et al. [68]. Muska et al. [69] performed experiments to substantiate the method proposed by Sellers [67] on a flat plate as well as on an airfoil. The airfoil was fitted with showerhead array of holes as well as two additional rows of holes on the suction side. Good agreement was found between the measured and predicted results on a flat plate and on the suction side of the airfoil. The superposition effect on the pressure side was not investigated.

Polanka et al. [70] and Cutbirth and Bogard [71,72] studied the effect of superposition from a showerhead array and two pressure side holes in the same vane cascade. Polanka et al. [70] also observed a degradation in the film cooling effectiveness from the first compound angled PS hole row compared to superposition for both high and low turbulence levels in the presence of showerhead ejection. They suggested that showerhead ejection generates additional turbulence near the leading edge region which may cause the observed degradation. Detailed flow and thermal field measurements were performed by Cutbirth and Bogard [71, 72] in two papers to assess the impact of showerhead injection on the film degradation from the first compound angled PS hole row. They measured turbulence generated from showerhead injection and found this degradation to exist even for cases with higher mainstream turbulence. Smaller turbulence length scales from showerhead injection was thought to cause this effect. Schneider et al. [73] studied the effect of superposition for multiple row injection on the pressure side with fan-shaped holes using a steady state liquid crystal technique with carbon-dioxide as coolant gas. Superposition on the pressure side was investigated with and without showerhead injection.

The present study focuses on full coverage film cooling on a high pressure turbine rotor blade using 3 rows of showerhead holes on the leading edge and six rows of film cooling holes on the pressure and suction surfaces. Individual row film cooling for the showerhead array as well as each individual row on the Pressure and Suction side blade span is also investigated. The hole geometry and location along with the internal coolant supply passage design are modeled similar to typical blade designs used in commercial gas turbines. Experiments were performed in a 5-bladed linear cascade with relatively high freestream Mach numbers with inlet and exit Mach numbers of 0.27 and 0.44 respectively. The effects of a stationary, upstream wake at the cascade inlet and blowing ratio at these high Mach numbers are also examined on film cooling effectiveness. The current study aims to understand the transient behavior of a rotating wake using stationary wake rods under a fixed frame of reference and to determine its impact on film cooling. Superposition of film effectiveness from individual rows is also examined and compared with results from full coverage film cooling for four different blowing ratios. Additionally, detailed distributions of the coolant traces are presented on the entire blade surface using the Pressure Sensitive Paint (PSP) technique. Prior studies on blade span film cooling have not captured the local effectiveness distributions under the influence of an upstream wake and different blowing ratios on the entire blade surface stretching from hub to tip.

The PSP technique used for measuring film cooling effectiveness is based on mass transfer analogy and is free from heat conduction related errors frequently encountered with other heat transfer measurement techniques measuring adiabatic effectiveness. PSP works by sensing the partial pressure of oxygen on the test surface. By displacing the oxygen on the platform via nitrogen injection from the film holes and by measuring the relative difference between air and nitrogen injection, the film cooling effectiveness can be calculated. Since no heating is involved, errors resulting from lateral heat conduction in the test surface are avoided resulting in a clean and well-defined coolant trace. The turbine heat transfer research group from Texas A&M University has been actively involved in the development of this technique for film cooling effectiveness measurement. A detailed working methodology of PSP to measure film cooling effectiveness has been described in Wright et al. [40]. The results from this technique have been

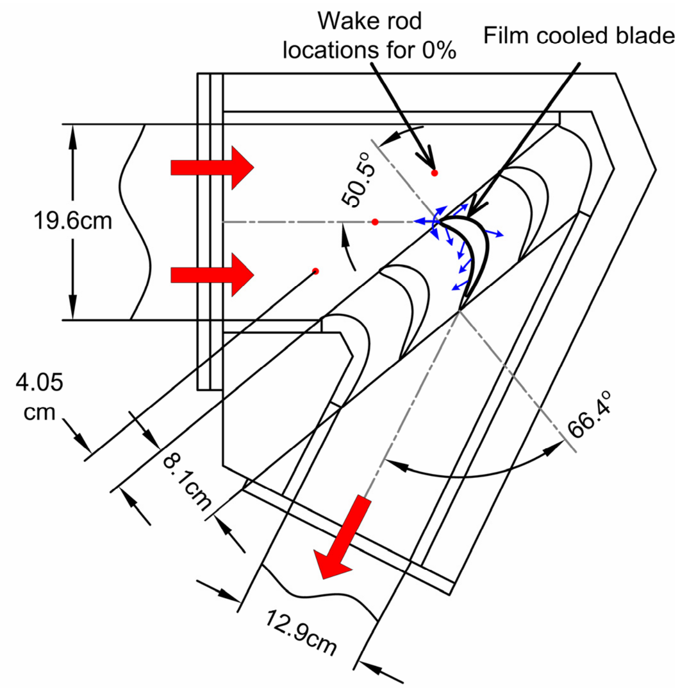

Fig. 3.2 Schematic of cascade with film cooled blade

calibrated with other measurement techniques by Wright et al. [40] on a flat plate and Gao et al. [74] on a film cooled cylindrical leading edge model in low speed wind tunnels. Gao et al. [74] compared results obtained from a steady state PSP technique and a transient IR measurement technique.

3.2. EXPERIMENTAL FACILITY

The test section consisted of a 5-blade linear cascade with center span profiles of a high pressure turbine rotor blade. A schematic of the test section and the mainstream flow loop is shown in Fig. 3.2. The mainstream air for the cascade was supplied by a three stage centrifugal compressor connected to a 450hp electric motor. The compressor is rated for a maximum pressure differential of 55kPa and a volume flow rate of 6.2m^3/s. The pressure and volume flow rate in the cascade could be varied by a frequency controller operating between 0 to 60Hz. Inlet cross-section of the test section was 19.6cm (width) x 12.7cm (height) while the exit cross-section was reduced to 12.9cm (width) x 12.7cm (height). A 0.5% blade tip clearance was provided for the center three blades. The top plate which acted as the shroud for the blades and the outer side walls of the test section were machined out of 1.27cm thick acrylic sheets for optical access to the blade pressure and suction sides. Images of the test surface were captured through this acrylic interface by a 12-bit, scientific grade CCD (Charge-coupled Device) camera mounted outside the test section. Flow conditions in adjacent passages of the center blade were ensured to be identical by adjusting the trailing edge tailboards for the cascade. The cascade inlet and exit velocities were set to be 96 m/s and 156 m/s corresponding to inlet and exit Mach numbers of 0.27 and 0.44 respectively. The inlet velocity was continuously monitored using a pitot static pressure probe placed upstream of the cascade. The Reynolds number based on the axial chord length and exit velocity was 750,000. Overall pressure ratio (P_t/P) was 1.14 (where P_t is inlet total pressure and P is exit static pressure). Turbulence intensity was recorded 6.3cm upstream of the middle blade using a hot-film probe. Turbulence intensity (Tu) at this location was found to be 6% at mid-span in the cascade. Turbulence intensity increases closer to the tip and hub walls with magnitudes measured to be as high as 11% at 0.6cm near the wall. The integral length scale was also determined using the power spectral density function and was calculated to be around 5cm near the center span at the cascade entrance. The length scale decreased to about 3cm at 0.6cm from the hub or tip.

All the five blades in the cascade had a span of 12.64cm and an axial chord length of 8.13cm. The midspan profile of a high pressure turbine rotor blade with a total flow turn angle of 116.9^o was used. Since the blades were placed in a linear cascade, they were machined for a constant cross-section for its entire span. The center test blade drilled with film cooling holes was made using Stereo lithography (SLA) as conventional machining methods were unsuitable for such a complicated geometry. The four guide blades placed in the test section were made of aluminum. Figure 3.3 shows the film-cooling measurement blade with the internal coolant supply passage geometry and the film cooling holes. The center test blade had a squealer tip with a recess of 2.4% of blade span (2.84mm) while the two adjacent blades had a flat tip. The leading edge of the blade can be approximated as an arc with a radius of 2.4mm. Three rows of showerhead film cooling holes with a diameter of 0.65mm were drilled along the leading edge of the blade. The middle row (SH-ST row in Fig. 3.3) was aligned with the stagnation line while the other two rows were placed 15^o apart on either side. 22 holes were drilled in each showerhead row resulting in a spacing of 5.3mm (s/d = 8.2). All the holes were drilled at a radial angle of 30^o to the leading edge surface. The length of hole to diameter ratio (L/d) for all the showerhead holes was 12.7. Four rows of cylindrical holes were also drilled on the pressure side

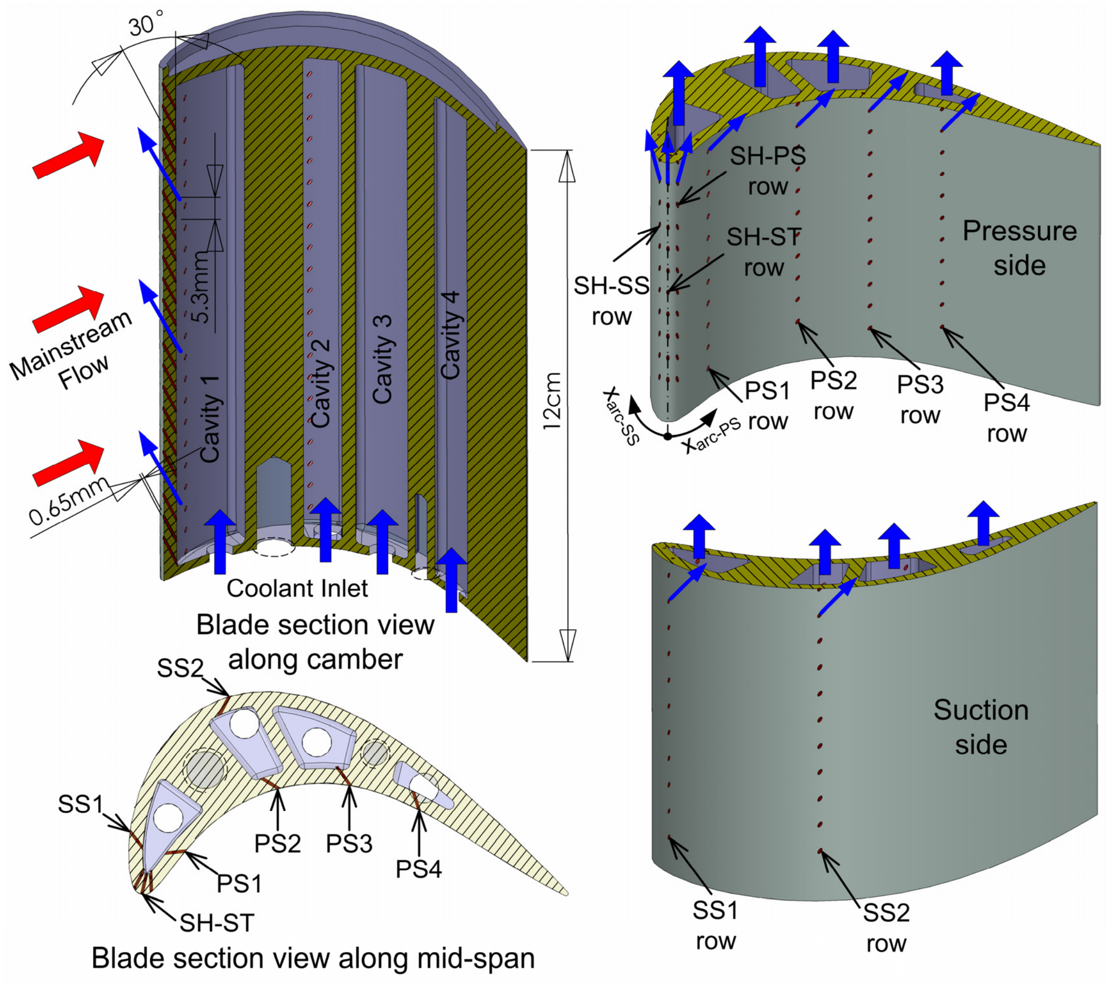

Fig. 3.3 Film cooling blade with cylindrical holes

at axial locations of 1.24cm (PS1), 3.62cm (PS2), 5.01cm (PS3) and 6.1cm (PS4). Two more rows were drilled on the suction side at axial locations of 0.38cm (SS1) and 3.56cm (SS2). Typical blade designs used in gas turbines were considered for deciding the distribution of film cooling hole rows along the blade. All the pressure and suction side holes were drilled at a compound angle of 45^o to the blade span and 45^o with respect to the airfoil surface with a diameter of 0.65mm resulting in an L/d ~ 9. The holes in adjacent rows were staggered with respect to each other. Twenty three equally spaced holes with an s/d = 8.2 were drilled along the span at the PS1, PS3 and SS1 locations. Due to the staggered arrangement, hole rows PS2, PS4 and SS2 have one hole less with 22 holes per row.

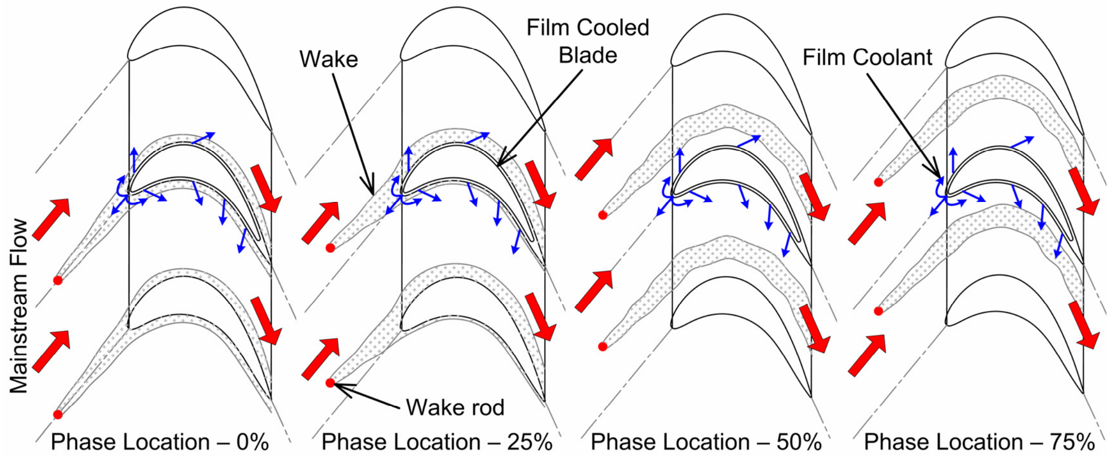

Fig. 3.4 Wake rod phase locations and conceptual view of unsteady wake effect on the test blade

Coolant was supplied to all the film hole rows through 4 cavities. The first cavity near the leading edge was designed to supply coolant to the showerhead film cooling holes as well as the first row of holes on the pressure (PS1) and suction (SS1) sides. The second cavity was designed to supply coolant to one pressure side row (PS2) and one suction side row (SS2). The remaining two cavities supplied coolant to the hole rows PS3 and PS4 respectively. The cavity cross-sections were modeled similar to the internal cooling passages in turbine blades with coolant injection through the bottom of the blade. A 3mm cavity wall thickness was provided to ensure structural integrity for the SLA blade at cascade flow conditions.

Metal rods for simulating a stationary, upstream wake were inserted periodically upstream of the blade at a distance equivalent to 50% of axial chord (4cm). Two rod diameters of 3.2mm and 4.8mm were chosen to account for the typical trailing edge thickness of an upstream vane and the boundary layer thicknesses on the upstream vane pressure and suction surfaces. The rods were placed at four equally spaced intervals corresponding to the blade pitch and their locations are shown in Fig. 3.4. The rod directly upstream of the leading edge was indicated as the 0% phase location and was 6.3cm upstream of the leading edge in the flow direction. Rod locations for 25%, 50% and 75% were progressively located along the blade pitch as indicated in Fig. 3.4. The periodically placed upstream rods simulate a progressing unsteady wake in a rotating turbine. Four sets of experiments were conducted to cover all phase locations for each rod diameter. Two rods were placed with one in the pressure side passage of the test blade and the other at the corresponding periodic location in the suction side passage for 25%, 50% and 75%

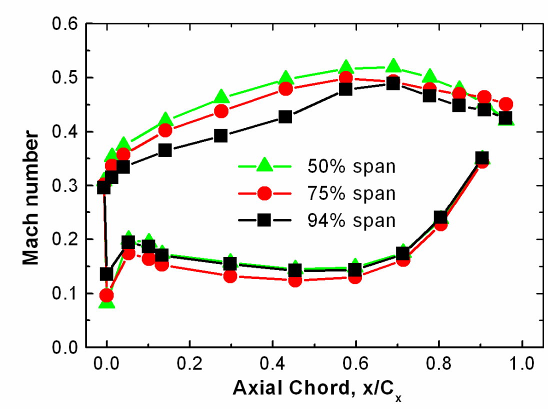

Fig. 3.5 Mach number distribution on blade span

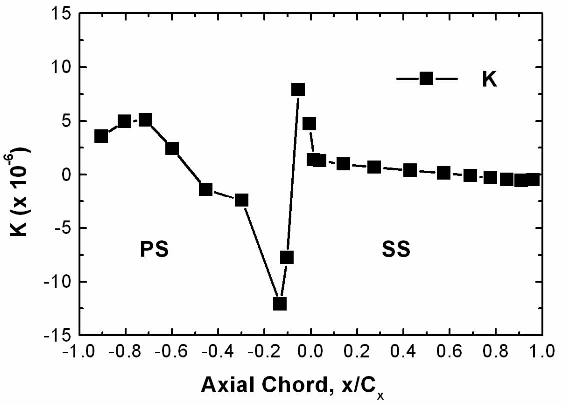

Fig. 3.6 Flow acceleration on blade

phase locations for each test while for 0%, a single rod was placed in front of the stagnation point of the center test blade.

Experiments were performed with different average blowing ratios (M) ranging from 0.3 to 1.5. The blowing ratio, M was calculated as the ratio between the coolant mass flux $\rho_c V_c$ and the mainstream mass flux $\rho_m V_m$ at the hole row location. The mainstream mass flux was obtained from total pressure measurement using a pitot static tube upstream of the test blade and static pressure measurements through surface taps along a blade specifically machined for pressure measurement. Total coolant mass flow for all holes in a cavity was pre-determined for the required blowing ratio and was set using a dedicated rotameter connected to the coolant loop for each cavity. Hence, the actual or local blowing ratio for each hole row can be different depending on the pressure variation in the coolant cavity and the outer blade surface along its span. The corresponding mass flow ratios per blade passage are 0.27%, 0.53%, 0.8% and 1.06% respectively for blowing ratios of 0.3, 0.6, 0.9 and 1.2 respectively. If the density of coolant and mainstream is same as in the present study, the blowing ratio is reduced to a velocity ratio.

As noted earlier, PS1 and SS1 share the cavity 1 while PS2 and SS2 share cavity 2. During testing for individual row film cooling, the hole row ejecting on the surface which was not being tested was sealed to prevent coolant ejection. Thus, while performing experiments on the pressure side, hole rows SS1 and SS2 were sealed and vice-versa. This enabled greater control over the blowing ratio distribution. If both hole rows were opened in a shared cavity, more coolant would have been diverted to the suction surface due to a higher pressure gradient across

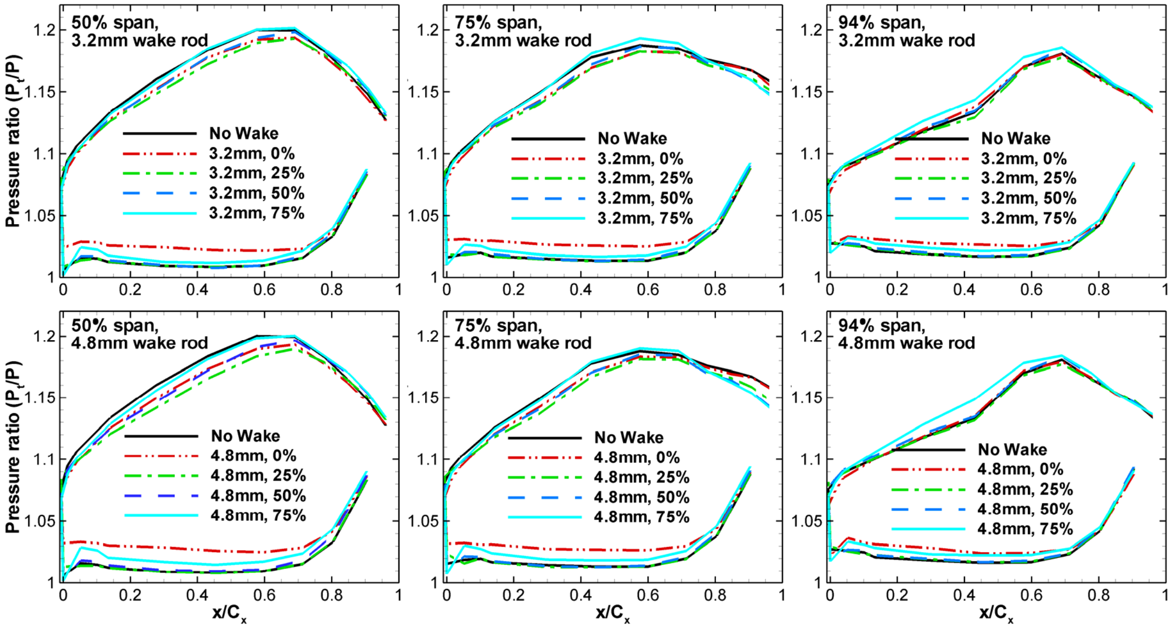

Fig. 3.7 Pressure ratio distribution on blade span under the influence of unsteady wake

the holes resulting in non-uniform blowing ratios. For the showerhead film cooling tests, all other hole rows were sealed.

3.3. FLOW DISTRIBUTION OVER THE BLADE

Figure 3.5 shows the Mach number distributions at different span locations on the blade. Pressure measurements were performed on a blade instrumented with pressure taps located at several axial locations at midspan, 75% of span (y/H = 0.75) and 94% of span (near tip, y/H = 0.94). Mach number distributions at these locations were obtained from static pressures measured from a blade instrumented with the pressure taps and the inlet total pressure measured using a pitot tube placed 6.3 cm upstream of the center blade. Pressures were recorded with a 48-channel Scanivalve System coupled with LabView software. LabView discarded all data that fell outside the initial mean ±1.5 standard deviation. It then recorded the mean value of the screened data. Every pressure measurement was repeated at least three times to reduce operating uncertainty and to verify the repeatability of the data. The pressure side Mach number distributions for all three span locations are similar. The Mach number is fairly constant on the pressure side till about $x/C_x = 0.6$ beyond which it increase sharply as the flow approaches the throat. However, on the suction side, the Mach number distribution shows an increasing trend till the throat ($x/C_x = 0.65$) and then decreases gradually. The Mach numbers at 94% span are lower as the flow is affected due to the tip leakage vortex. A clearance gap of 0.5% span gap exists between the blade tip and the shroud endwall. The static pressure difference between the PS and the SS acts as the main driving force for this leakage flow. A peak mach number of about 0.5 occurs in the throat region on the suction side with the exit Mach number close to around 0.44.

$$k = \frac{\nu}{V_x^2}\frac{dV_x}{dx} \tag{3.1}$$

Figure 3.6 shows the flow acceleration parameter, K over the blade as calculated from Eq. 3.1. Positive values indicate flow acceleration whereas negative values indicate flow deceleration. Strong deceleration can be observed on the pressure side close to the leading edge. As the flow approaches the throat, it starts accelerating with a peak magnitude of about $5\text{x}10^{-6}$ near 70% of axial chord. Relaminarization of the flow may occur for K magnitudes above $3\text{x}10^{-6}$ as indicated by Kays and Crawford [75]. On the suction side, acceleration is highest near the leading edge and decreases gradually till the trailing edge of the blade.

Figure 3.7 shows the pressure ratio distribution under the influence of a stationary wake for both wake rod diameters at all phase locations and compares it with that for the no wake case. Data is shown for three blade span locations. The pressure ratio was obtained by normalizing the blade inlet total pressure with the static pressure over the blade surface. On the pressure side, the 0% phase location has the largest impact on the distribution as compared to the no wake case. The pressure ratio is higher indicating that the local velocity on the blade surface is also higher. The additional turbulence from the wake may reduce the boundary layer thickness on the pressure side which may explain the higher velocity. Wake rods at 75% phase location have a minor impact on the distribution whereas the other phase locations do not show any noticeable effect. On the suction side though, the effect of wake is opposite. The presence of wake increases the static pressure on the surface resulting in a lower pressure ratio. This effect is largest for the wake rods at 25% phase location with the effect from 0% phase location being slightly lower. Also, a larger wake rod diameter causes a greater impact on the pressure ratio distribution.

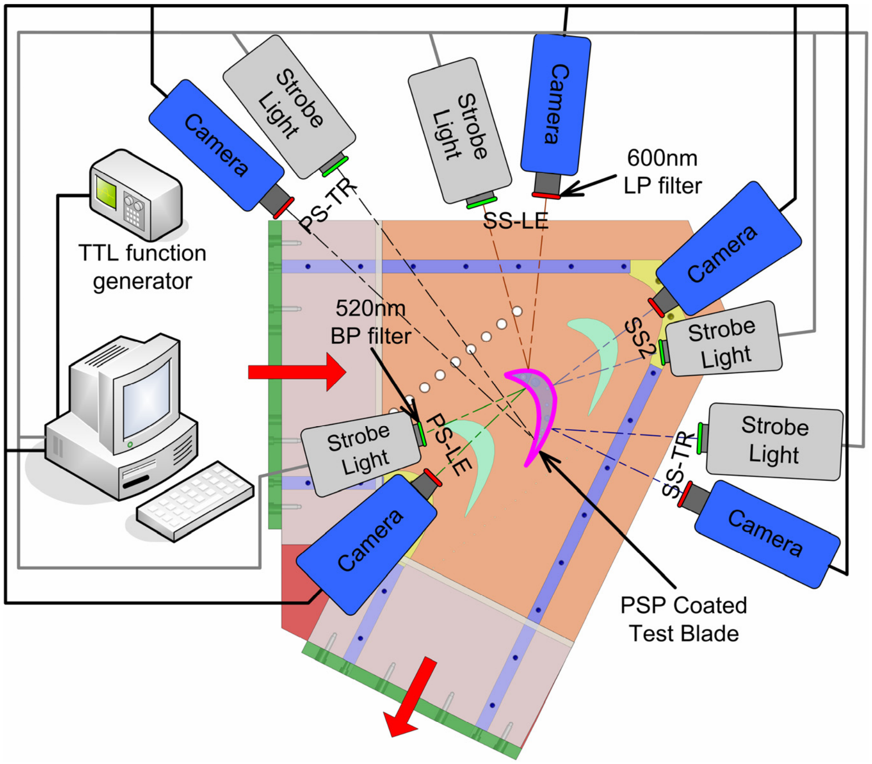

Fig. 3.8 Optical component setup for blade span film cooling

3.4. FILM-COOLING EFFECTIVENESS MEASUREMENT THEORY AND DATA ANALYSIS

Data for film cooling effectiveness was obtained by using the PSP technique. The PSP measurement technique along with the associated uncertainties in the data has been described in detail in section 2.4. For blade span film cooling, the center test blade in the cascade which was under investigation was layered with PSP using an air brush. The same optical components used for blade tip cooling were employed for this study. A schematic of the optical components setup and camera positions is depicted in Fig. 3.8 for blade span film cooling. Due to the blade curvature and surface accessibility, images of the blade were captured from five camera positions; 2 positions for capturing images on the pressure side and 3 on the suction side. The camera and the strobe light were triggered simultaneously using a TTL signal from a function generator. A total of 200 TIF images were captured for each experiment with air and nitrogen injection and the pixel intensity for all images was averaged. The image resolution obtained from the camera was 0.6 mm/pixel. A computer program was used to convert these pixel intensities into pressure using the calibration curve and then into film cooling effectiveness. The coolant flow rate into each cavity was set using a rotameter based on prior calculation for the desired mass flow ratio. The coolant was heated to the same temperature as mainstream air (~35^{o}C) before injection through the holes.

3.5. DISCUSSION OF RESULTS

3.5.1. Full Coverage Film Cooling Effectiveness on Blade Span under No Wake

Figure 3.9 shows the contour plots for the film cooling effectiveness distribution on the pressure and suction sides for mainstream flow with no wake. Contour plots are shown for all four blowing ratios. The images of the blade surface captured by the camera from five different positions were averaged and the film cooling distribution on the curved blade surface obtained after data reduction have been plotted by projecting it onto a radial plane passing through the axial chord of the blade. The abscissa and the ordinate have been normalized using the axial chord length and the blade height respectively. For the pressure side, the 5th coolant hole from the tip (SH-PS row at y/H = 0.75) in the showerhead array was blocked due to a manufacturing defect in the blade and hence no coolant is observed to exit in this region.

The coolant flow through a film hole is proportional to the driving pressure differential across it. Thus, for coolant ejection, the static pressure inside the coolant cavity needs to be higher than the static pressure on the blade outer surface. As the coolant enters the cavity from the blade hub, it reaches stagnation inside the cavity near the tip (y/H = 1) thus setting up a pressure gradient from the hub to the tip with higher pressure at the tip. This higher cavity pressure might result in higher coolant mass flow through the holes close to the tip. Also, for film cooling rows on the pressure and suction side which share the same coolant supply cavity, due to lower static pressure on the suction surface, more coolant may get diverted to the suction side resulting in a higher coolant jet velocity. However, this may or may not affect the local blowing ratio for each row as the coolant and mainstream velocities are both higher on the suction side. The resulting coolant to mainstream velocity ratio for each row may be the same. The effect of the pressure differential on the two blade sides on coolant distribution can be clearly observed for M = 0.3 and 0.6 for shared cavities 1 and 2. Due to higher static pressure on

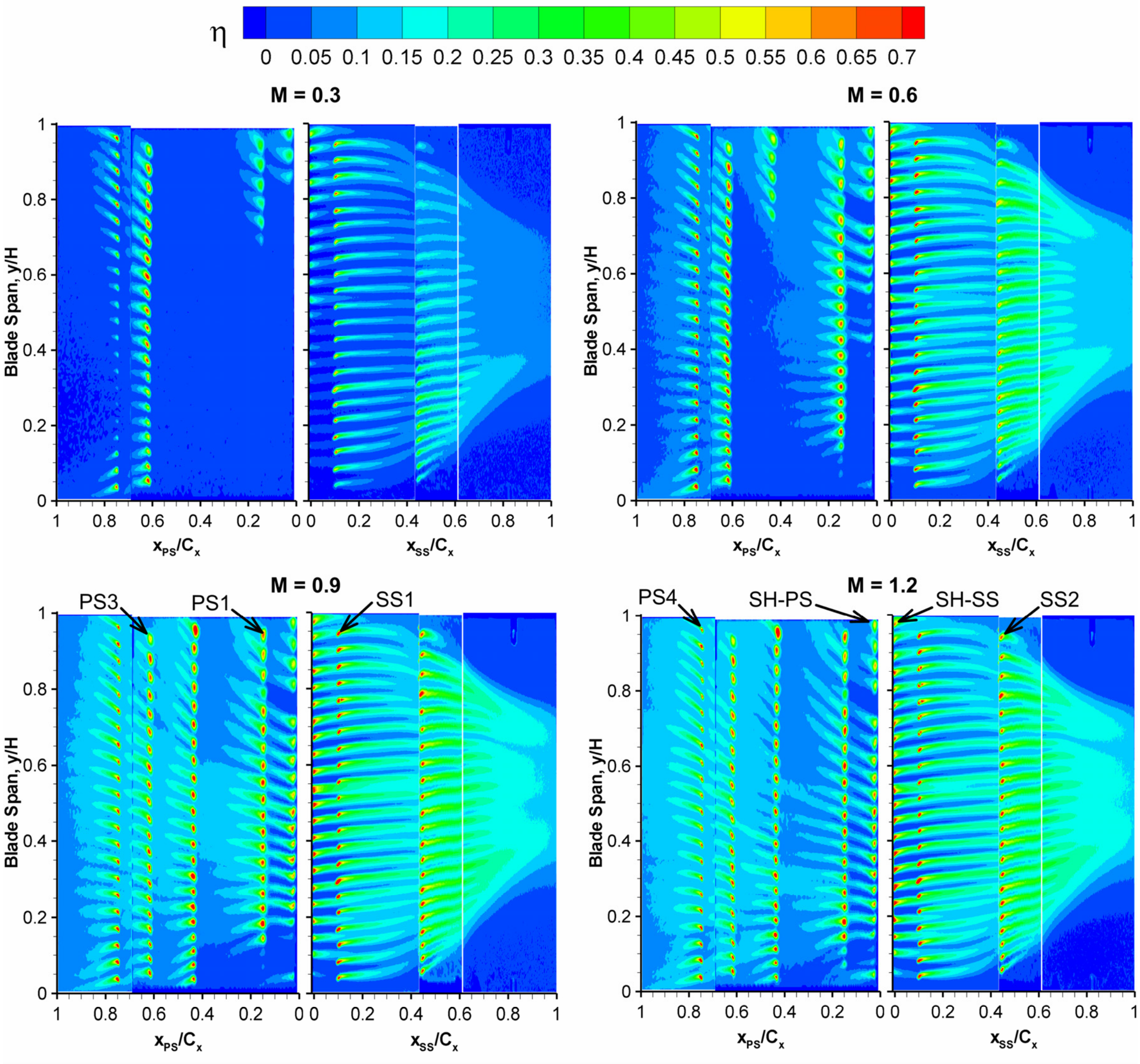

Fig. 3.9 Contour plots of film cooling effectiveness distributions with no wake

the pressure surface, hardly any coolant traces can be observed on the pressure surface for M = 0.3 from the showerhead rows and PS1 and PS2 rows. In fact, for cavity 2, all the coolant is diverted to the SS2 row with no coolant ejecting from the PS2 row. Some mainstream ingestion may also occur at these low blowing ratios.

As the blowing ratio is increased, the internal cavity pressure also increases resulting in more coolant ejection from the pressure side rows. However, even at high blowing ratios (M = 0.9 and 1.2) coolant traces from the showerhead and PS1 rows on the pressure side close to the hub are weak due to high external blade pressures near the leading edge and low internal static pressures in the cavity. A blowing ratio of M = 0.9 is found to give the strongest film effectiveness traces on both the pressure and suction sides. For a higher blowing ratio (M = 1.2), the high effectiveness trace near the hole rows is slightly shorter indicating that the higher momentum coolant jet for M = 1.2 ejecting from the film hole mixes with the mainstream more than that for M = 0.9 before attaching to the surface. Lift off of the coolant jet can also be observed for M = 1.2 for the PS2 row. No coolant ejection at low blowing ratios (M = 0.3 and 0.6) and jet liftoff at high blowing ratio (M = 1.2) indicates that the effectiveness from the PS2 row is very sensitive to the blowing ratio. The PS2 row is located on the blade where maximum blade curvature occurs. The lowest velocity on the pressure surface (Fig. 3.5) along with high static pressure occurs near the PS2 row location which may explain the above observation.

Film cooling distribution on the suction side is spanwise periodic with an axial coolant trace occurring at each hole location. Strong individual traces can be observed as the coolant remains attached to the convex suction surface. Flow acceleration due to the reducing passage cross-sectional area and bulk movement of the flow from the pressure to the suction side may cause this extended coolant streak. On the pressure side though, more spreading of the coolant traces is observed. The concave pressure surface results in an adverse pressure gradient near the leading edge resulting in flow deceleration whereas a favorable pressure gradient exists near the trailing edge as the flow approaches the throat resulting in flow acceleration (Fig. 3.6). This leads to thickening of the boundary layer near the leading edge and thinning as the flow progresses over the blade. The decelerating flow promotes mixing which causes shortening and smearing of the coolant trace.

Another important observation that can be made from the contour plots for the pressure and the suction sides is the direction which the coolant follows upon ejection through the film holes. The coolant is injected at an axial angle of 45^o to the surface pointing towards the blade tip. The mainstream flow is sufficiently strong to deflect this angled jet in the axial flow direction. This is particularly true for the suction side which experiences higher freestream velocities. The coolant traces are almost axial with some inward deflection for the traces near the hub and the tip caused mostly due to the passage and tip vortices. At $x/C_x \sim 0.3$ near the hub and tip, slight coolant trace deflection can be observed on the suction side. This may indicate the inception of the passage vortex attachment and the tip vortex resulting from the tip clearance gap respectively. Both these vortices have an adverse impact on the film cooling effectiveness distribution. The rotating action of these vortices scoops and pushes the coolant towards the

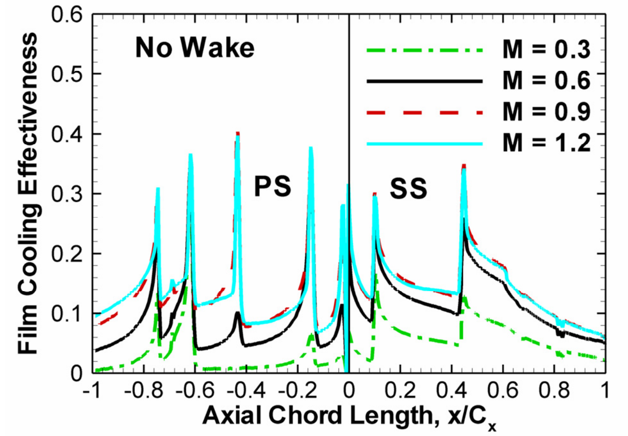

Fig. 3.10 Spanwise averaged film cooling effectiveness distributions with no wake

blade midspan. The effect of the passage vortex extends to almost 30% of the blade span near the trailing edge with the tip vortex effect extending upto 25%. The coolant pathlines on the pressure side are more complicated and follow the mainstream pathlines. For about 25% of the blade span near the hub, the coolant traces are deflected downward towards the hub whereas for about 40% of the blade span near the tip (y/H = 0.6 to 1), the coolant appears to flow towards the tip. Near the hub, the downward movement of the coolant trace may be due to the pressure side leg of the horseshoe vortex formed due to the upstream inlet boundary layer thickness. The rotating action of this vortex which eventually grows into the passage vortex bends the pathlines on the pressure surface downward towards the hub causing the observed deflection in the coolant traces. Near the tip though, the mainstream tries to flow through the tip gap due to the large pressure gradient across the pressure and suction sides. This causes the pathlines close to the tip to diverge from the axial flow direction. Around the midspan region, the mainstream flow at the cascade inlet exhibits inviscid behavior and coolant traces remain near axial.

Figure 3.10 shows the spanwise averaged film cooling effectiveness distribution for the pressure side (negative x-axis) and suction side (positive x axis) for all blowing ratios with no wake against the normalized axial chord length. Highest effectiveness magnitudes are observed for M = 0.9. Effectiveness magnitudes for M = 1.2 are similar to M = 0.9 but lower immediately downstream of a hole row. Overall average effectiveness on the pressure side is lower than suction side even though the pressure side has 4 rows of holes against 2 rows on the suction side. Effectiveness magnitudes fall sharply to less than 0.1 downstream of the holes for the pressure surface while for the suction surface the fall is less dramatic. Coolant accumulation near the trailing edge results in comparatively higher effectiveness for both blade surfaces. The SS1 row shows higher effectiveness as compared to the PS1 row. The thinner boundary layer on the pressure side may result in smearing of the coolant trace on the pressure side resulting in lower effectiveness. It should be also noted that for a certain axial chord distance, the suction side has a longer surface curvature length than the pressure side.

3.5.2. Showerhead Film Cooling Effectiveness under No Wake

Figure 3.11 shows the contour plots for the film cooling effectiveness distribution on the pressure and suction sides for mainstream flow with no wake. Contour plots are shown for three blowing ratios. One of the most striking features that can be observed from the contour data is the difference in effectiveness levels between the pressure and suction sides. The concave pressure surface results in a adverse pressure gradient on the blade surface near the leading edge. Flow deceleration near the leading edge (Figure 3.6) promotes mixing which causes shortening and smearing of the coolant trace. On the other hand, flow acceleration on the convex suction surface due to the reducing passage cross-sectional area and bulk movement of the flow from the pressure to the suction side may cause this extended coolant streak.

The higher pressure close to the tip in the first cavity might result in higher coolant mass flow through the holes which explains the weak traces near the hub for $M = 0.6$. As the coolant mass flow is increased with increasing blowing ratio, a more uniform distribution in film cooling effectiveness along the span can be observed. A blowing ratio of $M = 0.9$ is found to give the strongest film effectiveness trace on the pressure side close to the leading edge similar to that observed for full coverage film cooling. For a higher blowing ratio, the high effectiveness trace near the leading edge ($x/C_x < 0.15$) is slightly shorter indicating that the higher momentum coolant jet for $M = 1.2$ ejecting from the film hole mixes with the mainstream slightly more than that for $M = 0.9$ before attaching to the surface. In general, film cooling effectiveness from the middle stagnation hole row (SH-ST) is not significant. High stagnation pressure at the leading edge may prevent coolant to exit from this row, with more coolant being diverted towards the pressure and suction side rows. Some ingestion of the mainstream flow through this hole row may also be possible for low blowing ratios.

Film cooling distribution on the suction side is spanwise periodic with an axial coolant trace occurring at each hole location. The local blowing ratio for the suction side row (SH-SS) may be higher than that on the pressure side. This may be due to lower static pressure at this row

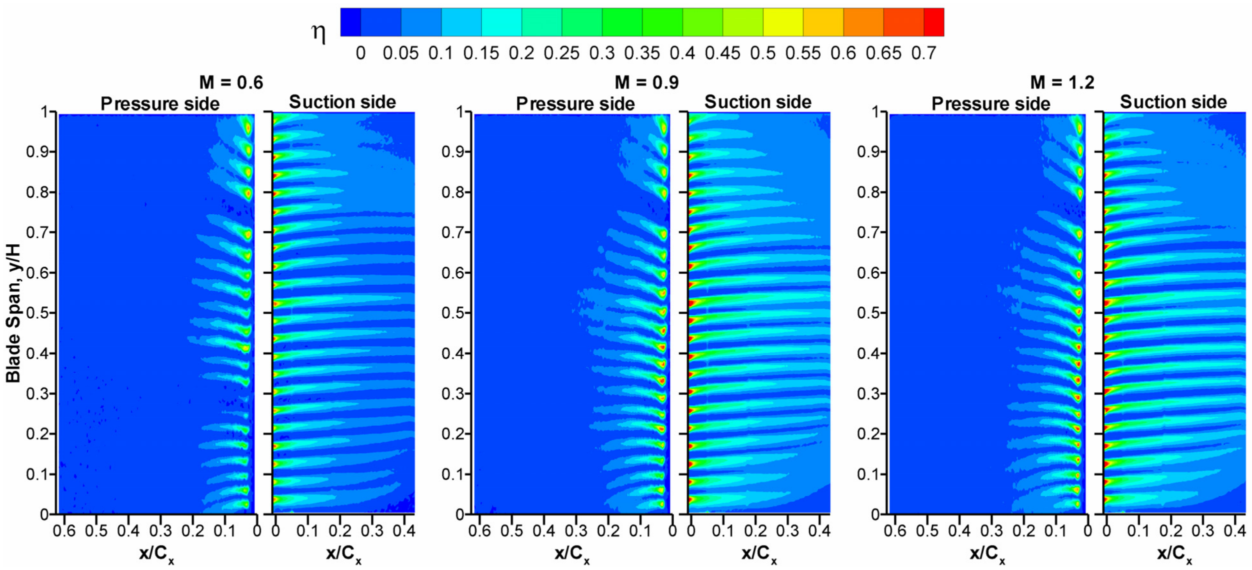

Fig. 3.11 Contour plots of showerhead film cooling effectiveness distributions with no wake

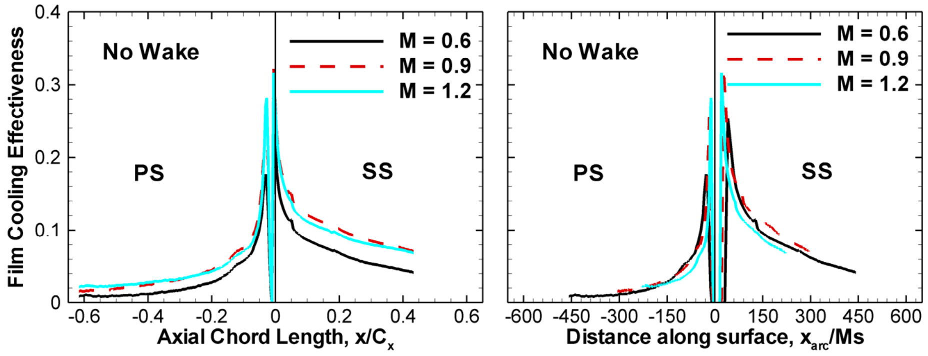

(a) **(b)**

Fig. 3.12 Spanwise averaged showerhead film cooling effectiveness distributions with no wake

location (SH-SS) on the outer blade surface as a result of mainstream flow acceleration on the concave suction side than on the pressure side row location (SH-PS). Static pressure measurements on a blade machined with pressure taps showed that the static pressure near row SH-SS (P_{SH-SS} (gage) = 9,100Pa) is about 55% of the stagnation pressure at row SH-ST (P_{SH-ST} (gage) = 16,500Pa). Strong traces can be observed even at large axial distances as the coolant remains attached to the convex suction surface. A blowing ratio of M = 0.9 gives the strongest coolant trace similar to that observed for the pressure side.

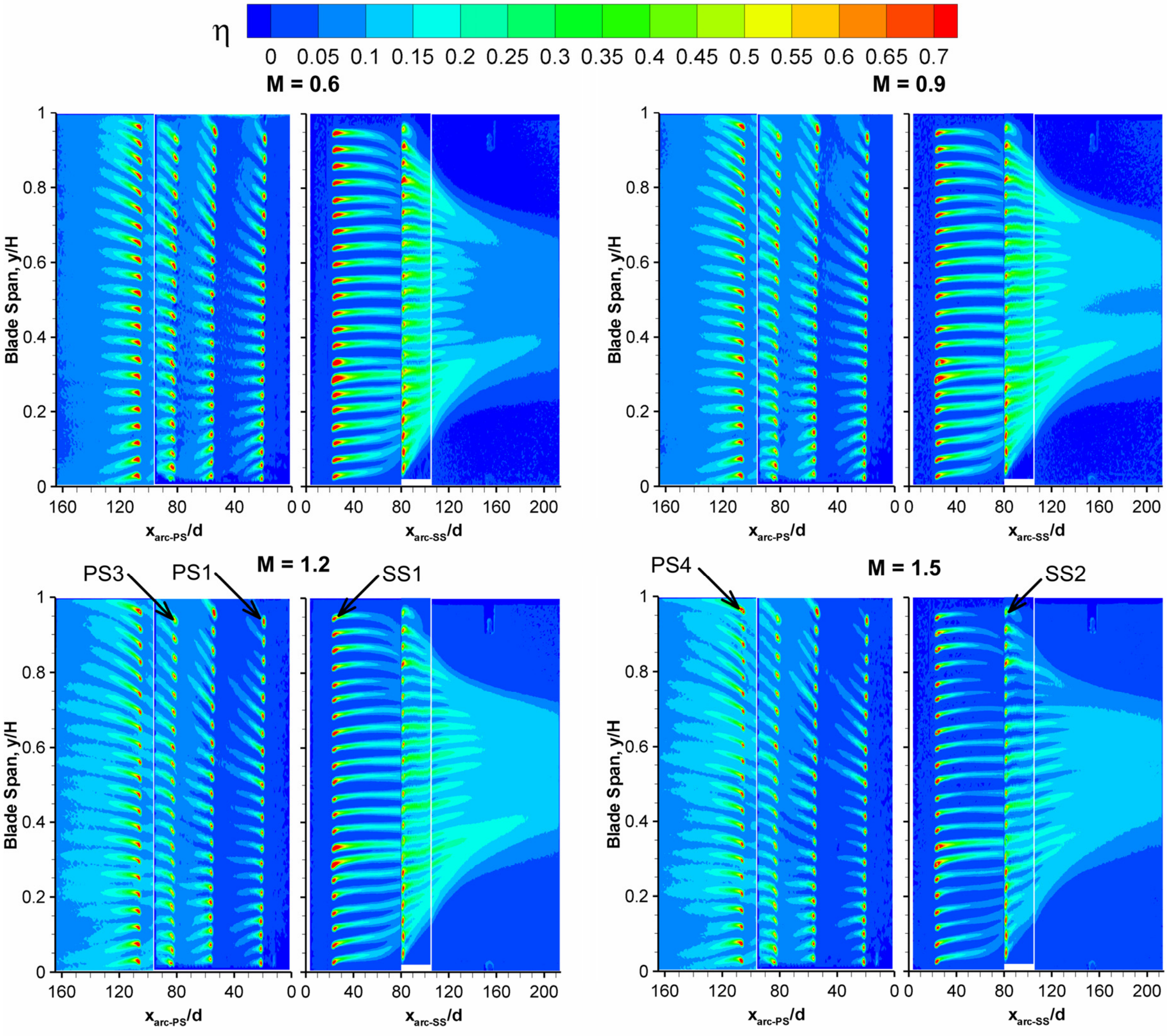

Fig. 3.13 Contour plots of full coverage film cooling without showerhead ejection

Figure 3.12(a) shows the spanwise averaged film cooling effectiveness distribution for the pressure side (negative x-axis) and suction side (positive x axis) for all three blowing ratios with no wake against the normalized axial chord length. Highest effectiveness magnitudes are observed for M = 0.9. Effectiveness magnitudes for M = 1.2 are marginally lower than those for M = 0.9. A higher blowing ratio results in a stronger coolant jet which promotes mixing with the mainstream and hence results in lower film effectiveness. The showerhead design used in this study gives good film coverage in the region very close to the leading edge ($x/C_x < 0.1$) with average effectiveness magnitudes of about 0.2. The effectiveness magnitude though decreases rapidly as the axial distance increases. The spanwise averaged effectiveness magnitude drops below 0.15 at axial chord distances of 0.1 from the leading edge even for the highest blowing ratios. It should be noted that for a certain axial chord distance, the suction side has a longer surface curvature length than the pressure side. This can be discerned from Fig. 3.12(b) which plots the same spanwise averaged effectiveness data against the curve length starting from the stagnation point on the leading edge. This surface curvature length is normalized with the blowing ratio, M and equivalent slot width of a hole row, s. As observed from Fig. 3.11, the effectiveness on the pressure side decays much faster than that on the suction side especially for low blowing ratios.

3.5.3. Film Cooling Effectiveness on Blade Span without Showerhead Ejection and without Wake

Figure 3.13 shows the contour plots for the film cooling effectiveness distribution on the pressure and suction sides for all four blowing ratios. Film cooling distribution on the curved blade surface obtained has been plotted against the normalized actual surface distance starting from the stagnation line along the blade curved surfaces.

Effectiveness magnitudes near the leading edge are noticeably lower than those for full coverage film cooling due to absence of showerhead injection. A blowing ratio of M = 0.6 is found to give the strongest film effectiveness traces on both the pressure and suction sides immediately downstream of the holes. It should be noted that while investigating film cooling on the pressure side, the suction side hole rows were sealed and vice-versa. As the blowing ratio is increased (M = 0.9 and 1.2), the effectiveness levels near the holes drop but far downstream of the holes, the effectiveness levels show an increase due to coolant accumulation. This effect can be clearly observed on the suction surface downstream of the SS2 hole row and close to the trailing edge. For a higher blowing ratio, the shorter high effectiveness trace near the hole rows indicates that the higher momentum coolant jet ejecting from the film hole mixes with the mainstream more before attaching to the surface. For high blowing ratios (M = 1.2 and 1.5), lift off of the coolant jet can be observed for the PS1 and PS2 rows particularly near the blade tip region. Lift off is indicated by the sudden drop in effectiveness levels immediately downstream of the holes with magnitudes close to zero.

Film cooling holes #7 and #8 from the hub in the SS1 row show a very high effectiveness trace as compared to the other holes in the same row. The hole breakout surface for these holes

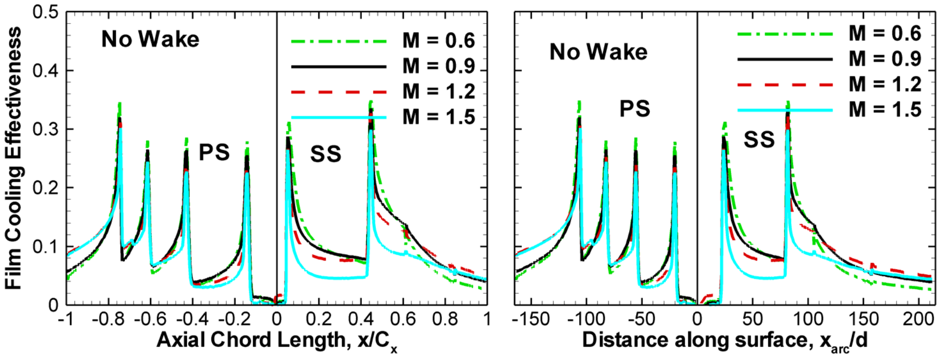

Fig. 3.14 Spanwise averaged full coverage film cooling distributions without showerhead ejection

was damaged during manufacturing of the blade resulting in a breakout profile resembling a shaped hole. This might explain the high effectiveness trace from these holes. On the pressure side though, more spreading of the coolant traces is observed similar to results for full coverage film cooling. Smearing of the coolant trace due to decelerating flow on the pressure side can be observed for the PS1 and PS2 rows. The coolant traces disappear within ~1cm of injection (~16d). Progressively longer traces can be observed for the PS3 and PS4 rows as they lie in the accelerating flow region.

Figure 3.14 shows the spanwise averaged film cooling effectiveness distribution for the pressure side (negative x-axis) and suction side (positive x axis) for all blowing ratios against the normalized axial chord length and also the normalized surface curvature length. Each peak corresponds to the location of the film cooling hole row. Highest effectiveness magnitudes immediately downstream of the holes are observed for M = 0.6. However, the coolant trace for M = 0.6 decays much faster. A blowing ratio of M = 1.2 gives best average effectiveness close to the trailing edge for both pressure and suction surfaces due to coolant accumulation from upstream holes. Overall average effectiveness on the pressure side is lower than suction side even though the pressure side has 4 rows of holes against 2 rows on the suction side. Effectiveness magnitudes fall sharply to less than 0.1 within 20 diameters downstream of the holes for the pressure surface while for the suction surface the fall is less dramatic. Coolant accumulation near the trailing edge results in relatively high effectiveness for both blade surfaces. As observed from the contour plots in Fig. 3.13, film cooling effectiveness from the PS1 and PS2 rows is lower than corresponding rows on the suction side. Experimental results from Drost and Bolcs [57] for a single row of holes on the pressure and suction sides indicate

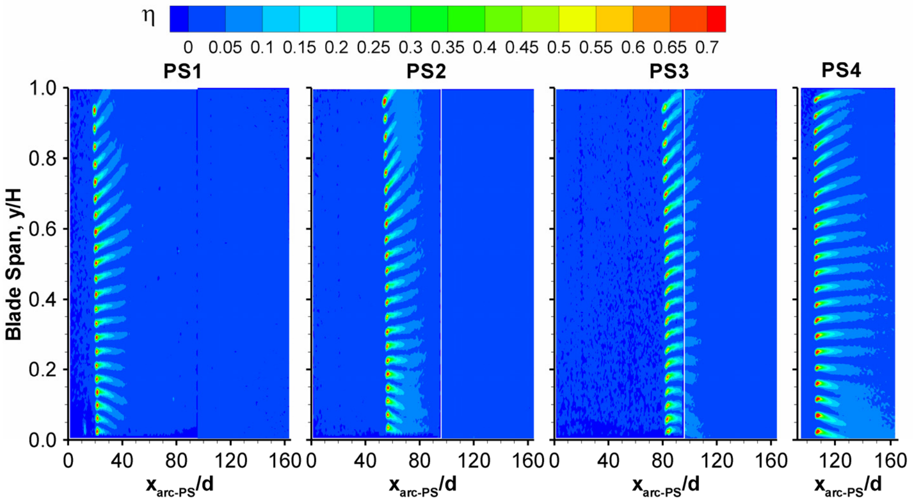

Fig. 3.15 Contour plots of film cooling effectiveness for individual rows on the pressure side, M = 0.9

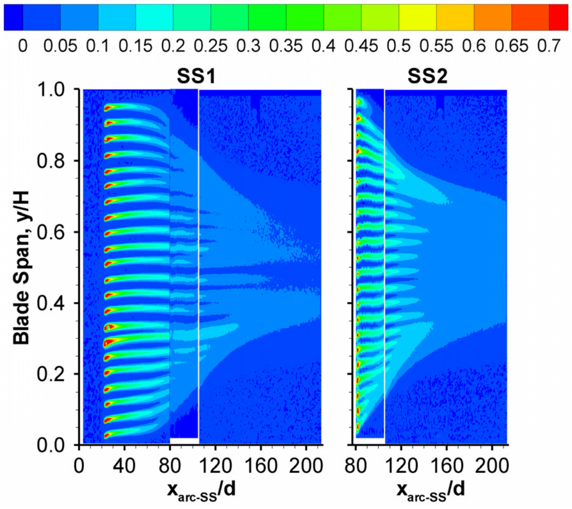

Fig. 3.16 Contour plots of film cooling effectiveness for individual rows on the suction side, M = 0.9

that best heat flux reduction occurs for a blowing ratio of 0.53 near the holes. Lower blowing ratios were found to give high effectiveness just downstream of the hole row. Extended coolant streaks were also observed on the suction side whereas on the pressure side, the traces disappeared quickly within 20 hole diameters similar to that observed the present study.

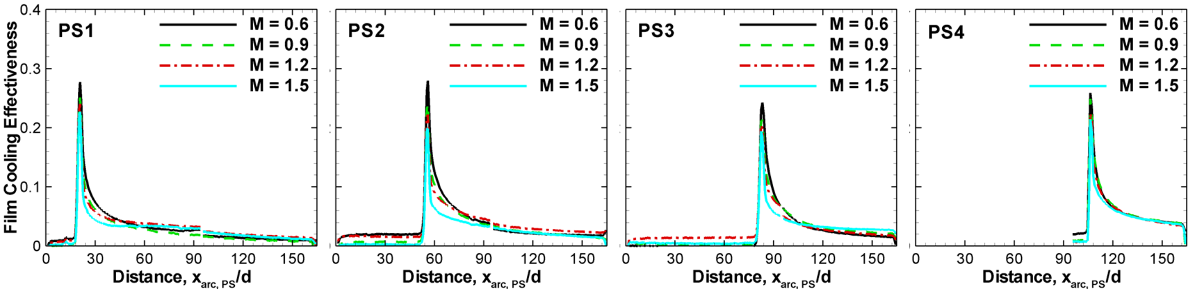

Fig. 3.17 Effect of blowing ratio on spanwise averaged film cooling effectiveness distributions on the pressure side

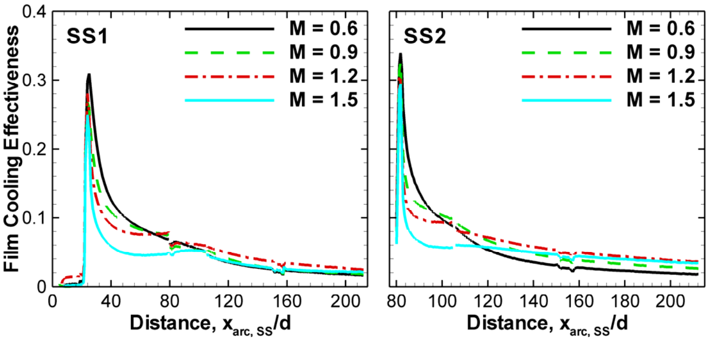

Fig. 3.18 Effect of blowing ratio on spanwise averaged film cooling effectiveness distributions on the suction side

3.5.4. Film Cooling Effectiveness Distribution from Individual Row Ejection

Figures 3.15 and 3.16 show the contour plots of film cooling effectiveness from individual rows for M = 0.9 on the pressure and suction sides respectively. Contour data for other blowing ratios is not shown due to space limitations. Results for the pressure side in Fig. 3.15 indicate that the coolant trace fades away completely within 20 to 30 diameters from injection. This observation is consistent with the results for full coverage film cooling on the pressure side where the coolant traces dissolve rapidly into the mainstream. The effectiveness levels for the PS1 row in Fig. 3.15 are similar to those observed from the PS1 row for full coverage film cooling. Higher effectiveness due to coolant accumulation is observed after the PS2 hole row for full coverage film cooling. Coolant traces for the PS4 hole row are relatively longer. High flow acceleration (Fig. 3.6) as the flow approaches the throat may explain these extended coolant streaks. Coolant streaks on the suction side shown in Fig. 3.16 for M = 0.9 are much longer as

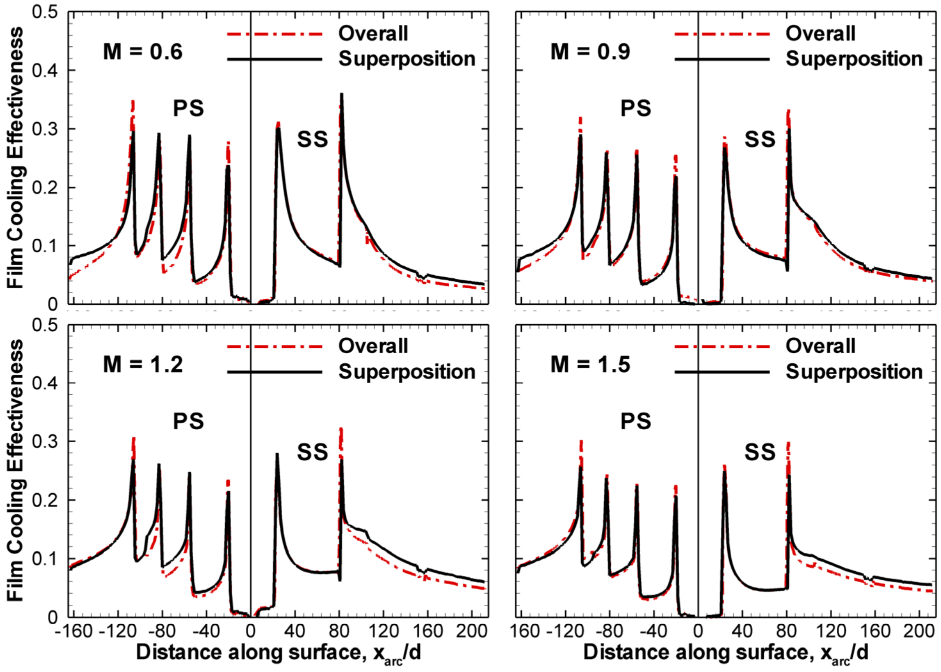

Fig. 3.19 Comparison of spanwise film cooling effectiveness from superposition of individual rows and with all film holes blowing (overall)

compared to the pressure side. Coolant traces from the SS1 row persist till the trailing edge of the blade. The contraction effect of the tip and passage vortex on the coolant traces as discussed in the preceding section can also be observed in Fig. 3.16. Also, each individual coolant trace shows higher magnitudes as compared to those from the pressure side in Fig. 3.15.

Figures 3.17 and 3.18 show the spanwise averaged film cooling effectiveness results for all blowing ratios for the pressure and suction sides respectively. A blowing ratio of 0.6 shows highest effectiveness magnitudes immediately downstream of the holes similar to that observed for full coverage film cooling. Increasing blowing ratio gives progressively lower effectiveness magnitudes. The highest blowing ratio (M = 1.5) gives the lowest magnitude downstream of the holes as the high momentum jets tend to mix with the mainstream. The film cooling effectiveness distributions on the pressure side for rows PS1, PS2 and PS3 are self-similar. For the PS4 row, the spanwise averaged magnitudes for all four blowing ratios are slightly higher and similar to each other. The drop in magnitudes for the suction side hole rows with increasing blowing ratio is much higher as compared to the pressure side. However, higher blowing ratios give better effectiveness far downstream of the hole row. A blowing ratio of 1.2 results in best effectiveness at distances greater than 45 hole diameters.

Figure 3.19 shows the spanwise averaged film cooling effectiveness from superposition of individual rows and with all film holes blowing for all the blowing ratios. The film cooling effectiveness from superposition as discussed by Sellers [67] is calculated from Eq. 3.2.

$$\eta_s = \sum_{i=1}^{n} \eta_i \prod_{j=0}^{i-1} \left(1-\eta_j\right) \quad where \quad \eta_0 = 0 \tag{3.2}$$

Effectiveness from superposition compares reasonably well with full coverage film cooling on both pressure and suction surfaces. Results from superposition indicate a smaller drop in film cooling effectiveness downstream of the holes. However, the peak difference between the overall and superposition results in small with a magnitude of only about 0.03 units. This indicates that the superposition principle can be successfully applied to predict film cooling in the absence of showerhead film cooling. Similar observations were made by Schneider et al. [73] who investigated this effect with and without showerhead cooling on the pressure side. Good agreement was found between individual row and multiple row measurements using the superposition approach without showerhead injection. However, showerhead injection caused degradation in full coverage effectiveness in the downstream rows resulting in over-prediction of the superposition effectiveness magnitudes. Effect of showerhead injection was also studied by Polanka et al. [70] and Cutbirth and Bogard [71, 72] as discussed in the Introduction.

3.5.5. Effect of Stationary, Unsteady Wake on Full Coverage Film Cooling Effectiveness

Figures 3.20 and 3.21 show the contour plots of film cooling effectiveness for wake rod diameters of 3.2mm and 4.8mm for 0% and 25% wake phase locations for M = 0.9 and M = 1.2 respectively. Contour data for other blowing ratios and phase locations is not shown due to space limitations. Film cooling on the pressure and suction sides is significantly damaged by the presence of wake rods at 0% and 25% phase locations as compared to the no wake case. For 0%, the rod is located directly upstream of the leading edge of the blade while for 25%, one rod is placed in the pressure side passage close of the film cooled blade while the second rod is close to the suction side of the test blade. Vortex shedding from the rod at 0% generates additional turbulence resulting in more mixing of the coolant with the mainstream. This mixing damages the film coverage near the leading edge. A conceptual view of the wake generated by the rods at different phase locations is shown in Fig. 3.4. The destructive effect of the wake from the 0% phase location can be observed as far as the PS4 row. For the 25% phase location, the wake rod

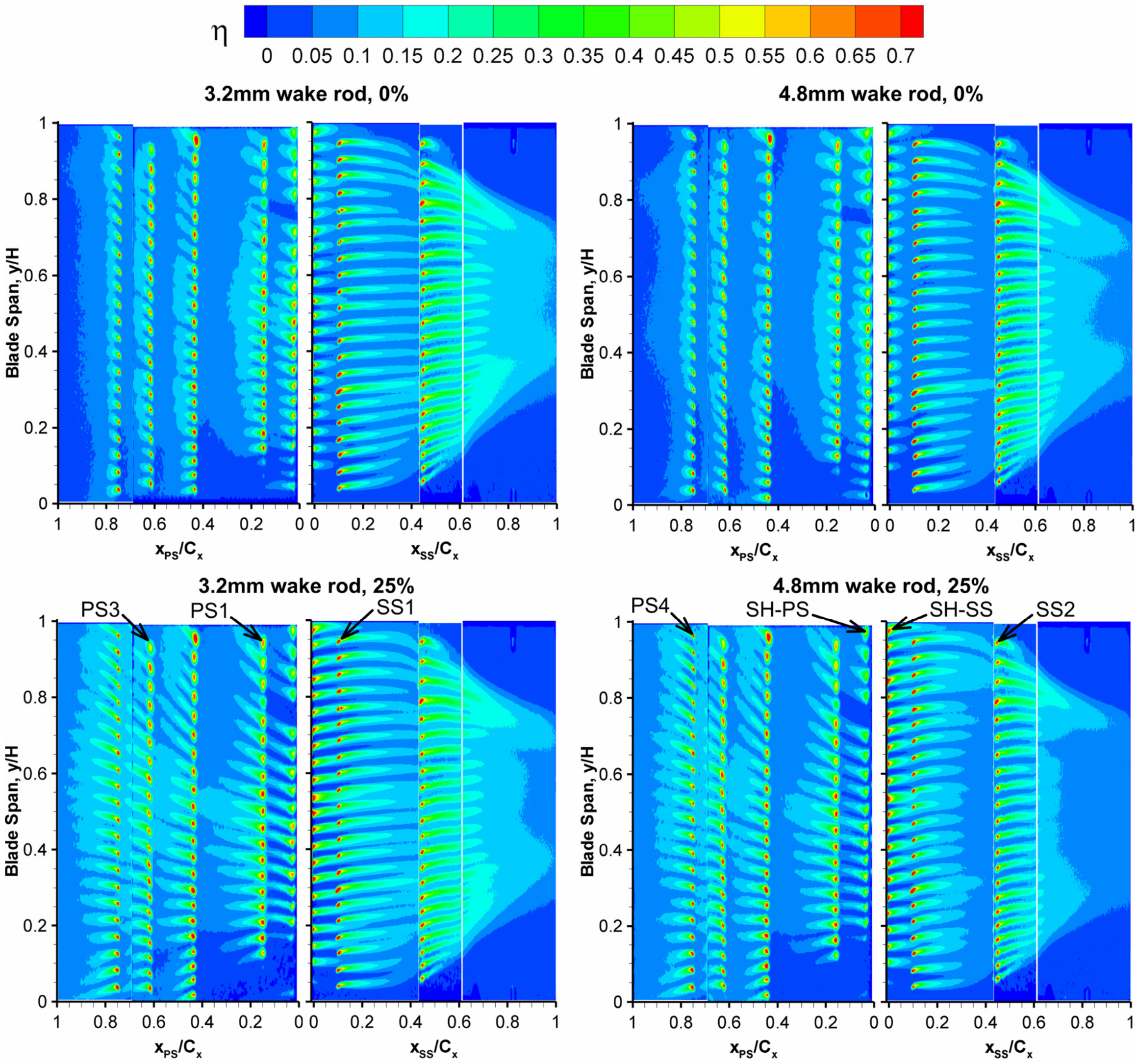

Fig. 3.20 Contour plots of full coverage film cooling distributions with unsteady wake for M = 0.9

located near the first guide blade in the pressure side passage is too far away from the test blade to affect the film cooling effectiveness. On the other hand, the wake rod placed upstream of the suction side passage of the test blade is closer to the blade than the rod at 0% phase location. This wake rod position has a major impact on the film effectiveness distribution on the suction side in the mid-chord region. Lower decay in the vortex shedding wake from the rod due to a smaller wake travel distance (Fig. 3.4) may cause this effect. The coolant traces near the leading edge for the 25% phase location are stronger than those for 0% while those near the mid-chord

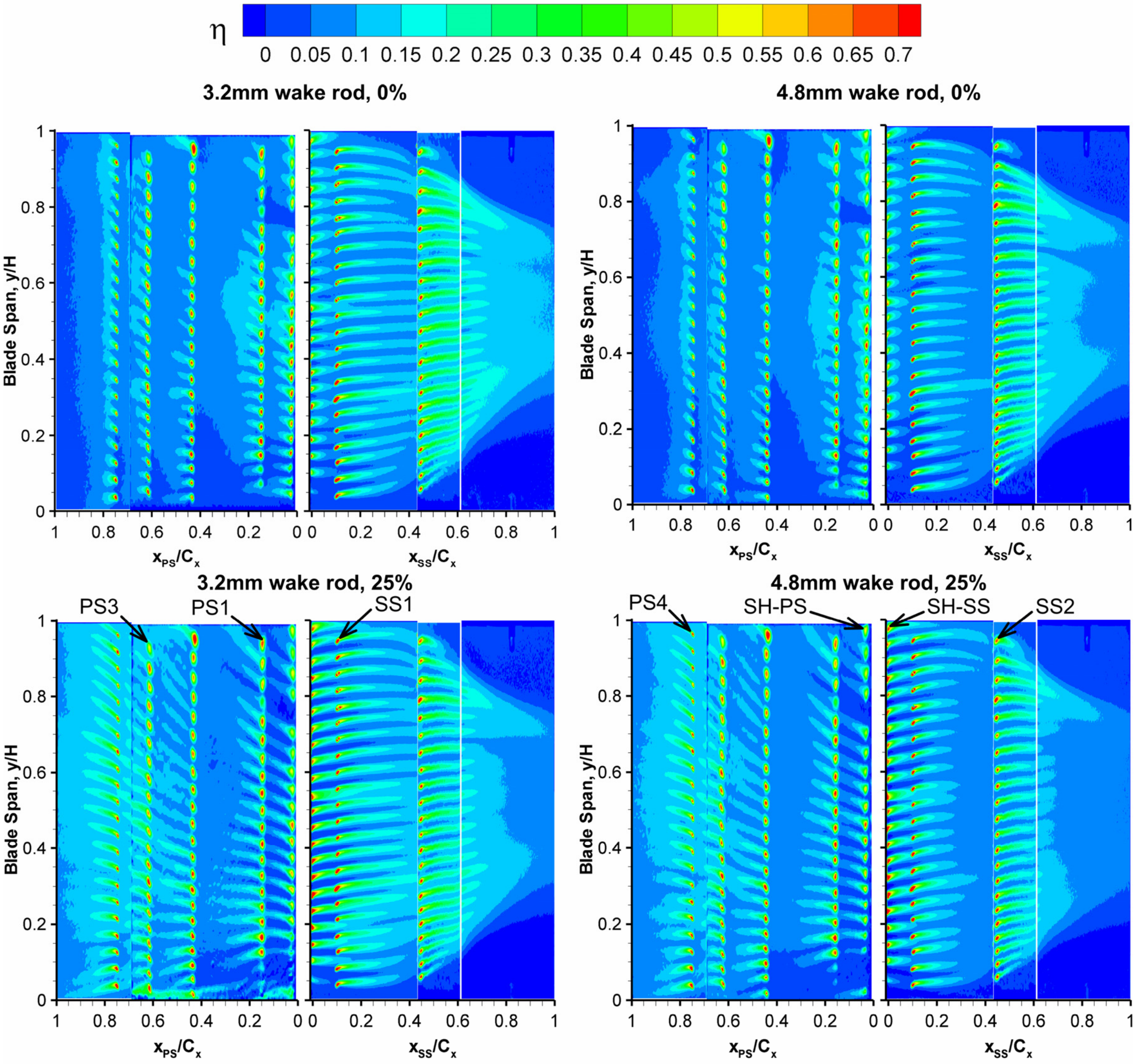

Fig. 3.21 Contour plots of full coverage film cooling distributions with unsteady wake for M = 1.2

region are weaker indicating the progression of the wake. A smaller reduction on the pressure side can be observed from the wake at 25% phase location as compared to 0%. The effect of wake rod diameter can also be observed from Figs. 3.20 and 3.21. The film cooling effectiveness distributions show lower effectiveness magnitudes for a larger wake rod diameter. A larger wake rod diameter will result in a stronger wake and consequently a higher wake Strouhal number.

Figures 3.22 and 3.23 show the variation in the spanwise averaged film cooling effectiveness for different blowing ratios for all wake rod diameters and phase locations for the pressure and suction side respectively. The trends obtained for data with wake are similar to those for the no wake case. A blowing ratio of 0.9 shows the best results for the pressure as well as suction sides for all rows. The drop in effectiveness for M = 1.2 just downstream of a hole row on the pressure side is much sharper as compared to M = 0.9. Figures 3.24 and 3.25 show the effect of a stationary, unsteady wake on the spanwise averaged film effectiveness for all blowing ratios for the pressure and suction side respectively. The data has been compared to the effectiveness results for no wake, which serves as a reference case. Results for 2 wake rod diameters and 4 phase locations are presented. The destructive effect of the wake can be clearly observed from the spanwise averaged plots for the two wake rod sizes for the 0% and 25% phase locations. The film cooling results for no wake, 50% and 75% phase locations are identical indicating that the vortex shedding from the rods at these locations does not attach to the pressure and suction surfaces (Fig. 3.4). Since these rods are further upstream of the leading edge on the pressure side of the test blade, the vortices shedding downstream of the rods may decay sufficiently so as to not affect the film cooling distribution.

For the 0% phase location, degradation in film coverage on the pressure side is by an effectiveness magnitude of as much as 0.1 for the larger wake rod as compared to the no wake case whereas for the suction side, the spanwise average effectiveness magnitudes decreases by a smaller amount (upto 0.08). For the 25% phase location, the decrease in effectiveness from the no wake reference case due to the stationary, unsteady wake is larger for the suction side as compared to the pressure side and the magnitudes are similar to those for the 0% phase location. This effect is similar to that observed from the contour plots in Figs. 3.20 and 3.21 and is due to the wake rod at this phase location being closer to the suction side of the test blade. On the pressure side, the damaging effect of the wake from the 25% phase location is more prominent near the leading edge of the blade for film hole rows, SH-PS, PS1 and PS2. Further downstream towards the trailing edge, the destructive effect of the wake disappears. Also, a larger wake rod diameter has a higher decremental impact on the film cooling effectiveness distribution. The results from this study compare favorably with those from Ou et al. [51] and Mehendale et al. [52]. Film cooling tests performed by them in a similar high pressure turbine rotor blade cascade mounted in a low speed wind tunnel with an upstream rotating wake generator indicate that film injection with air gives better film coverage for M = 0.8 as compared to M = 0.4 and M = 1.2.

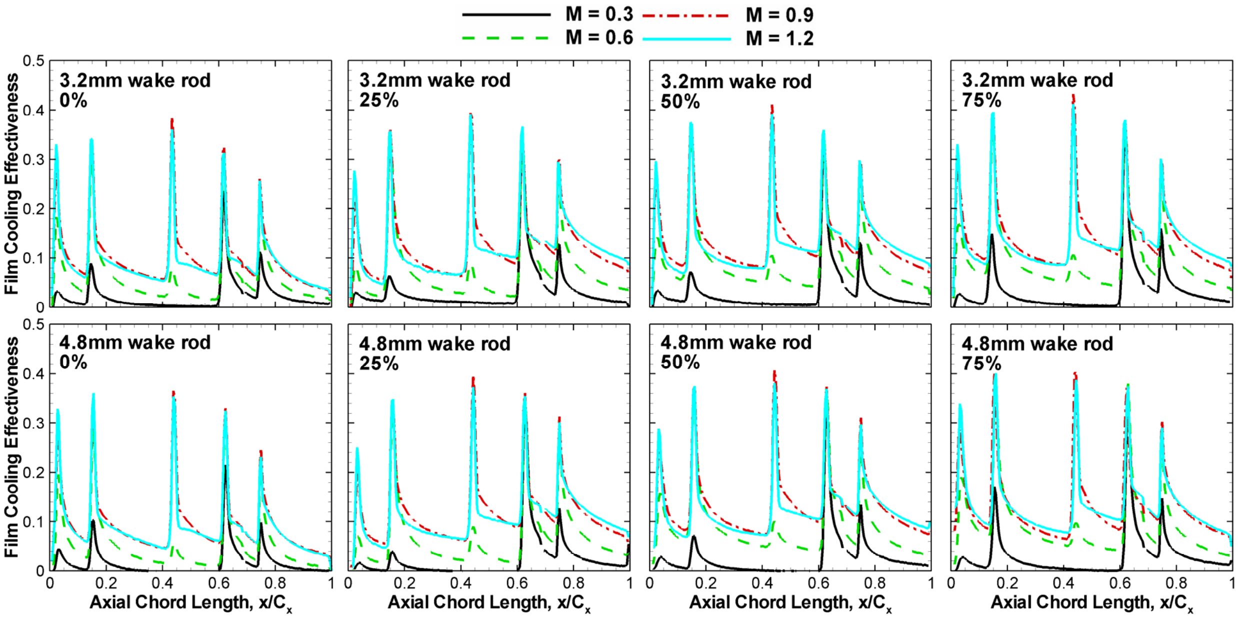

Fig. 3.22 Effect of blowing ratio on spanwise averaged full coverage film cooling effectiveness distributions on the pressure side

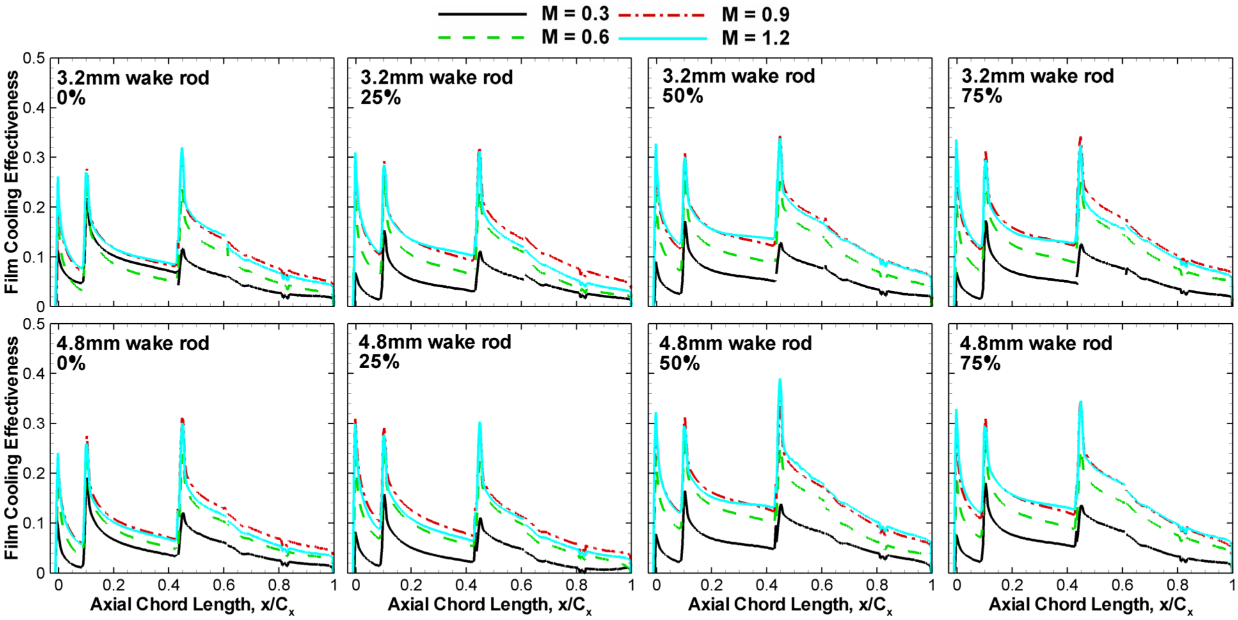

Fig. 3.23 Effect of blowing ratio on spanwise averaged full coverage film cooling effectiveness distributions on the suction side

Significant degradation in film coverage was also noticed in the presence of an unsteady wake. Similar observations were made by Ekkad et al. [53] with combined effect of freestream

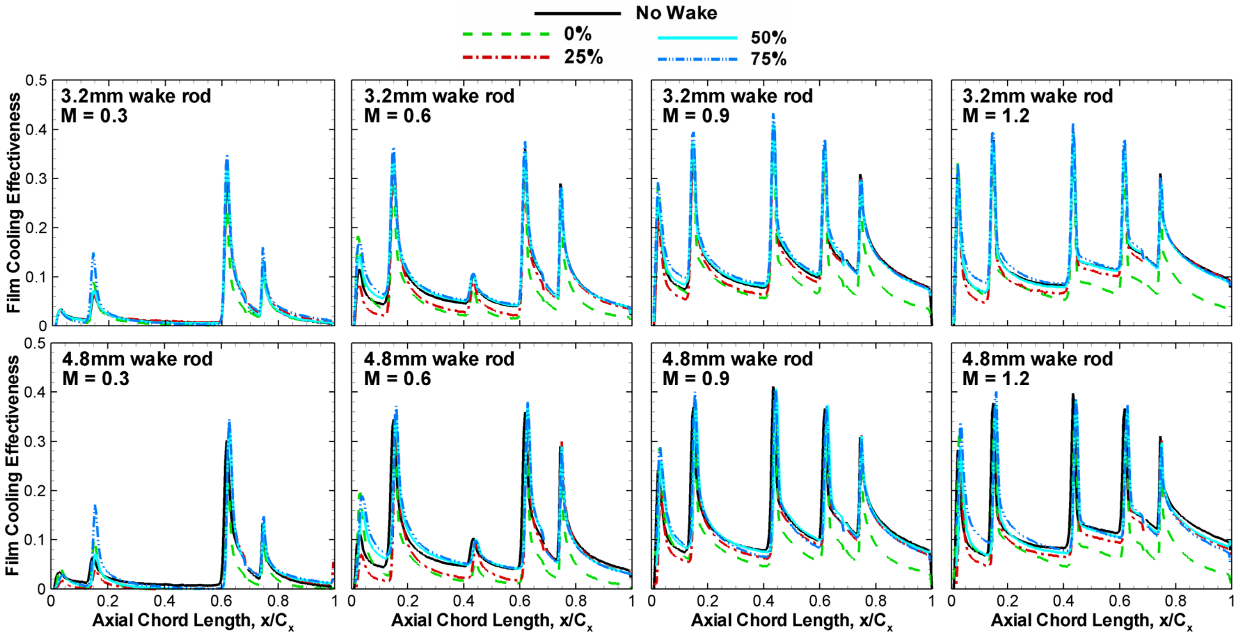

Fig. 3.24 Effect of unsteady wake on spanwise averaged full coverage film cooling effectiveness distributions on the pressure side.

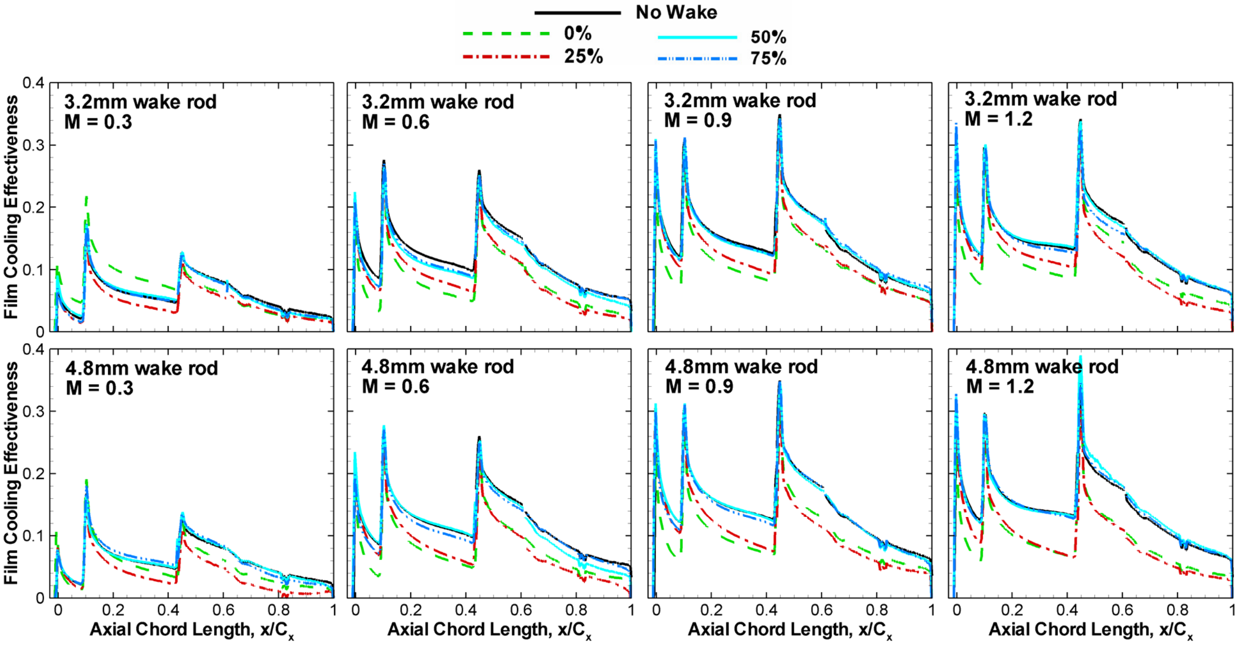

Fig. 3.25 Effect of unsteady wake on spanwise averaged full coverage film cooling effectiveness distributions on the suction side.

turbulence and unsteady wake and by Du et al. [54] with an unsteady wake from local measurements using the transient liquid crystal technique for the same cascade.

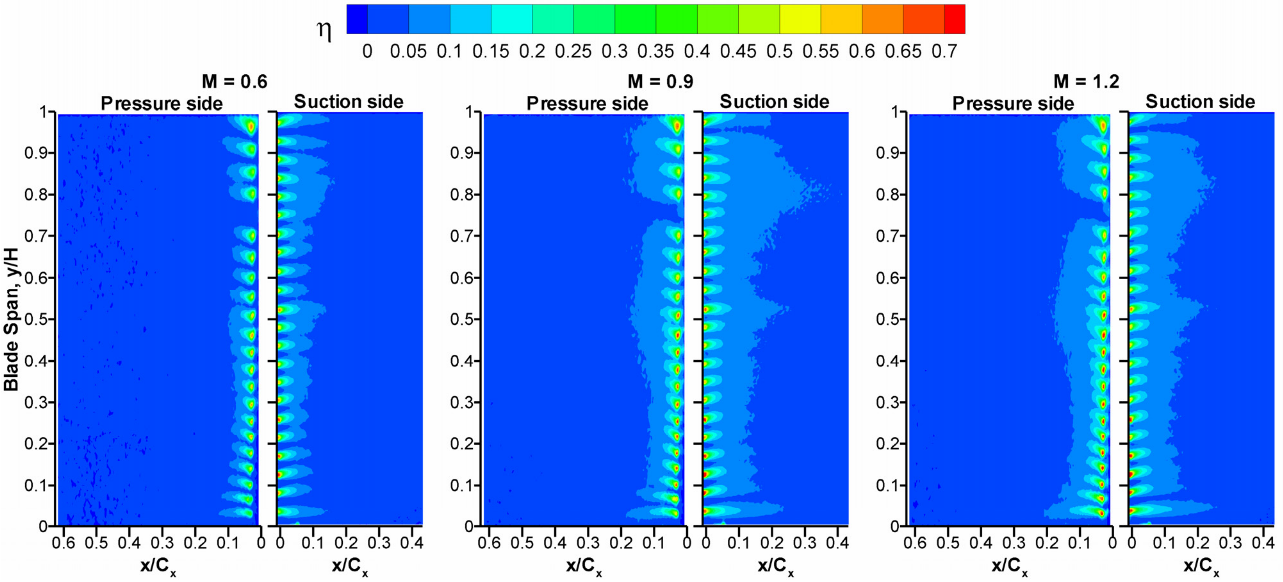

Fig. 3.26 Contour plots of showerhead film cooling distributions for 4.8mm wake rod at 0% wake location

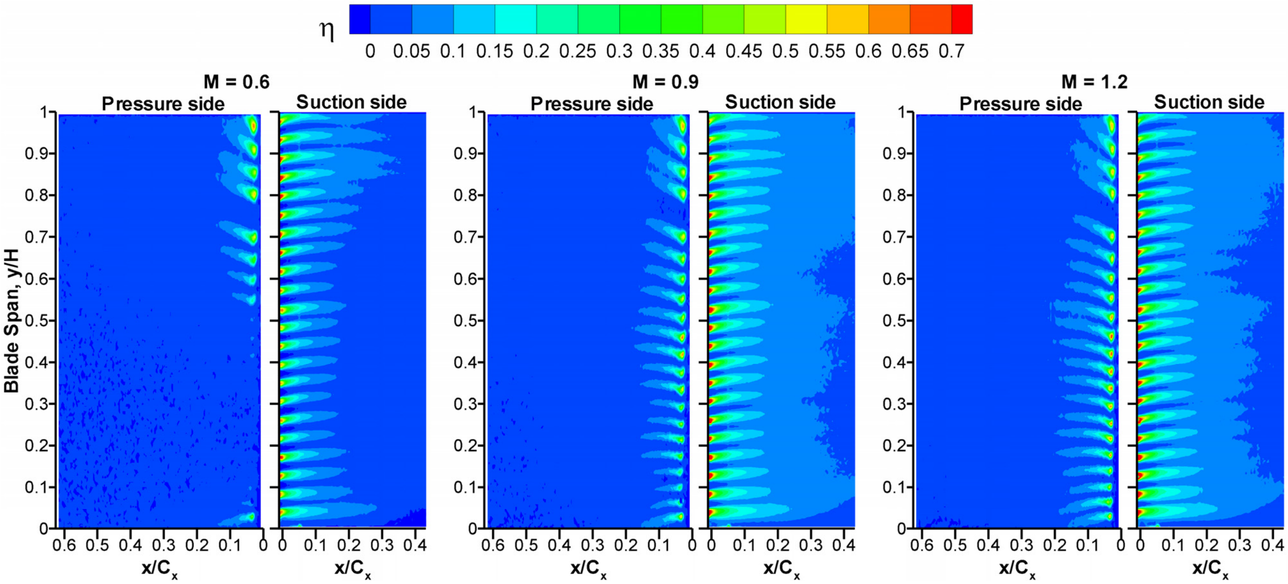

Fig. 3.27 Contour plots of showerhead film cooling distributions for 4.8mm wake rod at 25% wake location

3.5.6. Effect of Stationary, Unsteady Wake on Showerhead Film Cooling Effectiveness

Figures 3.26 and 3.27 show the contour plots of showerhead film cooling effectiveness for the 0% and 25% wake phase locations for three blowing ratios respectively for the 3.2mm wake

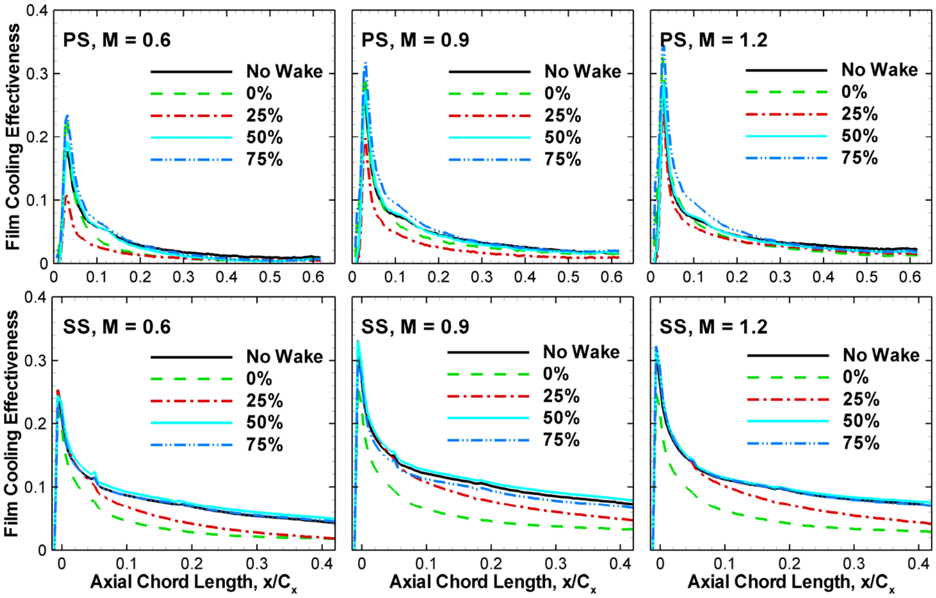

Fig. 3.28 Effect of unsteady wake on spanwise averaged showerhead film cooling effectiveness distributions on the pressure (top row) and suction sides (bottom row)

rod. Film cooling on the pressure and suction sides is significantly damaged by the presence of wake rods at 0% and 25% phase locations as compared to the no wake case. This observation is consistent with the unsteady wake results for full coverage film cooling described in the previous section.

Figure 3.28 show the effect of a stationary, unsteady wake on the spanwise averaged film effectiveness for three blowing ratios for the pressure and suction side respectively. The data has been compared to the effectiveness results for no wake, which serves as a reference case. Results for different phase locations of the wake rods are presented. The destructive effect of the wake can be clearly observed from the spanwise averaged plots for the 4.8mm wake rod for the 0% and 25% phase locations. The film cooling results for no wake, 50% and 75% phase locations are identical indicating that the vortex shedding from the rods at these locations does not attach to the pressure and suction surfaces (Fig. 3.4). For the 0% phase location, degradation in film coverage on the suction side is as much as 50% (Fig. 3.26) at large axial lengths ($x/C_x >$ 0.1) as compared to the no wake case. For the 25% phase location, the unsteady wake results in effectiveness decreasing by about 20 to 25% from the no wake reference case. Results for effectiveness in the presence of a stationary, unsteady wake also indicate that the effectiveness magnitude for M = 1.2 is marginally lower than that for M = 0.9 but higher than that for M = 0.6 similar to that observed for no wake conditions. Ou et al. [51] and Mehendale et al. [52] showed that showerhead film injection with air gives better film coverage for M = 0.8 as compared to M = 0.4 and M = 1.2. Average effectiveness magnitudes were found to decrease by about 0.05 near the holes in the presence of rotating wake from no wake conditions. PSP measurements by Gao et al. [74] on a 2 row showerhead cylindrical leading edge model also gave better spanwise averaged film coverage far downstream of the holes for M = 0.8 than M = 0.4 and 1.2 with high freestream turbulence.

3.6. CONCLUSIONS

Experimental tests were performed on a high pressure turbine rotor blade for full coverage, showerhead and individual row film cooling. The effect of different blowing ratios, and the presence of a stationary, upstream wake used for simulating a rotating, unsteady wake are examined on blade film coverage. Film cooling effectiveness from superposition of individual rows is compared against overall film cooling. Some of the main conclusions that can be drawn from the presented results are:

1. A blowing ratio of 0.9 gives the best film coverage for showerhead and full coverage film cooling. Film cooling results for M = 1.2 are close to M = 0.9 suggesting that the optimal blowing ratio might be close to 1.0 for the blade.
2. Film cooling effectiveness on the suction side is higher than that for the pressure side for all cases observed.
3. At low blowing ratios for full coverage film cooling, coolant coverage on the pressure surface is compromised by the failure of coolant to eject from several film cooling holes. Mainstream ingestion may also occur at low blowing ratios on the pressure surface.
4. Film cooling rows on the pressure side should be located carefully after examining the pressure distribution over the blade. Film cooling holes near large blade curvatures should be avoided.
5. Showerhead film coverage is non-uniform on the pressure and suction sides. Rapid degradation in film cooling effectiveness is observed on the pressure side.

6. Coolant traces from showerhead film cooling persist at distances greater than 40% of the blade axial chord on the suction side. Effectiveness magnitudes of about 0.08 can be observed under no wake conditions at this location.
7. The showerhead design gives good film coverage close to the leading edge with an average magnitude greater than 0.2 for $x/C_x < 0.05$ for both pressure and suction sides.
8. Superposition from individual film cooling holes shows good agreement with spanwise averaged full coverage film cooling for both pressure and suction surfaces and for all blowing ratios in the absence of showerhead injection.
9. An upstream wake can have a severe detrimental impact on film coverage. Wake phase locations of 0% and 25% significantly decrease the film cooling effectiveness magnitudes. Wakes from 50% and 75% phase locations do not attach to the blade surfaces and hence, do not impact the film cooling effectiveness.
10. The decrease in effectiveness from the wake is more prominent on the suction side as both 0% and 25% phase locations contribute to this reduction.
11. A larger wake rod diameter results in a stronger wake which further decreases the film cooling effectiveness.

4. INTERNAL HEAT TRANSFER EXPERIMENTS IN A TURBULATED HIGH ASPECT RATIO CHANNEL

4.1. INTRODUCTION

The internal heat transfer experiments are designed to simulate combustor liner cooling in a gas turbine. The combustor is one of the hottest regions in a gas turbine and its walls must be uniformly cooled to avoid meltdown. Typical temperatures in the combustor core exceed 2000°C which is higher than the melting point of most metals. By utilizing advanced cooling concepts such flow over turbulated surfaces, the combustor walls can be maintained within allowable thermal limits. The present study details the effect of a few typical turbulator geometries in a high aspect ratio channel. Several studies exist in open literature which discuss the heat transfer enhancement obtained from turbulators such as ribs and dimples with various geometries.

A few investigations on heat transfer in turbulated channels are discussed. Heat transfer in a channel from concave dimples and tear-drop shaped dimples (concavities) was studied by Chyu et al. [76]. Tear drop shaped dimples gave slightly higher heat transfer than concave dimples with both dimple geometries giving much lower pressure drop as compared to rib turbulators. Effect of channel height on heat transfer and friction was studied by Moon et al. [77]. A heat transfer enhancement of about 2.1 times that of a smooth channel was observed for the dimple geometry tested. Mahmood et al. [78] studied the flow structure and the local heat transfer on a dimpled surface in a channel. Vortex pairs originating from flow within the dimples were found to augment heat transfer especially near the downstream rims of each dimple. Nine concave and cylindrical dimples with various diameters and depths were studied by Moon and Lau [79] for several Reynolds numbers in a square channel. Cylindrical dimples were found to give a higher heat transfer coefficient and a lower pressure drop than concave dimples with same diameter and depth. Effect of aspect ratio, temperature ratio and Reynolds number on heat transfer in a dimpled channel was investigated by Mahmood and Ligrani [80]. Effect of dimple depth was investigated by Burgess et al. [81]. Deeper dimples were found to give higher heat transfer due to an increase in the strength of the vortical flow structures emerging from the dimples. Heat transfer in a channel with ribbed walls has been investigated by several researchers and a few relevant studies are listed. Han [82] correlated available data for angled rib turbulators based on the roughness function. V-shaped and v-shaped broken ribs were studied by Han et al. [83] and Han and Zhang [84]. The broken ribs were found to give higher heat transfer coefficients as compared to similar continuous ribs.

Internal heat transfer measurements were performed in the present study in a high aspect ratio channel with turbulators on one of the wider walls. This simulates the typical design in a combustor liner where only the liner wall is exposed to high heat fluxes originating from the combustor gases. Five different turbulator geometries are tested including 3 types of dimple arrays and 2 types of ribbed arrays. The enhancement obtained from these geometries is compared against a smooth liner wall. Tests are carried out for very large Reynolds numbers upto 1.5 million to maximize heat removal from the hot liner wall. Most experimental data available in literature extends only up to Reynolds numbers of ~100,000 for turbulated channels. Inadequate information pertaining to heat transfer enhancement from these turbulators is available at such high Reynolds numbers. Thus, the primary motivation of this study is to investigate the heat transfer and flow characteristics of typical turbulators at very high flow conditions. Measurements for heat transfer are made at steady state conditions using thermocouples to record temperature data.

4.2. EXPERIMENTAL FACILITY

Tests were performed in a rectangular channel with an aspect ratio of 6. The width of the channel was 50 cm with a height of 8.3cm. Three walls of the channel were heated including one wide wall or the test wall and the two narrow side walls. This design models the combustor liner where the test wall acts as the interface between the hot combustion gases and the gas turbine outer casing. This interface or liner wall is cooled from the outside to prevent it from over-heating. The heated area of the channel was 152.4cm long. In addition to this length, an entrance and exit short channel with a length of 30.2cm was provided to ensure that the flow entering and exiting the heated portion of the channel is not disturbed due to the effects of

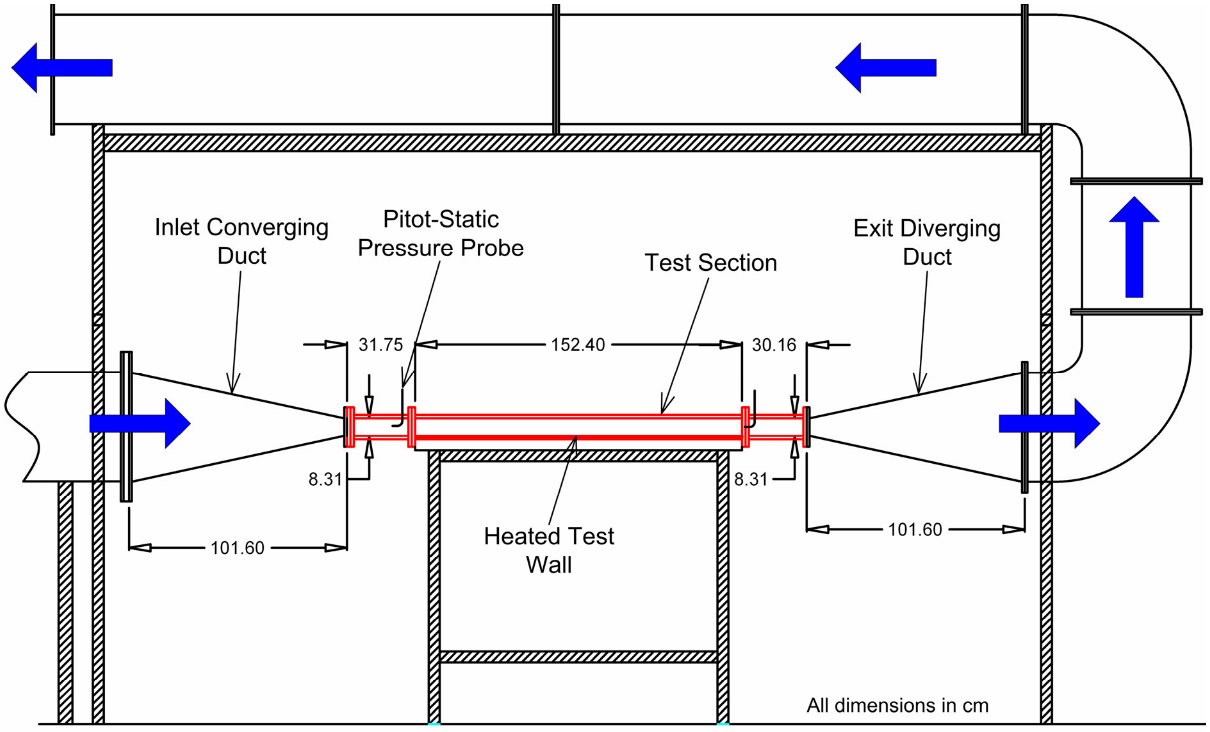

Fig. 4.1 Layout for high flow channel

sudden contraction and expansion respectively. A smooth, converging duct guides the flow to the channel entrance from a 50.8cm diameter pipe to prevent the formation of a vena contracta downstream of the test section entrance. A smooth diverging duct is also placed at the channel exit to prevent the exiting flow from affecting the upstream fully-developed channel flow at compressible, high Mach number flow conditions. Figure 4.1 shows the layout of the test facility. The inlet and exit converging ducts were made from 0.32cm thick steel sheet metal. The channel walls were made from aluminum and were 1.59cm thick. Aluminum was chosen as it has a relatively high thermal conductivity of 177 W/mK ensuring almost uniform wall temperatures.

Tests were performed for heat transfer and pressure losses for flow in a smooth channel initially to compare against existing empirical correlations. Five different geometries were tested on the test wall and compared against data for a smooth channel. The five geometries tested include 2 cases with spherical dimples, one case with cylindrical dimples and two cases with discrete, angled ribs. Figure 4.2 shows all the three dimple geometries tested. For the first case (case 1), a staggered array of spherical dimples with a sphere diameter of 3.39cm, depth of

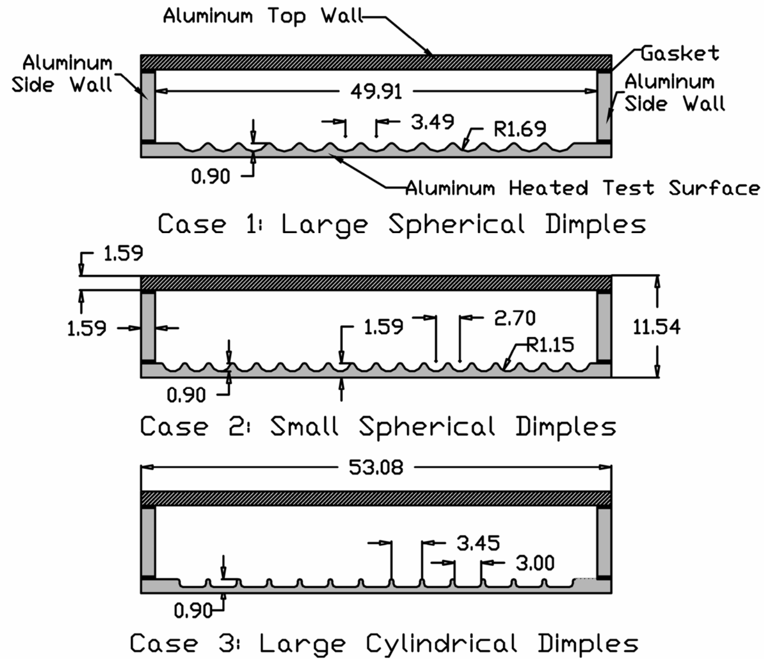

Fig. 4.2 Dimple configurations for Cases 1 to 3

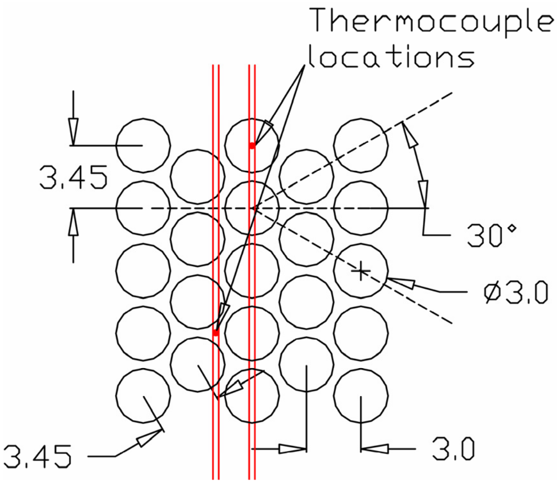

Fig. 4.3 Dimple detail for case 1

0.9cm and spacing of 3.45cm was used. The diameter of the circle formed by the dimple imprint on the test wall was 3cm. Figure 4.3 shows the detailed layout of the dimples on the test wall. A total of 650 dimples were machined on the test wall. To get maximum dimple density on the test wall, the dimples were arranged in staggered fashion in the streamwise direction. Thus, a dimple in an adjacent, downstream row was arranged such that its center lay on the vertices of an equilateral triangle with a length of 3.45cm (for case 1) formed by it and two dimples in the previous row. In case 2, smaller spherical dimples were used with a spherical diameter of 2.31cm, depth of 0.9cm and spacing of 2.7cm was used. A total of 1104 dimples were machined on the test wall. In case 3, cylindrical dimples with the same size, depth and spacing as case 1 were used. Edge circle diameter for the cylindrical dimples was 3cm with a depth of 0.9cm and a spacing of 3.45cm. A fillet radius of 2.1mm was provided on the dimple imprint edge for all dimpled cases to account for the edge defects frequently encountered while casting the combustor liner walls. The layout of the dimples on the test wall is shown in Fig. 4.4

Figure 4.4 also shows the ribbed geometry pattern tested on the test wall (case 4). The test wall is divided into six rows of ribs placed in the streamwise direction. Each discrete rib in each streamwise row was placed at an angle of 45^o and had a length of 11.76cm with a rib height to channel height ratio (e/H) of 0.11. The rib pitch to rib height ratio (p/e) was 10. Discrete ribs made from brass were provided only on the test wall while the side walls were maintained smooth similar to the dimpled cases. The ribs can be subjected to a large form drag at very high Reynolds numbers and hence were glued on the test wall using a strong adhesive epoxy (JB Weld). The ribs in adjacent streamwise rows were staggered with respect to each other. The ribs were arranged in a V-shaped discrete rib pattern for the center two streamwise rows and the adjacent rows were then arranged in a parallel discrete rib pattern resulting in a \\\V// arrangement.

The mainstream air for the channel was supplied by a three stage centrifugal compressor connected to a 450hp electric motor. The compressor is rated for a maximum pressure differential of 55kPa and a volume flow rate of $6.2m^3/s$. The pressure and volume flow rate in the channel could be varied by a frequency controller operating between 0 to 60Hz. The total flow rate in the channel was controlled to correspond to pre-determined Reynolds numbers based on the channel hydraulic diameter. The Reynolds number was calculated using the following equation.

$$\mathrm{Re} = \frac{\rho \overline{V}_{in} D_h}{\mu} \qquad (4.1)$$

Heat transfer and pressure loss experiments were performed for six nominal Reynolds numbers of 100,000, 200,000, 500,000, 900,000, 1,100,000 and 1,300,000. The maximum flow rate in the channel depended on the overall pressure drop over the test section. Hence, tests for the highest Reynolds number of 1.3 million could not be performed for turbulators geometries

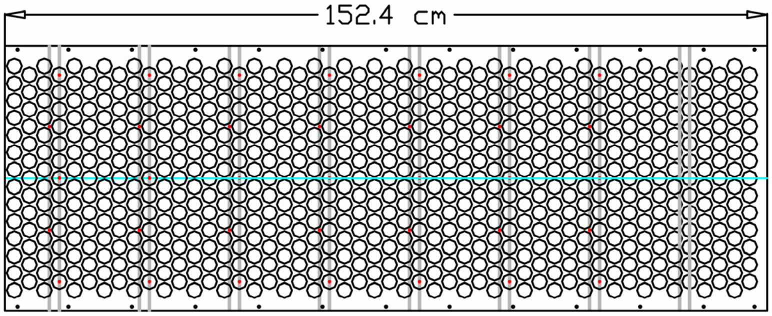

Case 1: Large Spherical Dimples

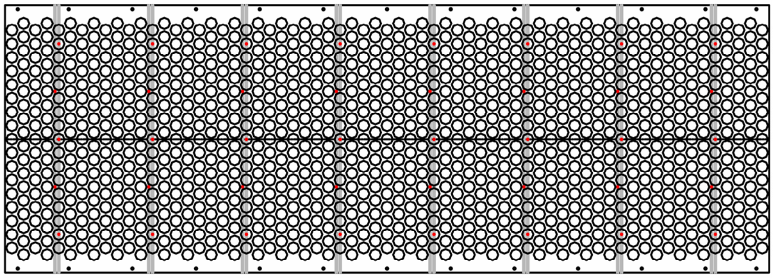

Case 2: Small Spherical Dimples

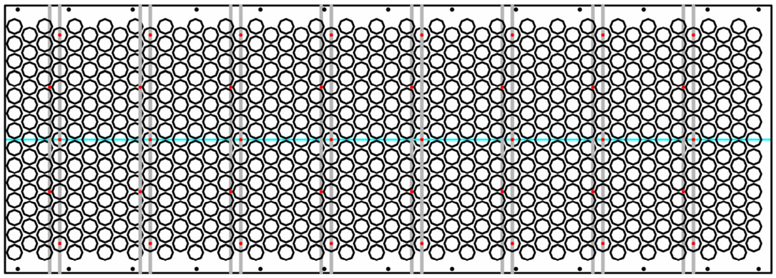

Case 3: Large Cylindrical Dimples

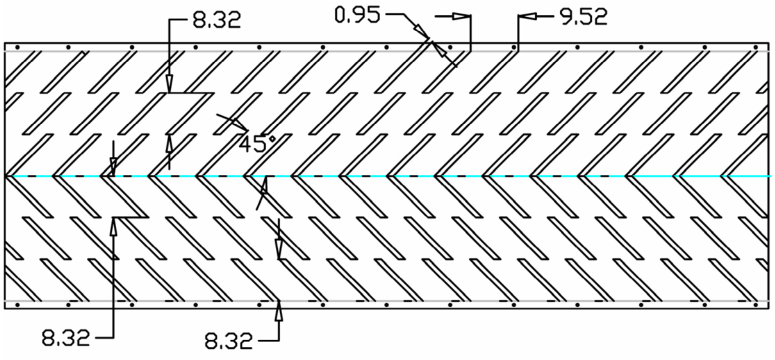

Case 4: \\V// Discrete Rib Arrangement

Fig. 4.4 Turbulator layout on test wall for cases 1 to 4

such as ribs which cause high frictional losses. The average inlet flow velocity was determined by traversing a pitot-static tube through a 5x3 matrix of points, 7.3cm upstream of the heated walls. It was found that the average inlet velocity was equivalent to 0.96 times the centerline velocity at the channel inlet. Flow profile at the exit of the heated test section was also measured using a pitot static tube traversed through the same 5x3 matrix of points, 2.22cm downstream of the heated test section. The inlet flow Mach numbers for Reynolds numbers of 900,000, 1,100,000 and 1,300,000 were greater than 0.2 resulting in a compressible flow regime. The highest Mach number at Re = 1.3 million was around 0.5.

4.3. MEASUREMENT THEORY

A steady state heat transfer measurement technique was used to determine the heat transfer. As the heat transfer coefficient on a turbulated wall at these high Reynolds numbers is very high, two high heat flux heaters were used to supply heat to the test wall while one heater was used to heat each smooth, side wall. Three phase flexible wire heaters, connected to 408V, 50A three phase supply line via individual auto-transformers, were used to generate the required heat to raise the wall temperature. The heaters used generate uniform heat flux over their entire area resulting in a uniform wall heat flux boundary condition on the walls. The total heat input for a rib turbulated test wall at the highest flow Reynolds number was around 7kW. During testing, it was ensured that the heat supplied from both heaters on the test wall was identical. The heat supplied was obtained by measuring the phase voltage, $V_{ph,i}$ and phase current, $I_{ph,i}$ for each phase using multimeters. The input heat flux, q''_{heater} supplied by a single three phase heater is given by

$$q''_{heater} = \sum_{i=1}^{3} V_{ph,i} I_{ph,i} \Big/ A_{heater} \tag{4.2}$$

The heaters were stuck on the outer surface of the channel walls using a high temperature adhesive. All four channel walls were covered with fiber-glass insulation 4cm thick to minimize extraneous heat loss. Data is corrected for this heat lost due to conduction and radiation to the surroundings. The amount of heat lost, q_{loss} was calculated by supplying heat to the channel walls under no-flow conditions with the same temperature difference maintained between the channel walls and ambient as in the actual tests. The heat loss which is a function of this temperature difference was determined for a range of temperatures and the resulting heat loss data was curve fitted and incorporated in the heat transfer calculation program. As the test wall and side walls are made from a single piece of aluminum which has relatively high thermal conductivity, during testing, heat conduction may occur within each wall. Nevertheless, temperature gradients were found to exist within the test wall and side walls and the temperatures obtained from the thermocouples at each streamwise location represent the locally averaged wall temperatures in that particular region. One-dimensional heat conduction along the streamwise direction within the test wall was corrected by applying a correction to the input heat flux. A finite difference model was applied to calculate the heat flux between two streamwise thermocouple locations which act as nodes. The smooth test wall and the ribbed test walls gave higher heat conduction corrections than the dimpled walls as the cross-sectional area for heat conduction is larger for the smooth and ribbed walls. Thus, the total heat flux supplied to air was given by

$$q'' = q''_{heater} - \left(q''_{loss} + q''_{cond}\right) = q''_{heater} - \frac{1}{A_{s,i}}\left[q_{loss,i} + k_{Al}A_c\left(\frac{T_{i-1}-T_i}{\Delta x_i} - \frac{T_i - T_{i+1}}{\Delta x_{i+1}}\right)\right] \tag{4.3}$$

where q''_{heater} is the power output per unit area from the heaters as obtained from voltage-current measurement, q''_{loss} is the net heat flux lost external to the test surface and q''_{cond} is the heat lost through conduction between regions. The heat transfer coefficient h, dictated by Newton's Law for convective heat transfer is given by

$$h_i = \frac{q''}{T_{w,i} - T_{\infty,i}} = \frac{q''}{T_{w,i} - \left(T_{aw,i} + \Delta T_{corr,i}\right)} \tag{4.4}$$

where q'' is the net convective heat flux from the surface after accounting for the heat loss through the insulation and through conduction in the test wall.

Wall temperature in the test wall and the side walls was measured using T-type thermocouples embedded into the walls at eight streamwise locations placed 18.7cm apart. For the smooth and ribbed channels, the test wall was instrumented with thermocouples placed at seven equally spaced streamwise locations against 8 locations for the dimpled test wall. Each streamwise location was fitted with 5 thermocouples on the test wall and 3 thermocouples on one of the side walls. For the three dimpled test walls, the 5 thermocouples were located such that two thermocouples were at the base of the dimples whereas the other three were located just below the rim formed between adjacent dimples (Fig. 4.3). Only one side wall was instrumented with thermocouples as the heat transfer coefficients for both narrow side walls was assumed to be symmetric and same. However, both the side walls were heated to ensure symmetric thermal boundary layer development in the channel. The thermocouples were placed in tiny holes drilled from the outer surface of the channel walls and spanwise grooves were cut into the walls to allow passage for the thermocouples wires. The thermocouples were connected to a Fluke data logger to record temperatures. The four walls of the channel were isolated from each other to prevent heat conduction errors by placing a 1.6mm rubber gasket between their contact interfaces.

Steady state was obtained within 90 minutes after applying heat to the test section. The amount of heat applied was controlled such that the steady-state wall temperature T_w was maintained around 20^{o}C higher than the inlet air temperature. High wall temperatures result in larger heat losses whereas low wall temperatures result in higher uncertainty in the data as the sensitivity of the heat transfer coefficient given in Eq. (4.4) at low temperature difference increases. A 20^{o}C temperature difference ensured an optimum balance with low relative uncertainties as well as low heat losses. The adiabatic wall temperature, T_{aw} in Eq. (4.4) was measured for an unheated surface but under the same flow conditions as the actual test. The adiabatic wall temperature was thus measured prior to the application of heat to the channel walls. The adiabatic wall temperature is equivalent to the recovery temperature of air flowing in the channel. Thus, it includes the effect of viscous heating due to eddy dissipation at high Mach numbers. However, this temperature does not include the effect of bulk air temperature rise from wall heating during the heat transfer experiment. For this reason, the adiabatic wall temperature is corrected by adding a correction factor ΔT_{corr} to account for the increase in bulk air temperature along the length of the channel. Assuming the inlet fluid temperatures for both tests to be the same, the corrected average fluid temperature can then be given as

$$T_{\infty,i} = T_{aw,i} + \Delta T_{corr,i} = T_{aw,i} + \left(\frac{T_{b,i+1} - T_{b,i}}{2} \right) \tag{4.5}$$

Inlet and exit bulk flow temperatures T_b were measured using T-type thermocouples suspended along the channel centerline. The heat transfer coefficient was expressed in terms of the Nusselt number Nu and was calculated using Eq. (4.6)

$$Nu = \frac{hD_h}{k_{air}} \tag{4.6}$$

The Nusselt number obtained from experiments was compared with an empirical correlation for fully developed, turbulent flow in a smooth channel given by Dittus-Boelter (Kays and Crawford [75])

$$Nu_0 = 0.023 Re^{0.8} Pr^{0.4} \tag{4.7}$$

To account for variation in the thermo-physical properties of air along the length of the channel, Nu_0 was corrected by multiplying it with a factor of $(T_{b,i}/T_{w,i})^{-0.55}$. All the thermophysical properties were evaluated at the mean film temperature ($(T_w + T_b)/2$). It should be noted that the above empirical correlation (Eq. (4.7)) is valid for a fully developed thermal boundary layer when all walls of the channel are heated. In the present study, only three walls of a four-sided channel were heated.

Streamwise static pressure measurements along the channel length were performed though pressure taps at 8 streamwise locations corresponding to the same locations as the thermocouples on one side wall. Pressure taps were drilled along the centerline on one narrow side wall and the unheated wide wall. The pressure taps were connected to a calibrated pressure transducer to record the static pressures. The friction factor based on the overall pressure drop in the channel and the average flow exit velocity was expressed by Eq. (4.8). The friction factors were compared with those for a smooth channel with fully developed flow obtained from Petukhov's correlation given in Eq. (4.9) (Kays and Crawford [75])

$$f = \frac{(\Delta p/\Delta x) D_h}{\rho \overline{V}_{exit}^{\,2}/2} \tag{4.8}$$

$$f_0 = [0.79 \ln(Re) - 1.64]^{-2} \tag{4.9}$$

Local heat transfer measurements were done for Case 1 using the steady state, hue-detection based liquid crystal technique. Wide band (20°C) liquid crystal paint was used with a color change (red) start temperature of 45°C (R45C20W). This liquid crystal paint was sprayed on a stainless steel plate machined with dimples with a length of about 1.07 times the channel hydraulic diameter. A layer of non-reflective black paint was sprayed on the stainless steel plate prior to painting with the liquid crystal paint to provide good color contrast. This stainless steel plate was located at a distance of $7.3D_h$ from the inlet of the channel. The thermal conductivity of stainless steel is similar to the metal used to cast the combustor liner wall. Thus, the wall temperatures measured from the liquid crystal technique correspond to a conjugate heat transfer problem similar to actual combustor liner conditions as heat conduction will occur within the liner wall. To accommodate this plate in the test section, the dimpled aluminum test wall was cut to fit this plate in the channel. The stainless steel plate was isolated from the adjacent aluminum test walls using a 3.2mm thick rubber gasket. The same heater and data reduction was used to

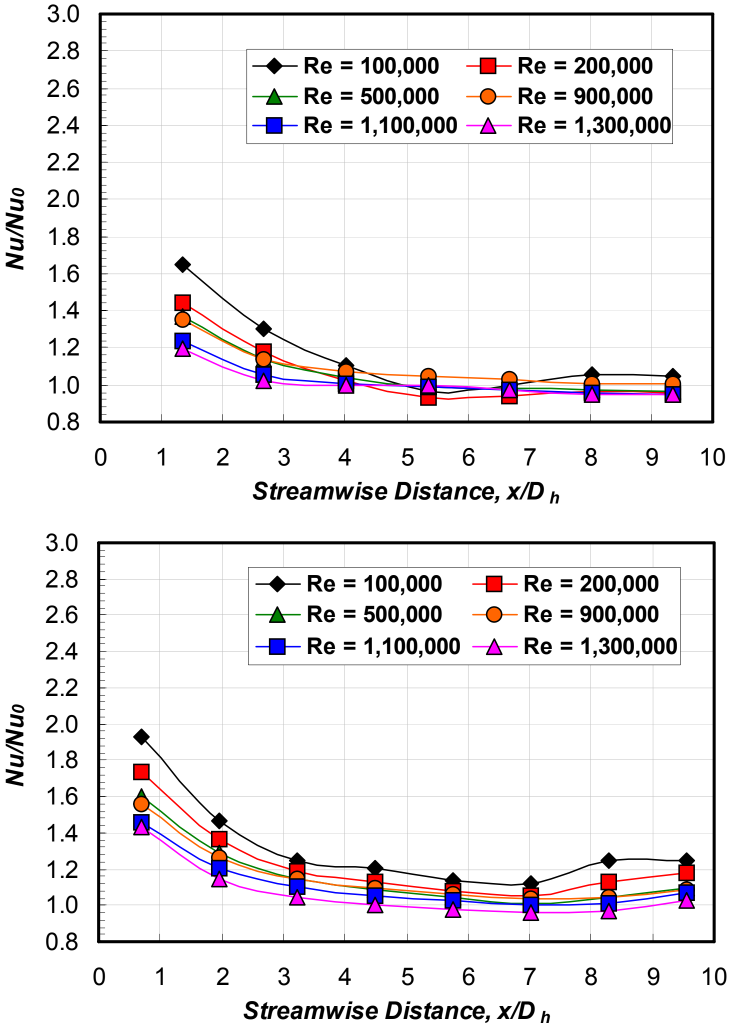

Fig. 4.5 Streamwise heat transfer distribution for smooth channel (reference case)

calculate the heat transfer coefficient. The wall temperature from thermocouples in Eq. (4.4) was replaced with the local wall temperature measured by the liquid crystal paint. The liquid crystal paint was calibrated for hue and temperature under the same optical conditions. The opposite wide wall of the channel was replaced with a plexiglass wide wall to allow optical access to the coated surface.

Uncertainty calculations were performed based on a confidence level of 95% and were based on the uncertainty analysis method of Coleman and Steele [41]. Lower Reynolds numbers gave higher uncertainties in the heat transfer coefficients due to lower magnitudes. Highest relative uncertainties for Nu were around 11% for Re = 100,000. Relative uncertainties in flow measurement and friction factor measurement were around 6% and 7.5% respectively.

4.4. RESULTS AND DISCUSSION

4.4.1. Heat Transfer for Reference Case – Smooth Channel

Experiments were initially performed for a smooth channel to calibrate the test section. Tests were performed for the specified range of Reynolds numbers. Results for heat transfer against streamwise distance are presented in Fig. 4.5 for all Reynolds number for the wide as well as narrow walls. It should be noted that fully developed turbulent flow occurs in a smooth channel after about x/D_h = 20. Thus, the flow at the exit of the smooth channel may not be fully developed at x_{max}/D_h = 9.4 resulting in heat transfer enhancements greater than 1. The heat transfer is highest near the entrance of the channel due to a smaller boundary layer thickness as progressively decreases along the streamwise direction. The decrease in heat transfer is more noticeable for the narrow side wall. Peak Nusselt number for the highest Reynolds number for the first upstream thermocouple location is as high as 2200.

In a high aspect ratio channel, the velocity profile along the shorter side attains a parabolic profile much more quickly than along the longer side. Along the center span of the wider test wall, the flow behavior resembles the flow between parallel plates. For this reason, the heat transfer enhancement on the wider test wall is close to 1 at x/D_h = 7 as the flow is near fully developed with an x/W_{narrow} = 18.3 at the channel exit. The boundary layer for the wide as well as narrow wall develops simultaneously and the thickness should be identical for a particular streamwise location. However, the velocity profile along the longer side does not attain a fully developed parabolic form as x/W_{wide} = 3.05 at the channel exit. Along the narrow wall, corner vortices at the edges may cause a greater impact on its average heat transfer coefficient resulting in slightly higher heat transfer. It should be also noted that one wall adjoining the narrow side wall is heater whereas the other wide wall is not. As a result, the thermal boundary layer profile may be skewed which may also explain the high heat transfer coefficients. Also, this results in large heat losses to the adjoining unheated wall at steady state due to a large contact area (20% of surface area for each wall interface) even though a 1.6mm rubber gasket is provided between them. Heat loss from the narrow side wall at low Re is as high as 35% of the heat input to it.

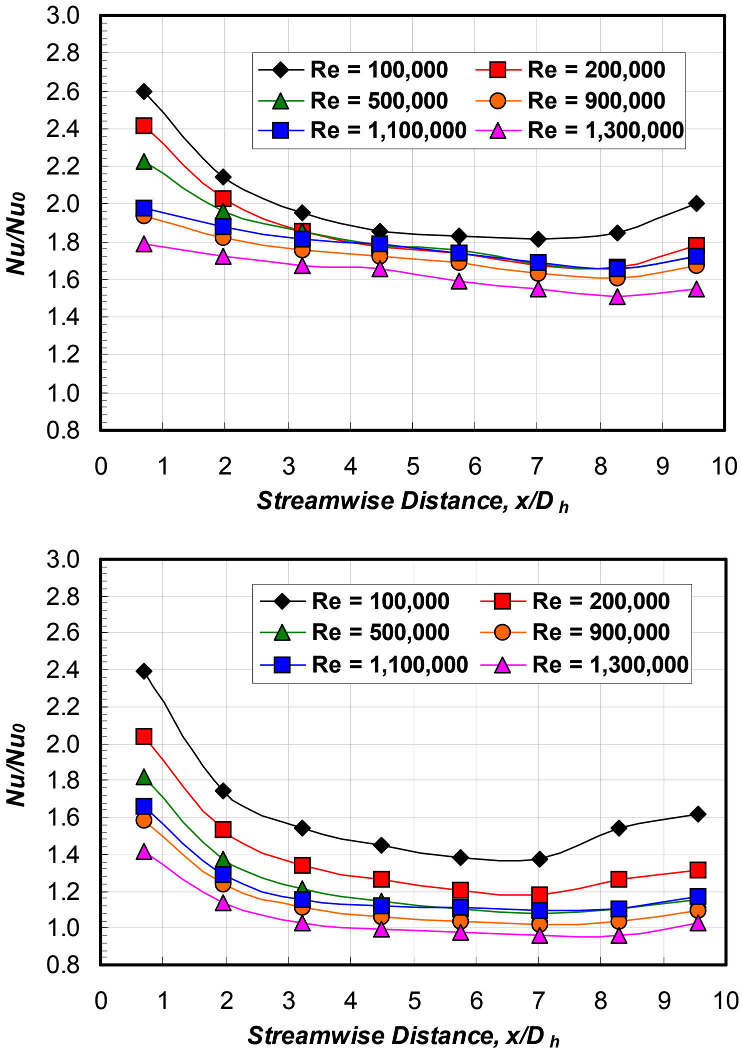

Fig. 4.6 Streamwise heat transfer distribution for spherical dimpled channel (case 1)

The effect of corner vortices and skewed thermal boundary layer may explain heat transfer enhancements from the side wall. As the Reynolds number increases, the enhancement at x/D_h = 7 approaches 1.

4.4.2. Heat Transfer for Turbulated Channels – Cases 1 to 4

Streamwise distributions for cases 1 to 4 are shown in Figs. 4.6, 4.7, 4.8, and 4.9 respectively for both the test wall and the side wall. Heat transfer distributions for the test wall are high near the channel entrance and decrease downstream similar to the smooth channel.

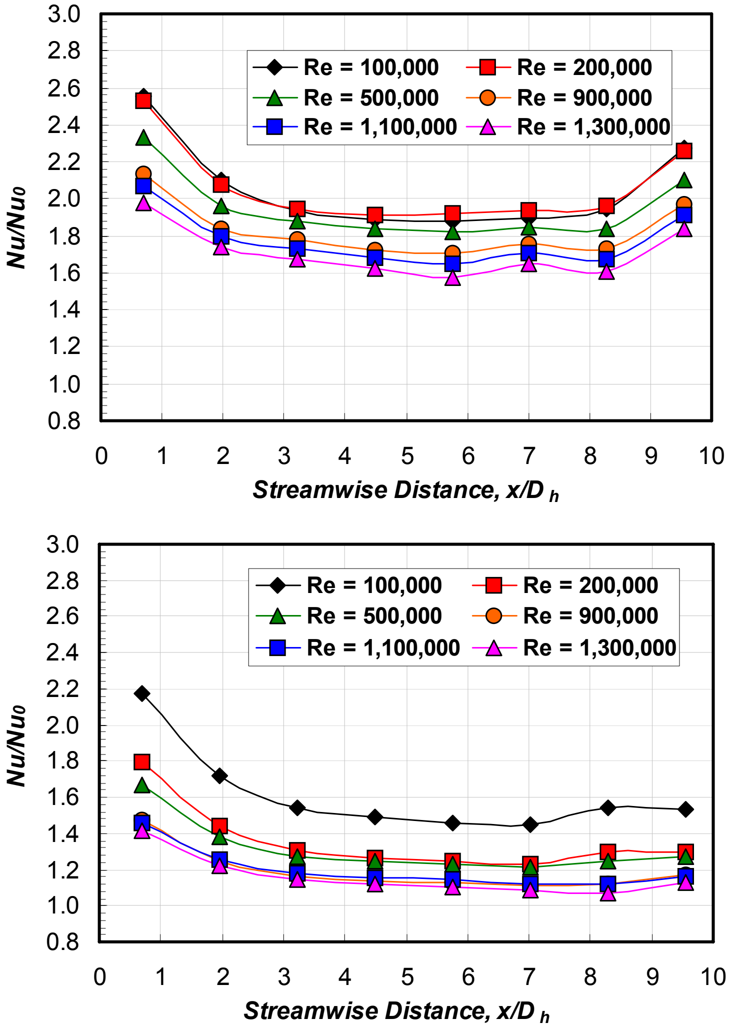

Fig. 4.7 Streamwise heat transfer distribution for small dimpled channel (case 2)

However, due to the added turbulence from the turbulators, this decrease is less dramatic. In general, lowest Nusselt numbers are observed for about x/D_h = 8. The Nusselt number streamwise trends on all dimpled test walls are similar. Cases 1 and 3 show similar heat transfer magnitudes. Both these cases have similar dimple dimensions and spacing with case 1 having spherical dimples and case 3 having cylindrical dimples. Thus, the heat transfer distribution is insensitive to dimple shape. Case 2 with smaller spherical dimples shows slightly higher heat transfer than cases 1 and 3. A higher dimple density on the test wall may result in higher turbulence from secondary flows which may explain the slightly higher heat transfer magnitudes. Heat transfer for the \\\V// ribbed channel (Case 4 in Fig. 4.9) is higher and more uniform than

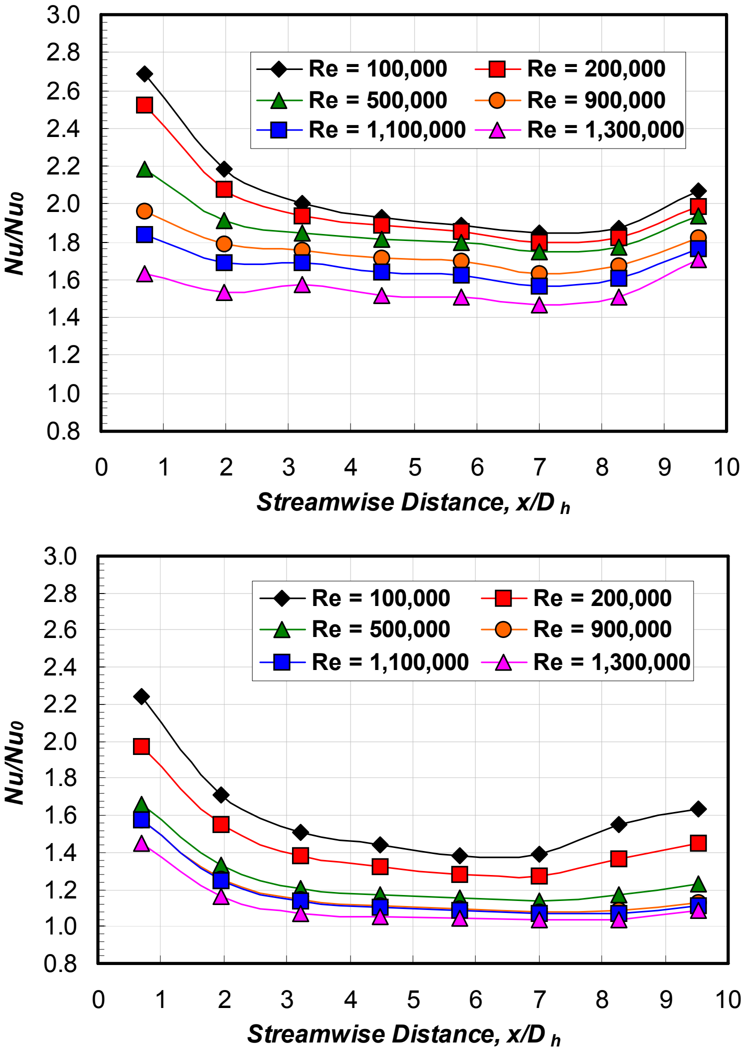

Fig. 4.8 Streamwise heat transfer distribution for cylindrical dimpled channel (case 3)

that for the dimpled channel cases. Stronger reattachment and secondary flows setup due to the angled ribs may cause the flow to become periodic earlier than the dimpled channels. Flow reattachment and secondary flows inside the dimples is typically milder than ribs and has been visualized by Mahmood et al. [78].

Heat transfer on the side walls is also depicted in Figs. 4.6, 4.7, 4.8, and 4.9 for cases 1 to 4 respectively. Heat transfer enhancement for x/D_h = 8 is as high as 1.4 times for the cases with dimples and 1.5 times for the ribbed cases for Re = 100,000. However, it should be noted that the enhancement over the smooth channel data in Fig. 4.5 is much less due to higher Nusselt numbers for the smooth side wall at low Re than those observed from fully developed turbulent

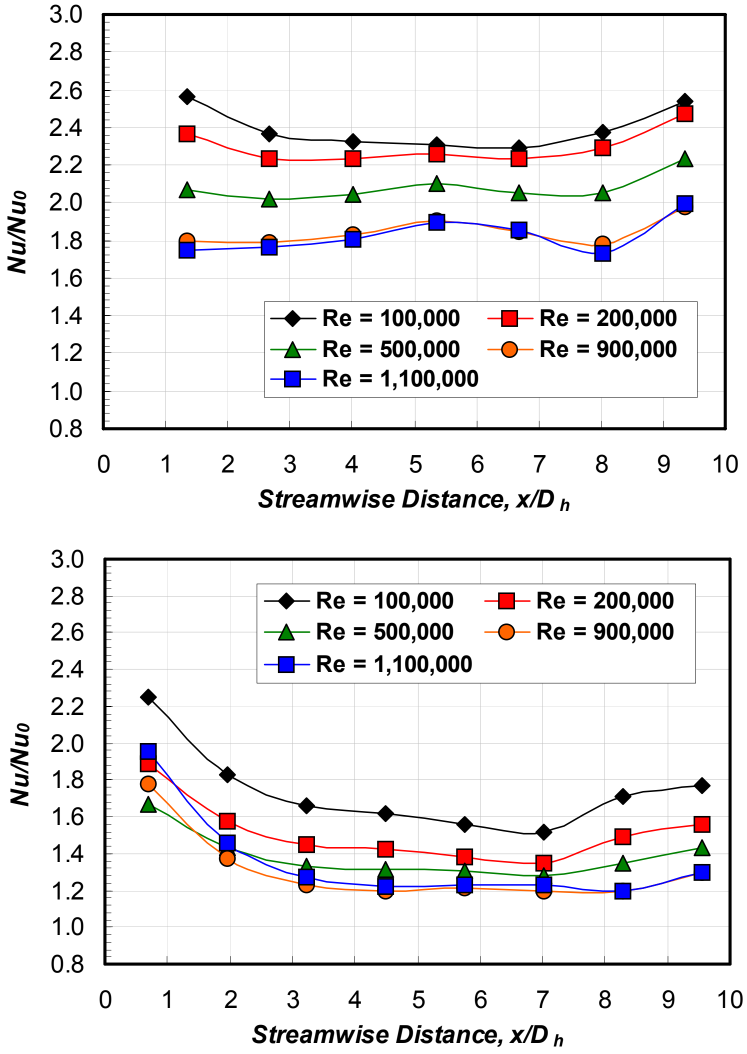

Fig. 4.9 Streamwise heat transfer distribution for channel with \\V// ribs (case 4)

flow correlations. If normalized with the smooth channel data in Fig. 4.5, maximum enhancement for the side wall for Re = 100,000 is around 1.25 for the dimpled cases and around 1.35 for the ribbed case. At high Reynolds numbers, the enhancement decreases. Enhancement levels drop down to ~1 for the highest Reynolds numbers for the dimpled cases while enhancement levels close to 1.2 still persist for the ribbed channel. The overall increase in turbulence in the channel due to the presence of turbulators may contribute to the increase in heat transfer on the side wall. Heat transfer for the last thermocouple location at $x/D_h = 9.5$ shows higher heat transfer than the previous locations for all cases for both the test and the side walls.

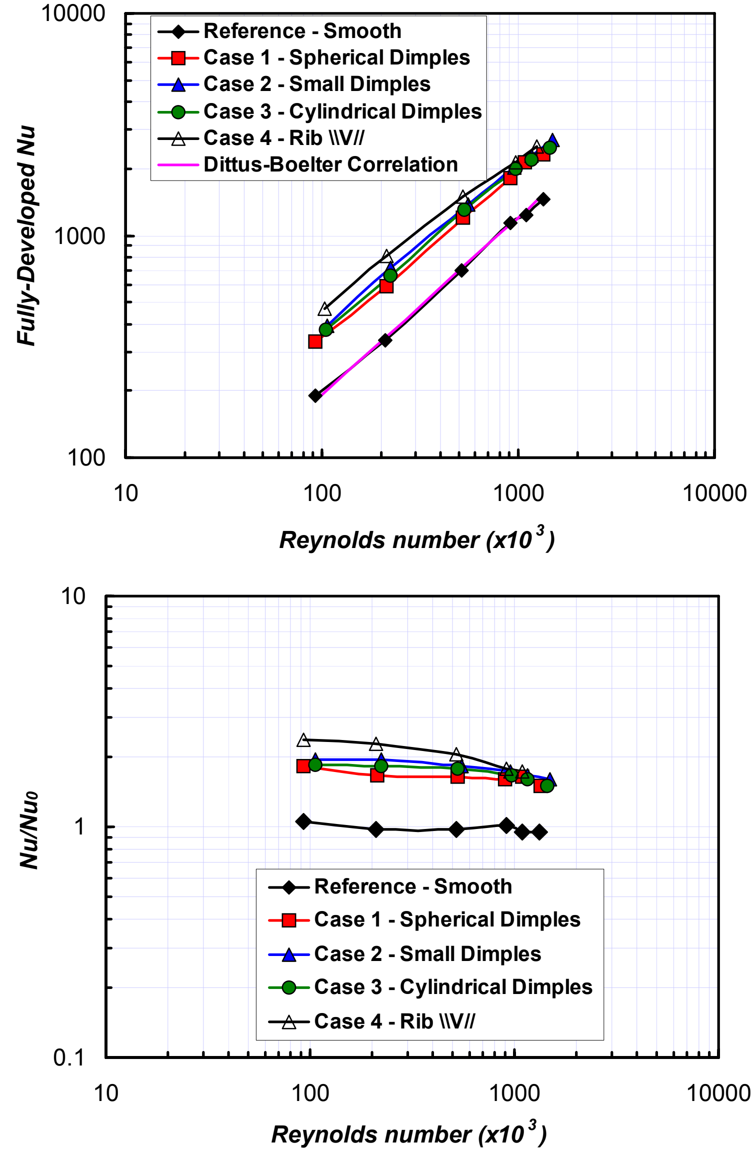

Fig. 4.10 Comparison of fully developed heat transfer and enhancement for all cases for the test wall

This unusual behavior is probably due to larger uncertainty from heat conduction to the downstream unheated flow guides.

Figures 4.10 and 4.11 show the fully developed Nusselt number and its enhancement for test and side walls respectively. For the test wall, the streamwise location $x/D_h \sim 8$ is considered as the fully developed flow region whereas for the side wall, $x/D_h \sim 7$ is considered as the fully developed flow region. The figures compare the heat transfer among all cases. At high

Reynolds numbers, the Nusselt number trends for all turbulated cases appear to converge with each other. From Fig. 4.10, it can be discerned that ribbed channel provides higher heat transfer than dimpled channels. The heat transfer enhancement for the ribbed channel decreases from about 2.4 for Re = 103,000 to 1.7 for Re = 1,240,000. The dimpled channels (cases 1 – 3) show similar heat transfer. Heat transfer for case 2 with smaller dimples is slightly higher than cases 1 and 3 as observed earlier. For Case 2, the heat transfer enhancement drop is lower than the ribbed channel with increasing Re and decreases from 1.9 for Re = 106,000 to 1.6 for Re = 1,490,000. Case 1 with large spherical dimples appears to give the lowest heat transfer enhancement among all turbulated geometries tested.

Similar observations can be made for heat transfer on the side wall shown in Fig. 4.11. However, the Nusselt number magnitudes are much lower. Higher heat transfer for the smooth channel as compared to the Dittus-Boelter correlation (Eq. 4.7) for low Reynolds numbers can be clearly observed from this plot. The heat transfer enhancement decreases with increasing Reynolds numbers similar to the test wall results. For the ribbed channel, heat transfer enhancement decreases from 1.5 for Re = 103,000 to 1.22 for Re = 1,240,000. Nusselt number enhancement for the dimpled channel cases approaches unity with higher Reynolds numbers.

4.4.3. Friction Factor Comparison

Figure 4.12 compares the friction factors and its enhancement as compared to a correlation for a smooth channel (Eq. (4.9)) for all cases. The friction factor is based on the pressure drop measured from $x/D_h = 3.35$ to $x/D_h = 9.6$. Friction factors for the smooth channel are quite low with values decreasing from 0.014 to 0.012 with increasing Reynolds numbers. The measured friction factors are very close to the calculated friction factors from Eq. (4.9) with enhancement magnitudes close to unity for all Re. As with the heat transfer distributions, friction factors for the dimpled channels are similar with magnitudes ranging between 0.03 to 0.06. In general, case 3 with cylindrical dimples shows lowest friction factors among all turbulated cases. Highest friction factors are observed for the ribbed channel with an average magnitude of about 0.1 and an enhancement of around 8. In general, friction factors for the ribbed channel are about 80 to 100% than the dimpled channels. A minor increasing trend is observed with increasing Reynolds numbers for all turbulated cases.

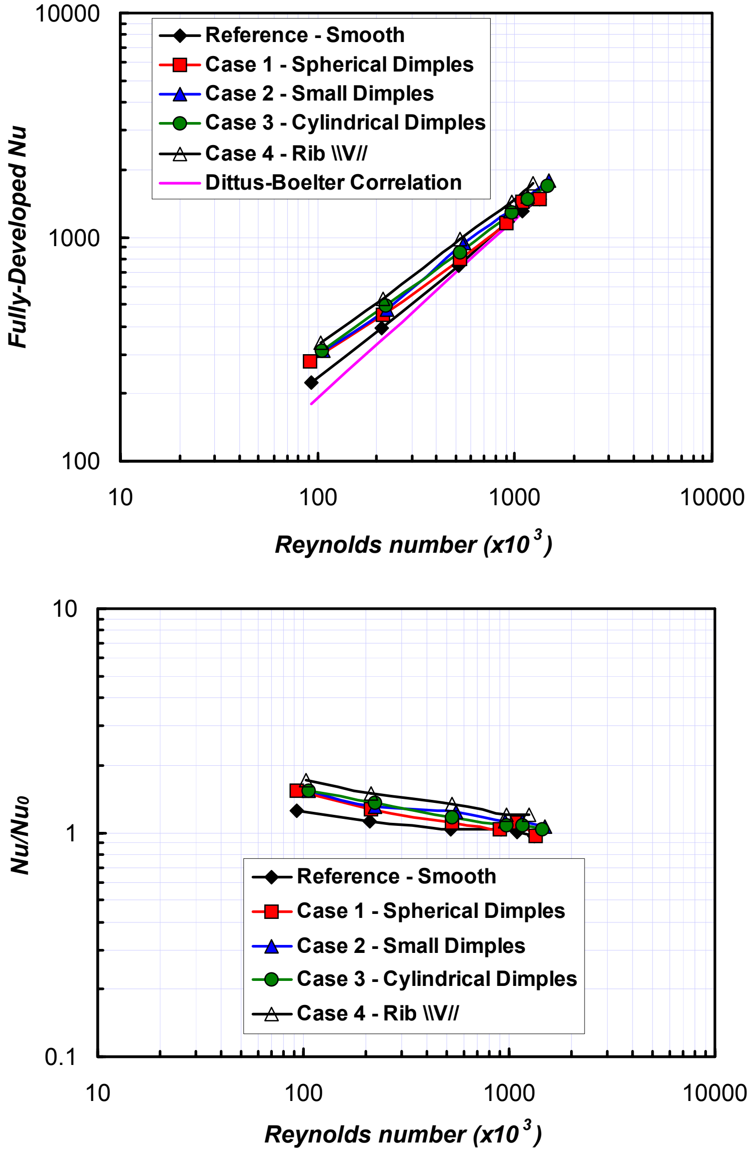

Fig. 4.11 Comparison of fully developed heat transfer and enhancement for all cases for the side wall

4.4.4. Local Heat Transfer Distribution

Local heat transfer measurements using liquid crystals were performed near the fully developed region for case 1 for three Reynolds numbers. The heat transfer distributions are depicted in Fig. 4.13. Heat transfer levels on the dimple rims are much higher than those inside

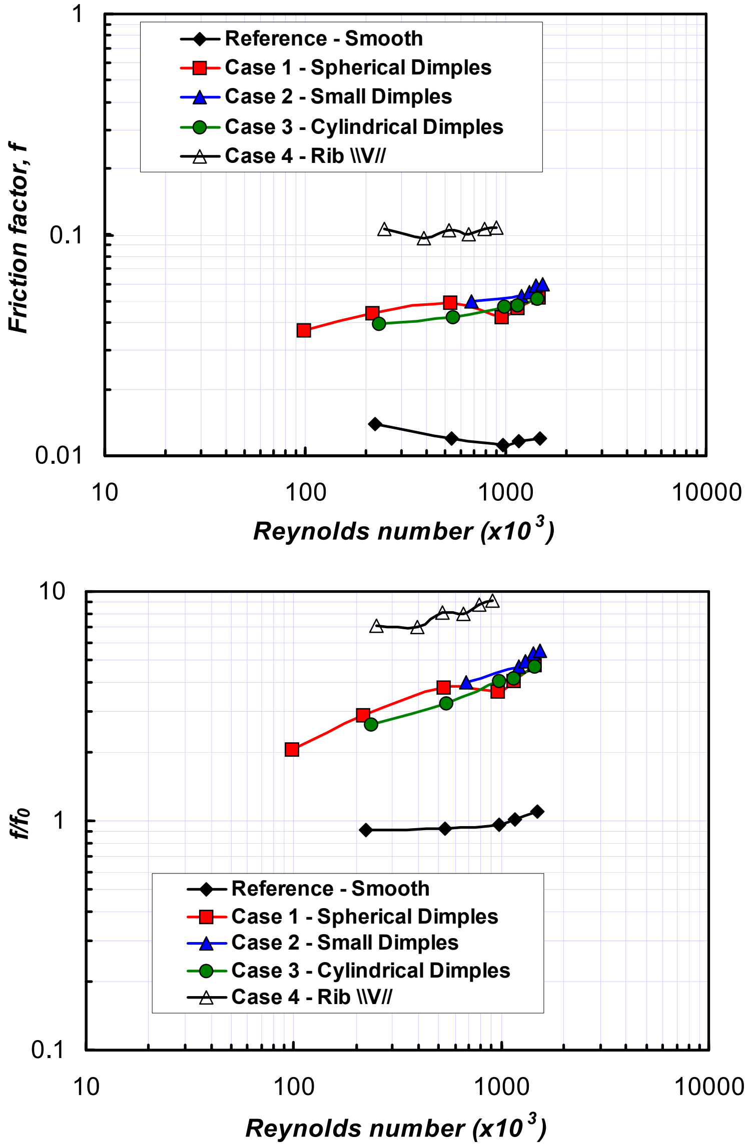

Fig. 4.12 Comparison of friction factor and its enhancement for all cases

the dimple cavity. The secondary flow vortices upon emerging from the dimple cavity reattach on the rim resulting in higher heat transfer coefficients. High heat transfer on the dimple rims was also observed by Burgess et al. [81]. However, the local heat transfer distribution pattern is different from that observed by Moon et al. [77] and Burgess et al. [81]. The local distribution is symmetric around each dimple in the present study whereas high heat transfer coefficients were observed immediately downstream of the dimples by other researchers. The symmetric distribution may be due to heat conduction as a stainless steel plate was used as the test wall in

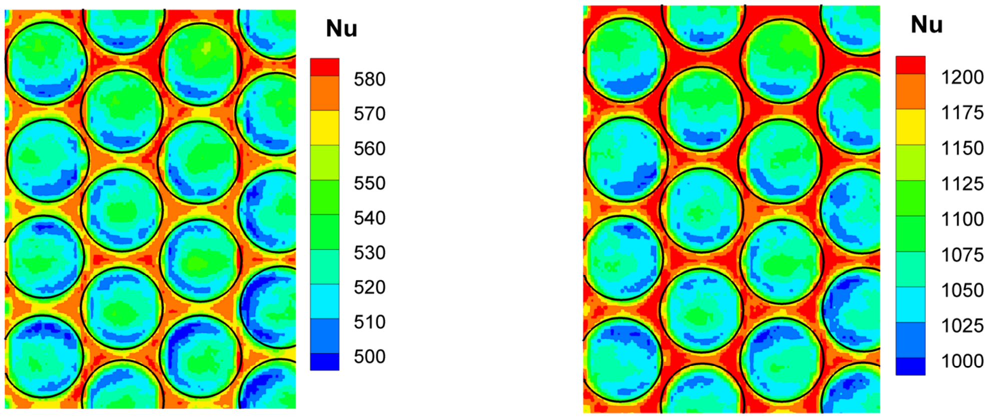

Average Nu = 539
Re = 213,000

Average Nu = 1105
Re = 526,000

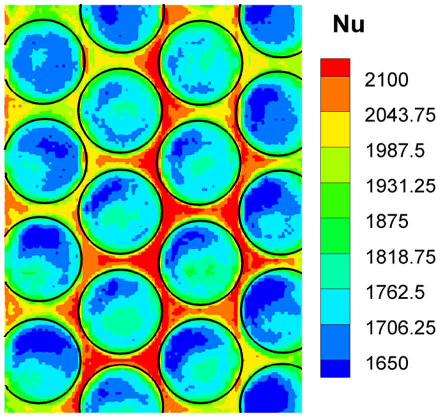

Average Nu = 1828
Re = 905,000

Fig. 4.13 Local heat transfer distribution between x/D_h = 7.3 and 8.4 for Case 1

the present study. Inside the dimple cavity, the base shows slightly higher heat transfer due to mainstream flow reattachment. The average Nusselt numbers obtained from the liquid crystal tests are within 8.5% of the fully developed magnitudes for the corresponding Reynolds numbers observed in Case 1.

4.5. CONCLUSIONS

Experiments were performed to investigate the heat transfer and pressure loss behavior at very high Reynolds numbers. Effect of three dimple shapes and discrete ribs was examined on the heat transfer enhancement and pressure drop. The main conclusions that can be discerned from this study are summarized below.

1. Heat transfer enhancement continually decreases with increasing Reynolds numbers. Enhancement for Re > 1 million is less than 2 times even for the ribbed channel. Average enhancement for the dimpled channels is around 1.6 times at Re = 1.4 million.
2. Best heat transfer enhancement is observed for Case 4 with a ribbed channel. However, highest friction factor is also observed for this case.
3. Heat transfer and friction factors for the dimpled channels (cases 1, 2 and 3) are similar for all three cases. Case 2 with smaller dimples gives slightly higher heat transfer and pressure drop among the three cases studied.
4. Heat transfer enhancement on the smooth side wall increases due to the presence of a turbulated test wall.
5. Local and average heat transfer measurements show good agreement.

5. IMPINGEMENT HEAT TRANSFER FROM JET ARRAYS ON TURBULATED TARGET WALLS

5.1. INTRODUCTION

Impingement heat transfer is frequently used to cool surfaces which are exposed to high temperatures. Jet impingement results in the formation of a thin boundary layer on the target surface thereby increasing the heat transfer coefficients. When a large surface needs to be cooled, a two-dimensional array of jets is frequently used to provide high and uniform heat transfer coefficients over the entire surface. Typical applications include gas turbine vane cooling through impingement inserts and combustor liner cooling. The target walls for both these applications experience very high metal temperatures due to contact with the hot gas on its opposing surface. Typical temperatures in the combustor core exceed 2000^{o}C which is higher than the melting point of most metals. By utilizing advanced cooling concepts such impingement over turbulated surfaces, the target walls can be maintained within allowable thermal limits.

Impingement heat transfer from an array of jets was investigated in the present study under high flow conditions. Heat transfer enhancement on the target wall by addition of artificial roughness as opposed to a smooth target wall is studied. Streamwise riblets, short pins and spherical dimples are used to create artificial roughness and enhance heat transfer. Several studies are available in open literature for jet impingement from arrays on a smooth target wall. Kercher and Tabakoff [85] investigated average surface heat transfer coefficients on a flat surface with a square array of jets impinging on it. The spent air was allowed to interfere with the jets and exhaust through one end of the enclosure. Increasing crossflow was found to decrease heat transfer performance while increasing the number of holes and decreasing hole diameter improved it. Inline and staggered arrays of jets with crossflow were studied by Metzger et al. [86] and Florschuetz et al. [87]. Metzger et al. [86] studied the heat transfer characteristics of two-dimensional arrays of jets impinging on a surface parallel to the jet plate.

The impinging flow was constrained to exit in a single direction formed by the jet plate and the heat transfer surface. The channel height as well as the jet spacing was varied and tested for different mean jet Reynolds numbers ranging from 5,000 to 20,000. The distributions of the stream wise Nusselt number indicated significant periodic variations persisting downstream for at least ten rows of jet holes. A similar study was performed by Florschuetz et al. [87] with ten transverse rows of jets through a plate impinging on a surface parallel to it. The air discharged from the upstream jet rows imposed a crossflow of increasing magnitude on the succeeding downstream jet rows. The streamwise as well as transverse jet spacings and the channel height was varied. Results showed that the periodic variation of the Nusselt number decreased in the downstream direction. Another study [88] using the same apparatus as the two previous studies obtained experimental and theoretical results for streamwise distributions of jet and crossflow velocities as well as Nusselt numbers. Correlations were presented for both inclined and staggered hole patterns including the effects of geometric parameters. Chakroun et al. [89] studied heat transfer from a single round jet, impinging on a surface with small cubic protrusions. The average Nusselt numbers were found to increase from 8 to 28% against a smooth surface. Azad et al. [90, 91] used a transient liquid crystal technique to study impingement heat transfer on a pinned and dimpled surface. In general, at higher Reynolds numbers, pinned surfaces were found to perform better than dimpled surfaces.

The objective of the present study is to determine the impingement heat transfer enhancement from closely spaced jet arrays on turbulated target walls at large Reynolds numbers. Data available in open literature for impingement heat transfer is limited to low Reynolds numbers with peak magnitudes ranging upto 50,000. Also, previous studies have investigated jet array impingement heat transfer for jet to jet spacing only above 5 jet diameters. The present study also investigates advanced cooling concepts such as impingement on turbulated surfaces to maximize heat removal. Measurements for heat transfer are made at steady state conditions using thermocouples to record temperature data.

5.2. EXPERIMENTAL FACILITY

Impingement heat transfer from an array of jets on a smooth and turbulated target wall was determined. The mainstream air for the test section was supplied by a three stage centrifugal compressor connected to a 450HP electric motor. The compressor is rated for a maximum

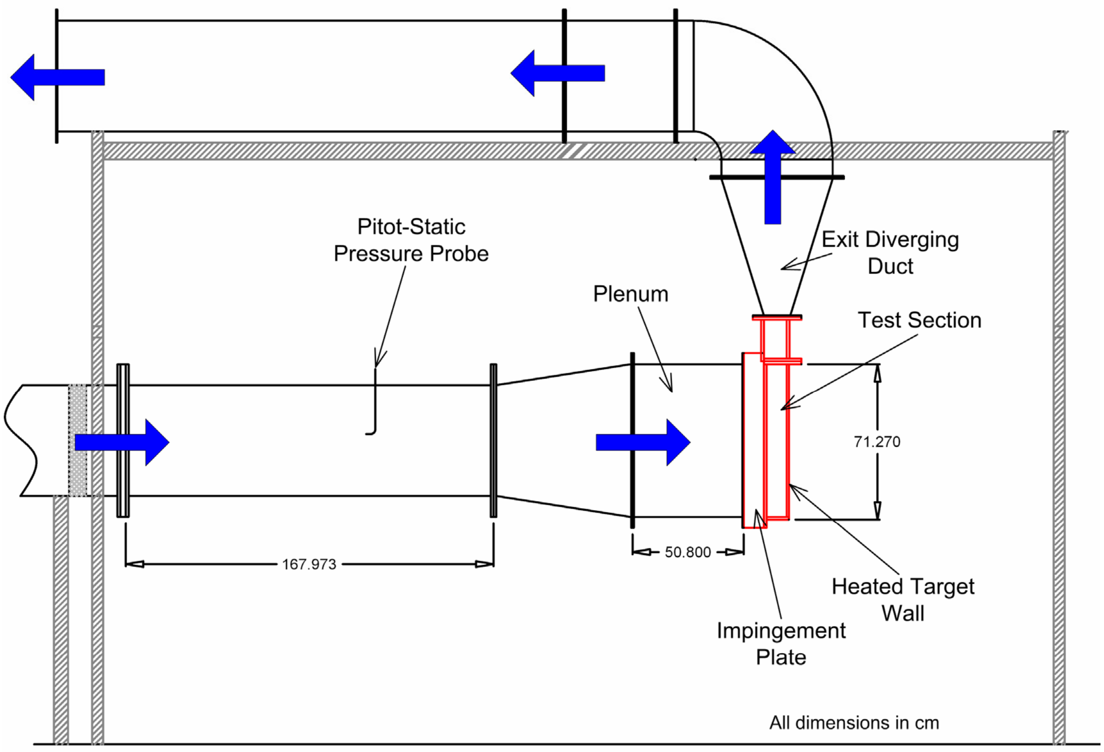

Fig. 5.1 Layout of the flow loop along with the test section

pressure differential of 55kPa and a volume flow rate of 6.2m^3/s. The pressure and volume flow rate in the channel could be varied by a frequency controller operating between 0 to 60Hz. The flow was supplied to the jet plate through an inlet pipe and a plenum as shown in Fig. 5.1. The flow entered the jet plate holes, impinged on the target wall and exited through one side only. The total flow rate in the loop was controlled to correspond to pre-determined Reynolds numbers based on the average jet hole diameter for each jet plate. The nominal Reynolds numbers tested, based on the average jet hole diameter were 50,000, 150,000, 250,000, 350,000 and 450,000. Average inlet velocity was measured upstream of the plenum by traversing a pitot-static tube through 6 radial points from the centerline. Assuming the flow is radially symmetric in the inlet supply pipe, the average inlet velocity was found to be equivalent to 0.89 times the centerline velocity upstream of the plenum.

Two jet plates with different hole arrangements were used. Figure 5.2 shows both the test plate drawings. Jet plate 1 has 5 rows of jet holes while jet plate 2 had 6 rows. For jet plate 1, the first two upstream rows contained 4 holes while the next three were composed of just 3 jet holes. The first upstream row was inclined at 45^o to the target wall and was cut with a chamfer

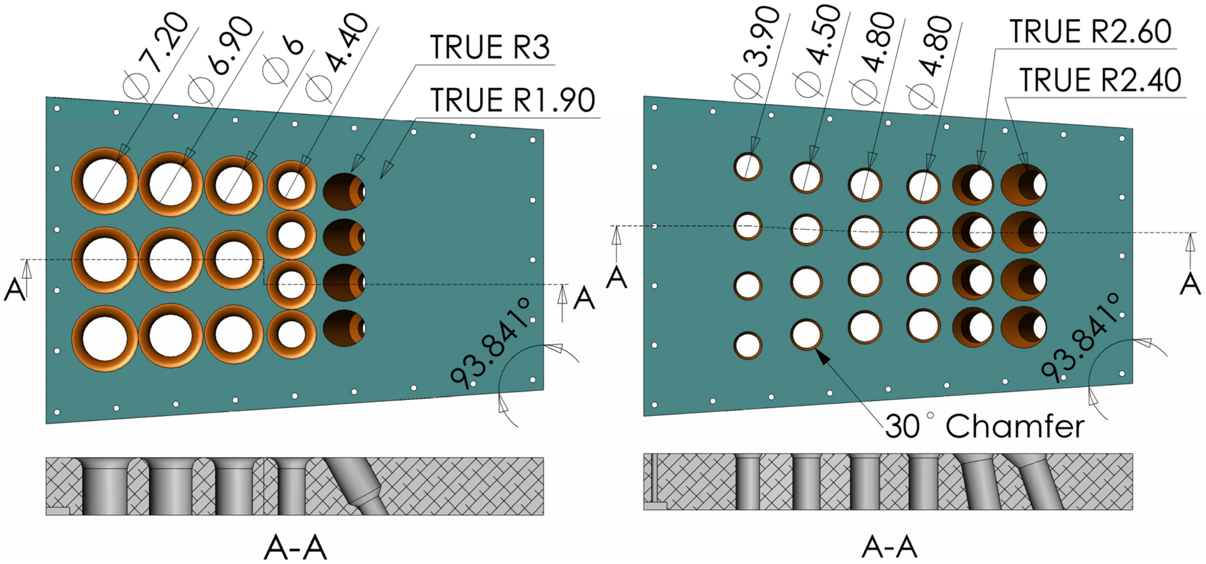

Jet Plate 1 ***Jet Plate 2***

Fig. 5.2 Schematic of the two impingement jet plates

on the top edge to allow smooth entry to the mainstream flow. The other holes were provided with a fillet radius. The jet hole diameters progressively increased from 3.8cm for the upstream row to 7.2cm for the last row with all holes in the same holes drilled at the same diameter. The average streamwise spacing between all holes was around 2.7 times the average jet diameter while the average spanwise spacing was 1.86 times the average jet diameter. The average length to diameter ratio and jet-to-target wall spacing to diameter ratio for all holes was 1.75 and 2 respectively. Figure 5.2 also shows a schematic of jet plate 2. Six rows of holes with 4 holes in each row formed the jet hole matrix. The first two upstream hole rows were inclined to the target wall 70.3^{o} and 79.8^{o} respectively while the other 4 rows impinged normally on the target surface. All holes were provided with a chamfer on its upstream edge to prevent the formation of a vena contracta immediately downstream of hole entrance. The first 4 upstream hole rows had a diameter of 4.8cm and it decreased to 3.9cm to the last row. All holes in a row had the same diameter similar to jet plate 1. The average streamwise spacing between all holes was around 2.08 times the average jet diameter while the average spanwise spacing was 1.8 times the average jet diameter. The average length to diameter ratio and jet-to-target wall spacing to diameter ratio for all holes was 2 and 2.25 respectively. Jet plate 1 is designed to minimize the effect of downstream crossflow by providing larger downstream holes resulting in larger mass flow. However, jet plate 2 is optimized to provide uniform mass flow in each streamwise region

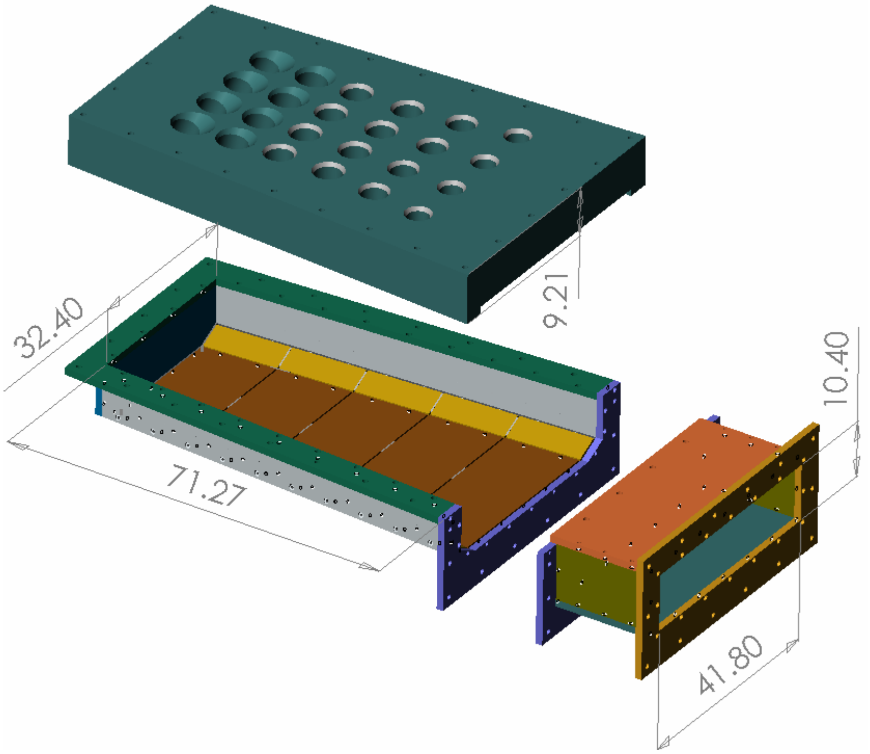

Fig. 5.3 Exploded view of impingement test section

along the test section. The downstream jets are arranged inline with the upstream jets to minimize jet deflection from crossflow.

A 3-dimensional pictorial representation of the test section is shown in Fig. 5.3. The jets emerging from the jet plates impinged on a target wall and two inclined walls located on the spanwise sides of the target wall. The inclined walls were angled at 27^o to the target wall. The flow exited the test section along only one direction. To decrease the momentum of the crossflow generated from the spent jets, the test section was designed to expand in the streamwise direction by an angle of 3.8^o on each side resulting in a trapezoidal shape. Hence, deflection of the impinging jets is minimized. In addition to the effect of jet plates, four different target walls were tested including the smooth target wall. Figure 5.4 shows the turbulator geometries studied for target wall region 1. Turbulated target walls with streamwise riblets, dimples and short pins were tested. Streamwise riblets 4mm tall and 3mm wide were machined on the target wall along the cross flow direction. Spherical dimples similar to those studied in the high flow channel experiments for case 1 were used and were scaled down by 0.667 times. About 420 dimples with filleted edges were machined on the target surface. Another target wall with short pins with a diameter and height of 4mm was fabricated to test enhancement due to the pins. The height of both pins and riblets was maintained to be same for fair comparison. Around 4350 pins were machined on the entire target wall.

5.3. MEASUREMENT THEORY

A steady state heat transfer measurement technique was used to determine the heat transfer. The target wall and inclined walls were each made of 5 equally spaced copper regions. A 3.2mm rubber gasket isolated the regions from each other and the unheated test section walls. Each region on the target wall was fitted with 6 T-type thermocouples to record the wall temperature whereas each inclined wall region was fitted with 2 thermocouples. The thermocouples were inserted on the underside of the copper regions through tiny holes and grooves to allow passage for the thermocouple wires. The thermocouples were connected to a computer controlled data acquisition system. Heat was applied to the target wall and the two inclined walls through individual heaters and was controlled using individual auto-transformers. Due to the high wattage required for high Reynolds numbers, three phase flexible wire heaters, connected to 408V, 50A three phase supply line via individual auto-transformers, were used to generate the required heat to raise the wall temperature. The heaters used generate uniform heat flux over their entire area resulting in a uniform wall heat flux boundary condition on the walls. The total heat input for a turbulated target wall at the highest flow Reynolds number was around 2kW. During testing, it was ensured that the heat supplied from both heaters on the test wall was identical. The heat supplied was obtained by measuring the phase voltage, $V_{ph,i}$ and phase current, $I_{ph,i}$ for each phase using multimeters. The input heat flux, q''_{heater} supplied by a single three phase heater is given by

$$q''_{heater} = \sum_{i=1}^{3} V_{ph,i} I_{ph,i} \Big/ A_{heater} \tag{5.1}$$

The heaters were stuck on the outer surface of the copper regions using a high temperature adhesive. All three walls were covered with fiber-glass insulation 4cm thick to minimize extraneous heat loss. Data is corrected for this heat lost due to conduction and radiation to the surroundings. The amount of heat lost, q_{loss} was calculated by supplying heat to the target and inclined walls under no-flow conditions with the same temperature difference maintained between the walls and inlet air as in the actual tests. The heat loss which is a function of this

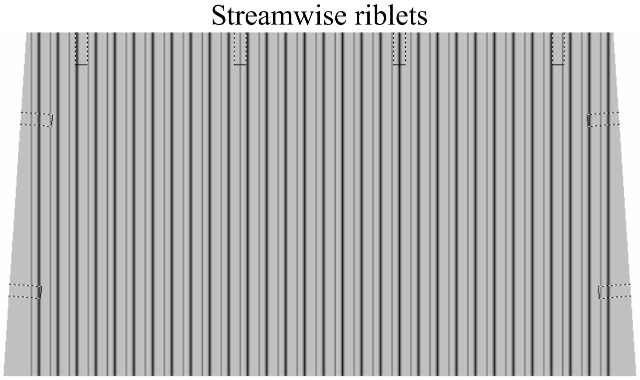

Fig. 5.3 Exploded

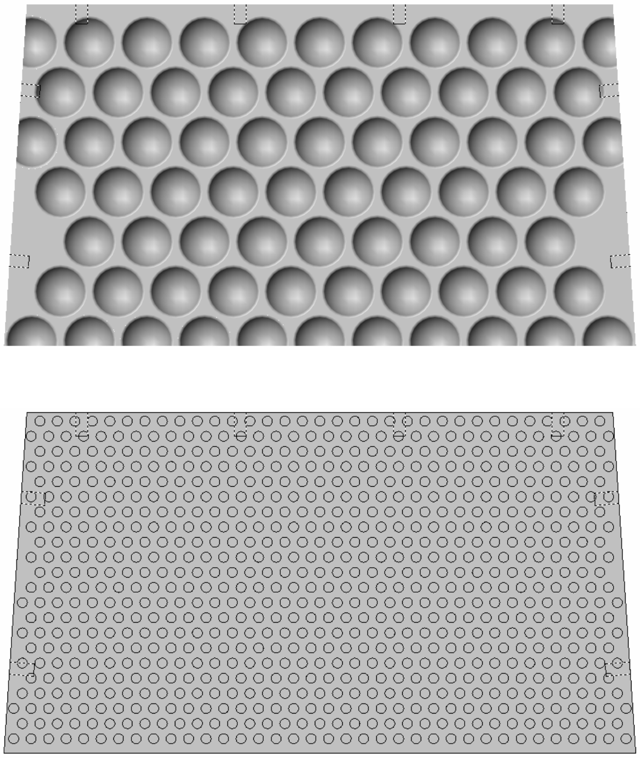

Fig. 5.4 Turbulated target wall design

temperature difference was determined for a range of temperatures and the resulting heat loss data was curve fitted and incorporated in the heat transfer calculation program. The heat transfer coefficient *h* for each region, dictated by Newton's Law for convective heat transfer is given by

$$h_i = \frac{q''}{T_{w,i} - T_{\infty,i}} = \frac{q''_{heater} - q''_{loss}}{T_{w,i} - T_{aw,i}} \tag{5.2}$$

where *q"* is the net convective heat flux from the surface after accounting for the heat loss through the insulation. Steady state was obtained within 90 minutes after applying heat to the test section. The amount of heat applied was controlled such that the steady-state wall temperature T_w was maintained around 20°C higher than the inlet air temperature. High wall temperatures result in larger heat losses whereas low wall temperatures result in higher uncertainty in the data as the sensitivity of the heat transfer coefficient given in Eq. (5.2) at low temperature difference increases. A 20°C temperature difference ensured an optimum balance with low relative uncertainties as well as low heat losses. The adiabatic wall temperature, T_{aw} in Eq. (5.2) was measured for an unheated surface but under the same flow conditions as the actual test. The adiabatic wall temperature was thus measured prior to the application of heat to the channel walls. The adiabatic wall temperature is equivalent to the recovery temperature of air and it includes the effect of viscous heating due to eddy dissipation at high Mach numbers. The effect of bulk temperature increase of the mainstream air due to the application of heat particularly near the test section exit was not accounted for. The heat transfer coefficient was expressed in terms of the Nusselt number *Nu* and was calculated using Eq. (5.3)

$$Nu = \frac{hD_h}{k_{air}} \tag{5.3}$$

Streamwise static pressure measurements along the test section length were performed though pressure taps at 10 streamwise locations spaced 6.3cm apart. Pressure taps were drilled along both the side walls of the test section. Static and total pressure measurement in the plenum was performed using a pitot-static probe placed 30.5cm upstream of the jet plate. A pitot-static probe was also placed 3cm downstream of the test section exit. The pressure taps were connected to a calibrated pressure transducer to record the static pressures. The loss coefficient based on the overall pressure drop between the plenum and the test section exit and the average exit flow velocity is expressed by Eq. (5.5).

$$K = \frac{\Delta p}{\rho \overline{V}_{exit}^{\,2} / 2} \tag{5.4}$$

Uncertainty calculations were performed based on a confidence level of 95% and were based on the uncertainty analysis method of Coleman and Steele [41]. Lower Reynolds numbers gave higher uncertainties in the heat transfer coefficients due to lower magnitudes. Highest relative uncertainties for Nu were around 11% for Re = 50,000. Relative uncertainties in flow measurement and loss coefficient measurement were around 6% and 7.5% respectively.

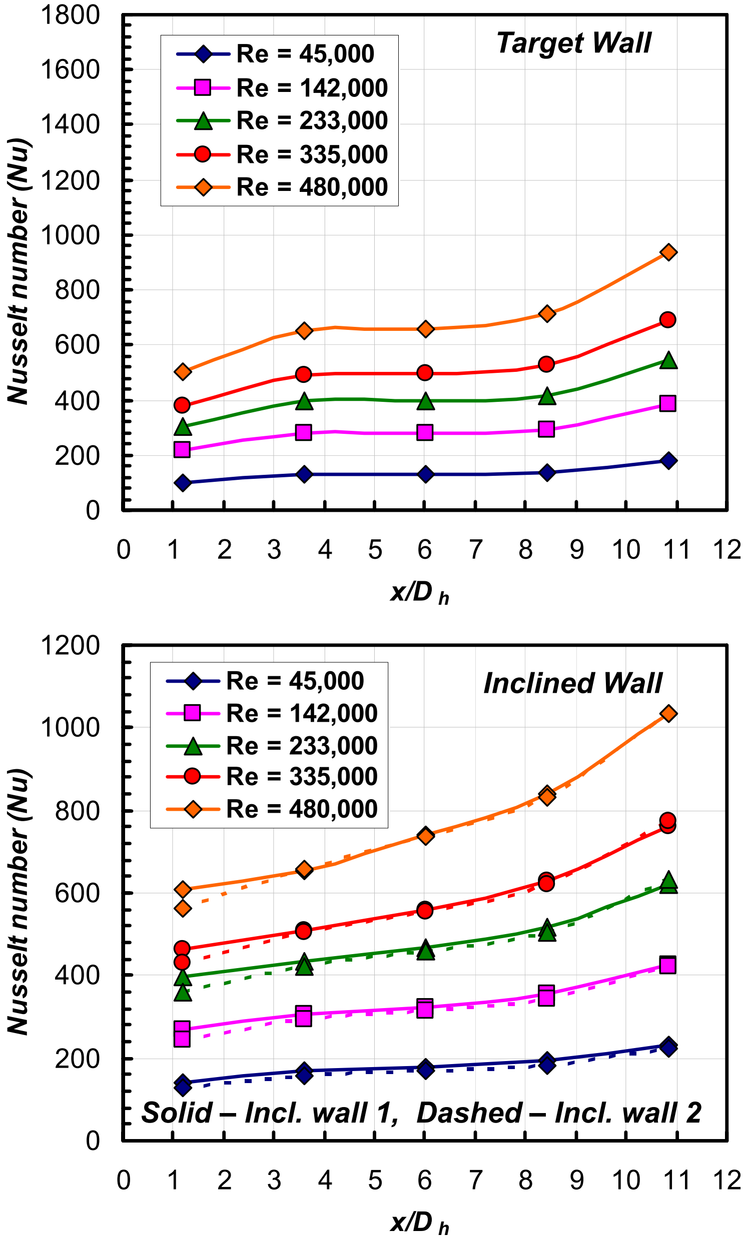

Fig. 5.5 Nusselt number distributions for all regions on smooth target wall with jet plate 1

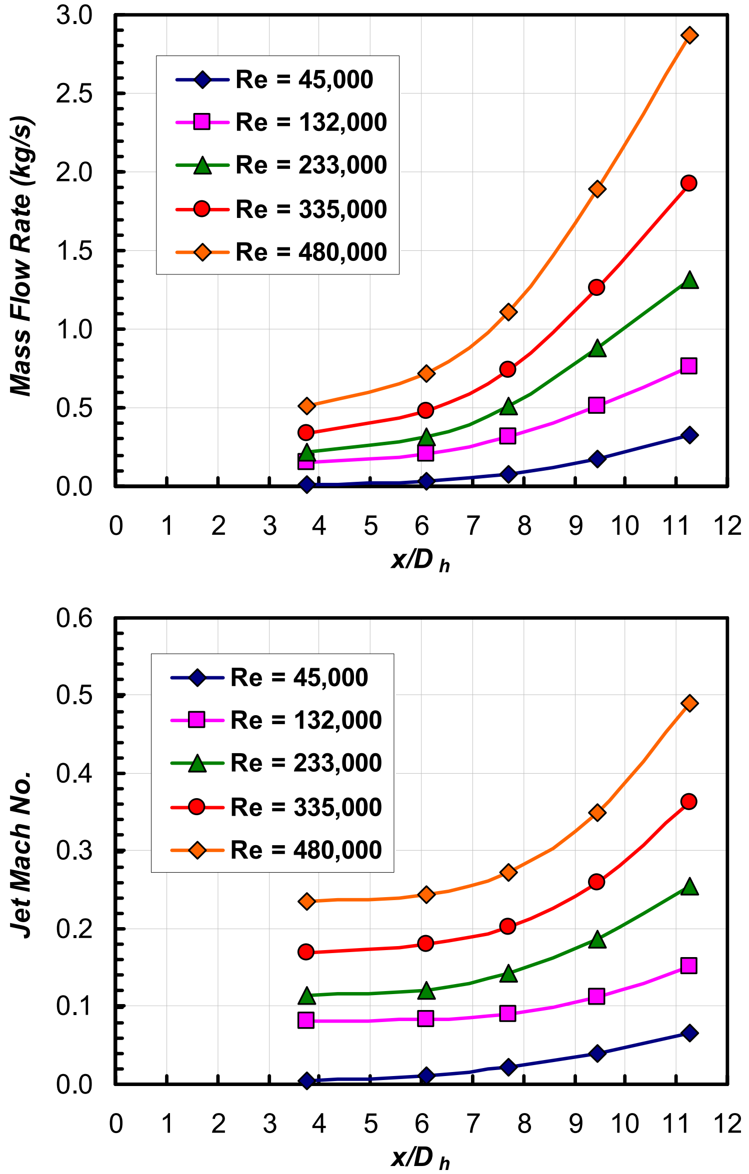

Fig. 5.6 Row-wise mass flow and jet Mach number distributions through streamwise jet rows for jet plate 1

5.4. RESULTS AND DISCUSSION

5.4.1. Heat Transfer for Smooth Target Wall – Effect of Jet Plate

Figure 5.5 shows the regional Nusselt number distributions on the smooth target wall and the two inclined walls for jet plate 1. Heat transfer on region 1 on the target wall is very low due to lack of jets impinging in this region. The Nusselt number increases substantially downstream with highest magnitudes for region 5. The Nusselt number for region 1 is about 45% lower than that for region 5. For jet plate 1, maximum mass flow occurs through the last jet hole row directly above region 5. The mass flow distribution through each jet hole row as well as the jet mach number are shown in Fig. 5.6 along the dimensionless streamwise distance. The mass flow distribution was obtained from the measured pressure drop between the static pressures measured upstream of the jet plate in the plenum and at the corresponding streamwise hole location inside the test section measured from the 10 pressure taps located on each side wall. A constant discharge coefficient was assumed for all the jet holes. It must be noted that the discharge coefficient depends on the hole geometry as well as the flow conditions. However, the hole geometry for all hole rows as well as the hole flow conditions are different in this case. As a result, the mass flow as well as the Mach number distributions obtained from the pressure drop and the constant discharge coefficient assumption provides only a qualitative idea of the actual flow through all holes.

The regional heat transfer distribution is similar to the jet Mach number distribution. Due to the large hole diameters and highest pressure drop across the holes in the last hole row, the mass flow and hole jet velocities are highest for this row resulting in high heat transfer for the downstream region. A peak mach number of 0.5 can be observed for the holes in the last row for the highest Reynolds number. Mass flow rate for the last hole row is almost 6 times that for the first row for the highest Reynolds number. The heat transfer increases with increasing jet hole Reynolds numbers due to higher impinging jet momentum. As expected, heat transfer distribution on the two inclined walls is almost same at all Reynolds numbers due to its symmetric design. Heat transfer on the target wall for regions 2, 3 and 4 is similar due to similar jet velocities for the first 3 rows whereas a continual increase in heat transfer in observed on the inclined walls. Heat transfer levels on the target wall are lower than those on the inclined walls by about 10 to 20% with the percent decrease more significant at lower Reynolds numbers. The closely spaced jets near the center span of the test section may hinder the movement of crossflow pushing it towards the sides of the test section. Thus, the inclined walls may be exposed to very high streamwise velocities from the crossflow raising their heat transfer coefficients. The steady increase in heat transfer in the streamwise direction on the inclined walls may be due to increasing mass flow of spent air.

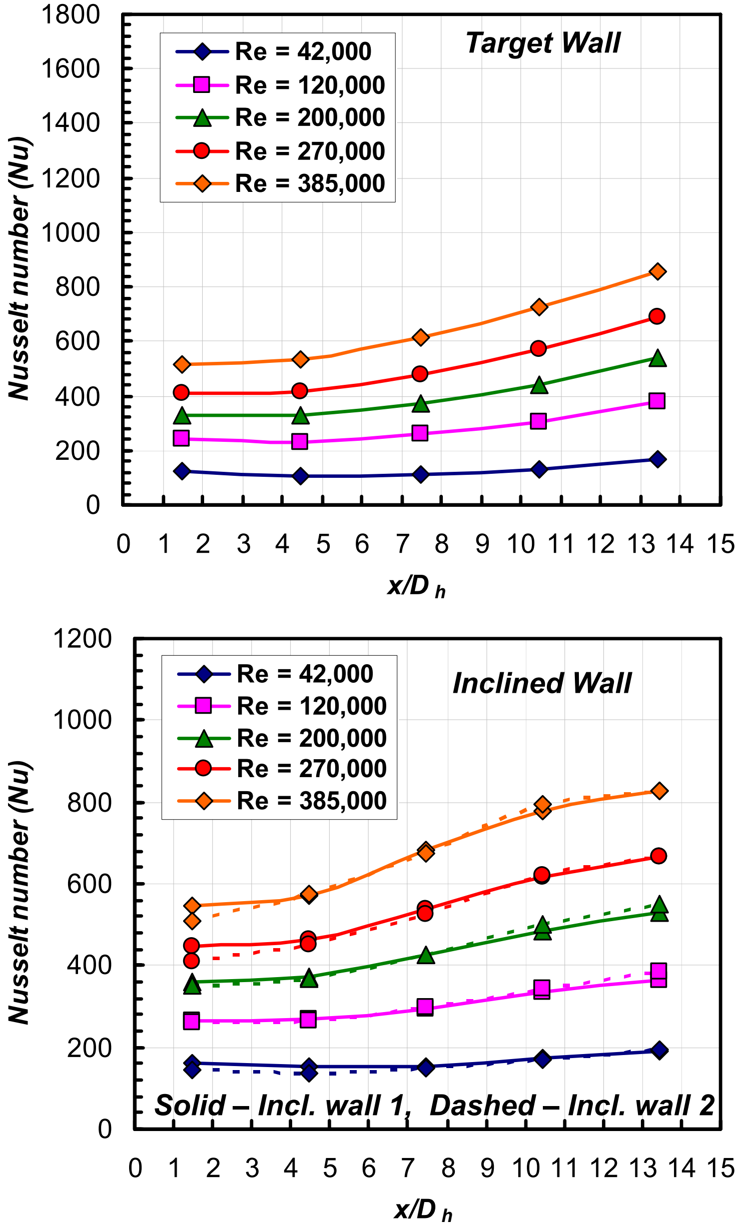

Fig. 5.7 Nusselt number distributions for all regions on smooth target wall with jet plate 2

Figure 5.7 shows the regional Nusselt number distribution for jet plate 2 for the target and inclined walls. The regional Nusselt numbers for jet plate 2 increase with increasing Reynolds number as well as with increasing streamwise distance similar to that observed for jet plate 1. The Nusselt number for region 1 is about 40% lower than that for region 5 resulting in a

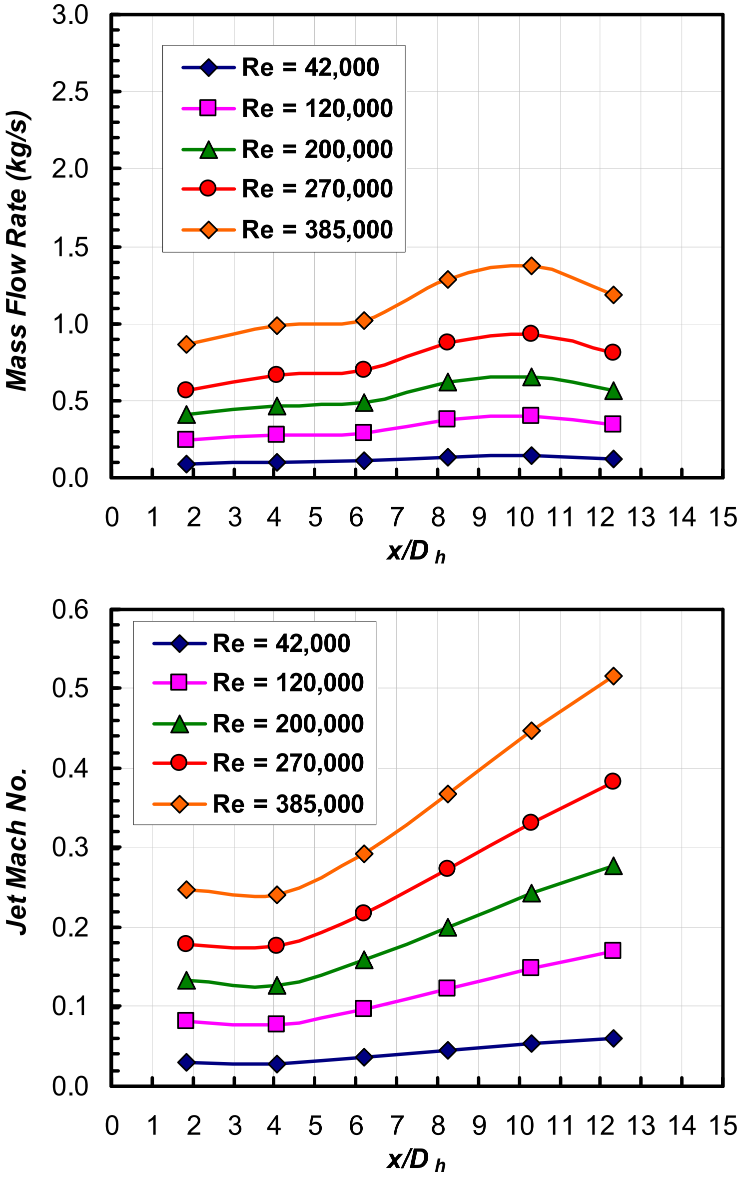

Fig. 5.8 Row-wise mass flow and jet Mach number distributions through streamwise jet rows for jet plate 2

relatively uniform distribution as compared to jet plate 1. Figure 5.8 shows the streamwise mass flow and jet Mach number distribution through the jet hole rows for all Reynolds numbers. The mass flow distribution is much more uniform as compared to that for jet plate 1. Maximum mass flow occurs for the 5th jet hole row which is only 1.5 times higher than the lowest mass flow for the first hole row. However, the jet hole velocities show a much sharper gradient due to smaller jet diameters near the test section exit. The regional Nusselt number distribution follows the same trends as the jet Mach number distribution. The coupled effect of large crossflow and jet impingement further helps in increasing the downstream heat transfer. Jet impingement from the first two upstream rows results in higher heat transfer for the first two regions than that observed for jet plate 1. This causes the average magnitudes for jet plate 2 to be higher than those for jet plate 1. It should be noted that the Nusselt number magnitudes in Fig. 5.5 for jet plate 1 and Fig. 5.7 for jet plate 2 cannot be compared directly as the corresponding jet Reynolds are higher for jet plate 1. Average heat transfer for all regions for jet plate 1 is about 14% lower than jet plate 2 for Re ~ 400,000.

Figure 5.7 also shows the Nusselt number distribution for the inclined walls. The heat transfer distributions for both inclined walls show similar trends and magnitudes and are comparable to those for jet plate 1 in Fig. 5.5. Also, heat transfer on the inclined walls is about 5 to 10% higher than that on the target walls due to crossflow effect.

5.4.2. Heat Transfer for Turbulated Target Walls

The smooth target wall used in the previous two tests was replaced with three turbulated target walls with riblets, short pins and spherical dimples. Jet plate 2 which gave higher heat transfer for the smooth target wall was used to impinge air on the turbulated target walls. The smooth target wall thus acts as a reference case for comparison. Figure 5.9 shows the regional Nusselt number distribution for the target wall with streamwise riblets. The trends observed for both the target and inclined walls are similar to that observed for the smooth wall cases in Fig. 5.7. However, the magnitudes are much higher. Peak Nusselt number for Re = 430,000 is about 1600. The short riblets help in increasing the surface area in contact with the flow. Also, they may promote the formation of secondary vortices between adjacent riblets which may give high heat transfer coefficients. Heat transfer on the smooth inclined walls however is not affected by the presence of a turbulated target wall. The heat transfer trends as well as magnitudes are similar to the smooth target wall case. A slight dip in heat transfer is observed for the last region which could be due to lower crossflow velocities from flow expansion.

Figures 5.10 and 5.11 show the regional heat transfer distribution for the target wall with short pins and spherical dimples respectively. The heat transfer trends are similar to the smooth target wall and target wall with ribs with the smooth inclined walls also showing the same trends. However, the Nusselt number magnitudes are much higher for the target wall with short pins.

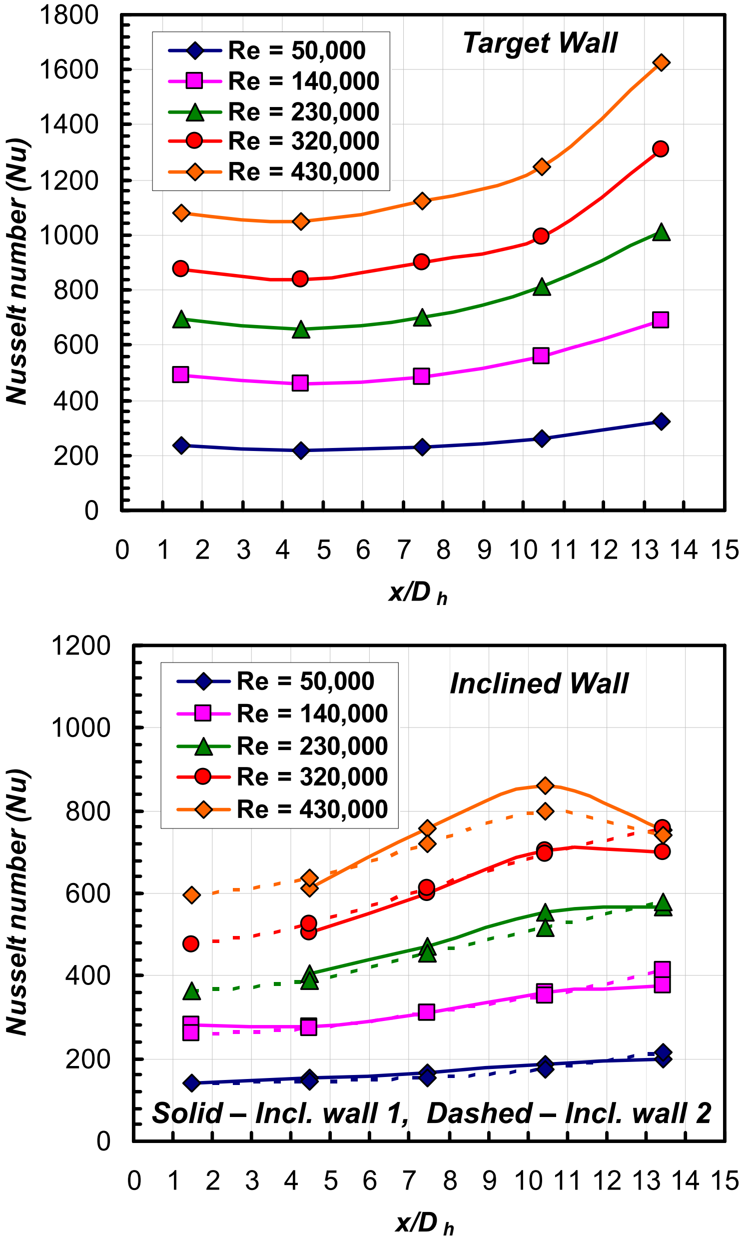

Fig. 5.9 Nusselt number distributions for all regions on target wall with riblets and jet plate 2

Figure 5.12 compares the overall average Nusselt number distributions for all turbulated target walls as well as smooth target walls. It can be clearly observed that heat transfer for the short pins is highest followed by the riblets and dimples in that order. Surface area from short pins is about 2.11 times the smooth target wall. The staggered arrays of short pins also create additional

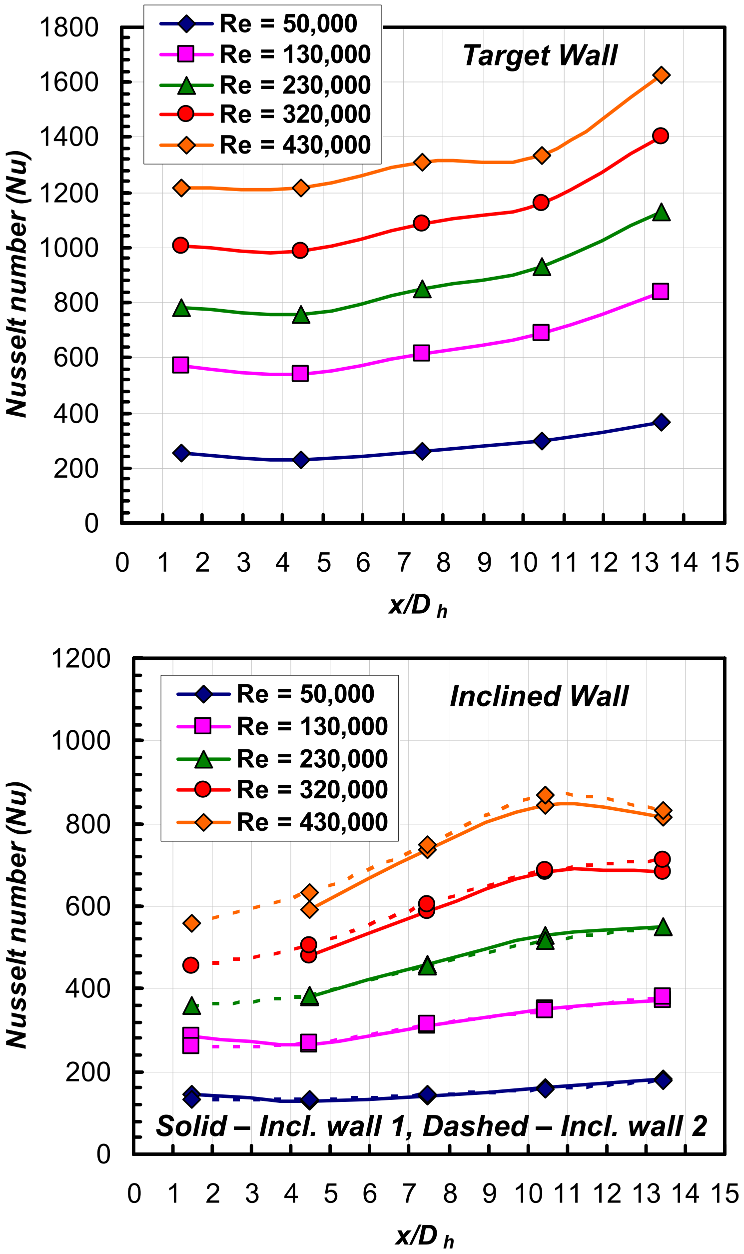

Fig. 5.10 Nusselt number distributions for all regions on target wall with short pins and jet plate 2

secondary flow vortices which may be stronger in intensity than that for either the riblets or dimples. The heat transfer enhancement for short pins is about 2 times as observed in Fig. 5.13. For the target wall with riblets, the surface area enlargement factor is 2.16 similar to short pins. However, the overall average heat transfer is slightly lower than pins resulting in an average

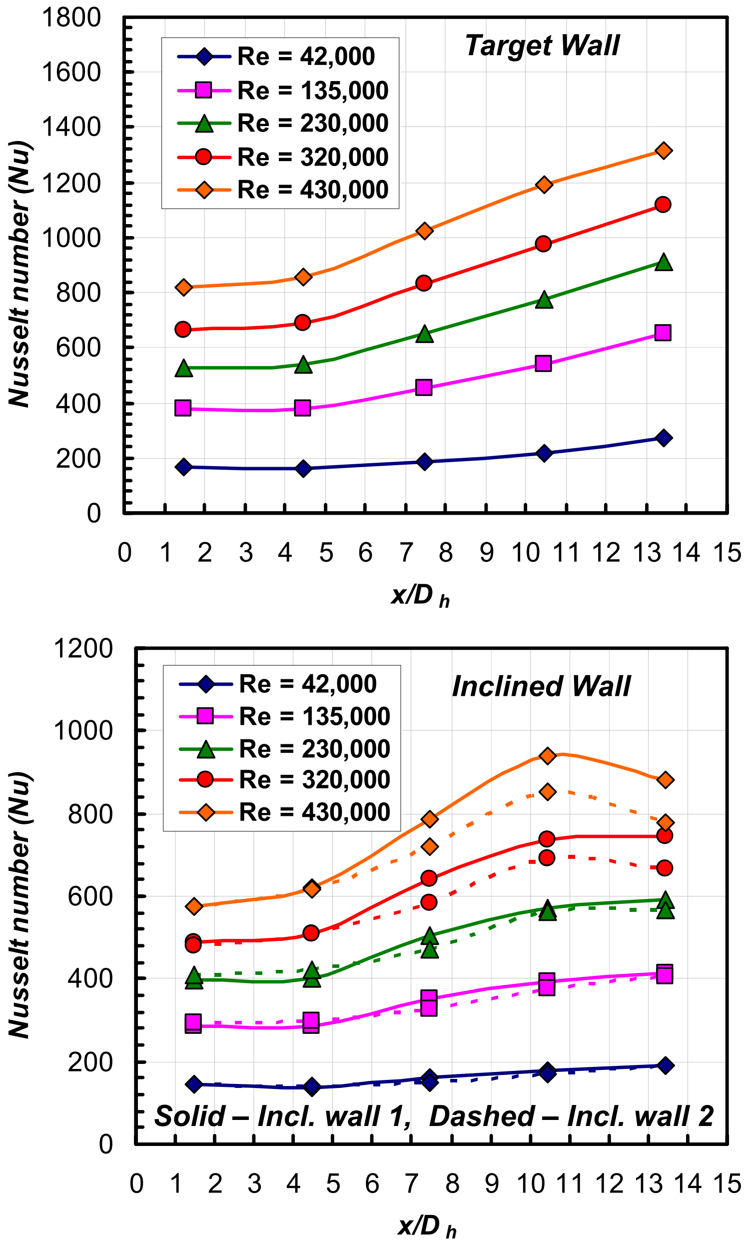

Fig. 5.11 Nusselt number distributions for all regions on target wall with dimples and jet plate 2

enhancement of about 1.72. Minimal surface enlargement is obtained from spherical dimples with an area enlargement factor of 1.27 and as a result, shows the lowest heat transfer enhancement. It should be noted that the dimpled target wall provides an enhancement of about 1.5 times over the smooth wall which is more than its surface enlargement factor. This indicates

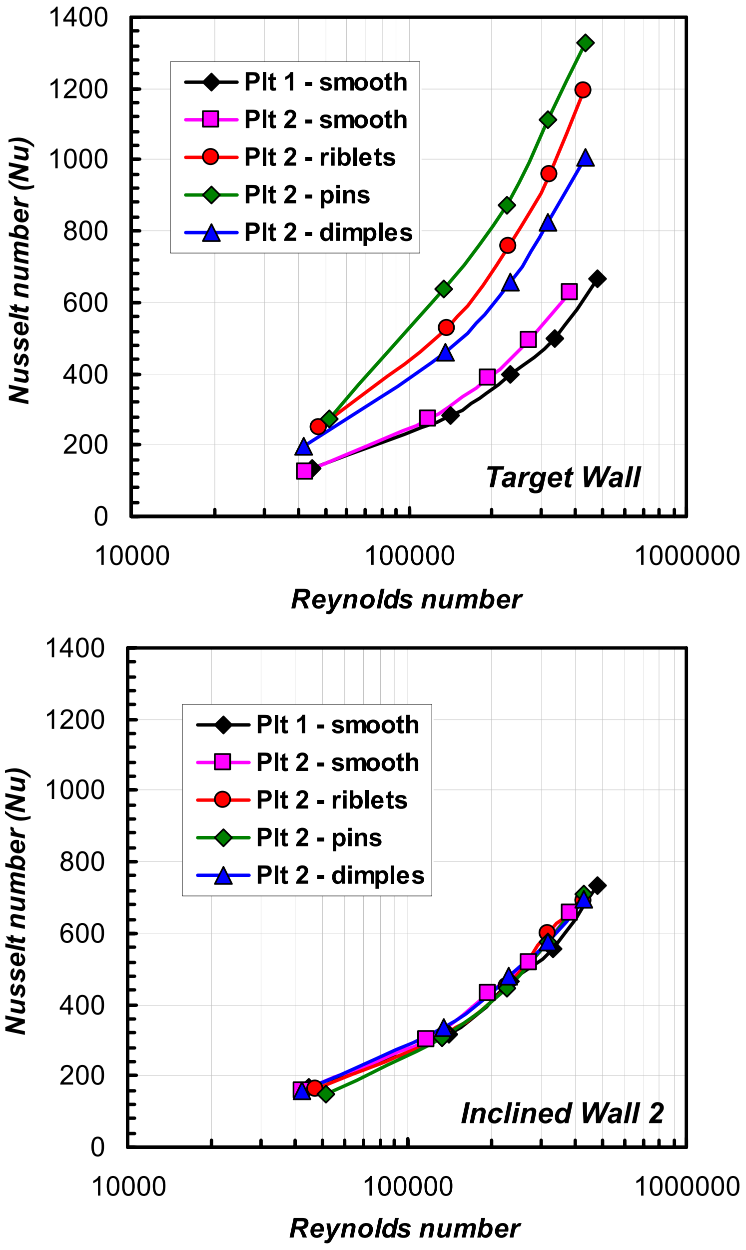

Fig. 5.12 Comparison of average Nusselt numbers for all regions between all cases

that dimples provide the best enhancement with lowest area enlargement. Overall, enhancement from the turbulated target walls decreases with increasing Reynolds numbers.

Figure 5.12 also compares the overall averaged heat transfer for the inclined wall 2 for all cases. It can be clearly observed that the presence of turbulators does not have a major impact on heat transfer from the smooth inclined wall with all cases showing similar levels. The flow on the inclined wall is dominated by the crossflow whose velocity does not change for the same Reynolds numbers and hence is not affected by the turbulated target walls.

5.4.3. Loss Coefficients

Figure 5.14 compares the loss coefficients obtained between the plenum and the exit of the test section for all cases. The loss coefficients for jet plate 1 are much higher than jet plate 2 at low Reynolds numbers but decrease rapidly to approach jet plate 2 values at high Reynolds numbers. Loss coefficient comparisons are also made for the three turbulators geometries employed on the target wall. The resulting curves obtained for the three geometries are similar to that for the smooth target wall. This is mainly due to the large pressure drop occurring over the jet plate which is much higher than the pressure drop introduced by adding turbulators geometries on the surface. As a result, all four cases for jet plate 2 tend to fall into one line.

5.5. CONCLUSIONS

Experiments were performed to investigate heat transfer and pressure losses in an impingement test section with closely spaced jet arrays. Two jet plate designs were investigated along with three turbulator geometries. Experiments were performed for a range of Reynolds numbers upto 450,000. The main conclusions that can be drawn from this study are presented below.

1. A jet plate design with increasing hole diameters in the streamwise direction gives relatively more gradients in the heat transfer distribution with lower magnitudes than a jet plate design with decreasing hole diameters.
2. Short pins give the highest heat transfer for all Reynolds numbers while riblets give the highest surface area enhancement.
3. Dimples provide enhancement larger than their area enlargement ratio while riblets give enhancement lower than their area enlargement ratio.
4. The second jet plate with decreasing hole diameters in the downstream direction provides lower losses.
5. Pressure losses through the jet plate dwarf those introduced by the addition of turbulators.

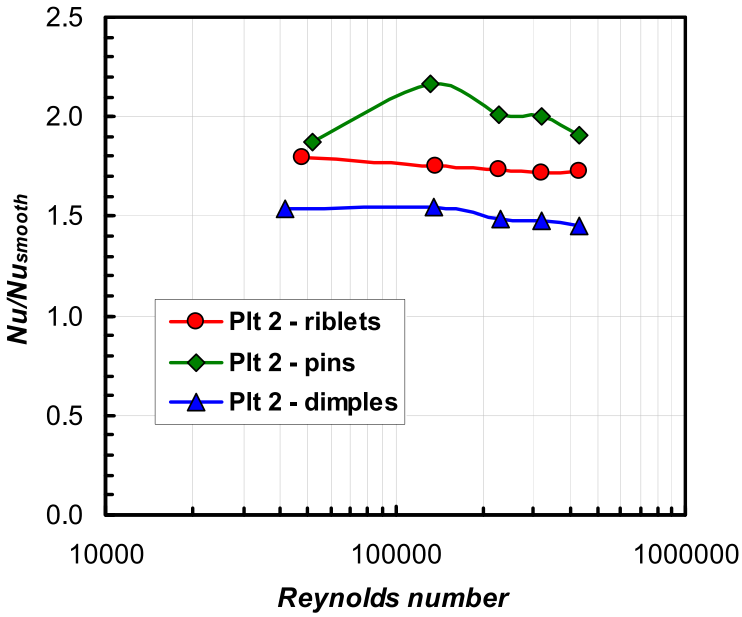

Fig. 5.13 Nusselt number enhancement from turbulated target walls compared to smooth walls

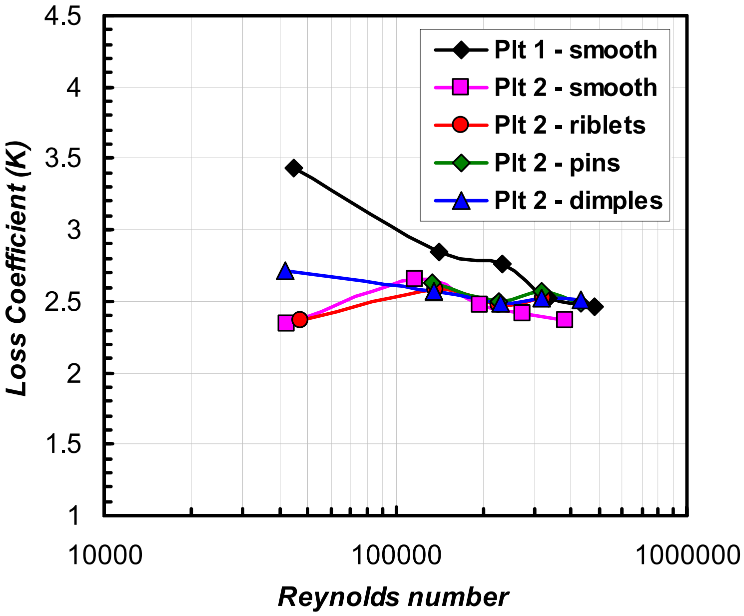

Fig. 5.14 Comparison of loss coefficients from plenum to test section exit between all cases

6. SUMMARY

Experimental investigations were performed for four different test sections involving the study of film cooling and heat transfer. Film cooling effectiveness results were obtained for a gas turbine blade tip as well on the blade span. A new measurement technique known as Pressure Sensitive Paint (PSP) technique was employed to study this phenomenon. The PSP technique is free from errors related to heat conduction frequently encountered in other heat transfer measurement techniques. As a result, clear coolant traces were observed with accurate data near the ejection holes. Tests were performed using PSP in linear cascades with relatively large inlet Mach numbers. Parametric investigations were performed to optimize the blade film coverage and innovative ideas were tested. The effect of blowing ratio, cavity depth, cutback squealer and film cooling hole arrangement was investigated for the blade tip whereas the effect of blowing ratio, unsteady wake, hole row ejection and film cooling superposition was tested on the blade span.

Heat transfer and pressure loss measurements were also performed in a high aspect ratio channel and for jet array impingement under very large Reynolds numbers. These tests provide valuable insight in heat transfer behavior at high flow conditions as very limited data exists in open literature in this area. The channel flow results were compared with available correlations to ensure validity of test data. The heat transfer enhancement from artificial roughness introduced on the test wall was also investigated. Test results indicate a continually decreasing enhancement level for larger Reynolds numbers for all turbulator geometries tested.

REFERENCES

[1] Han, J.C., Dutta, S., and Ekkad, S. V., 2000, *Gas Turbine Heat Transfer and Cooling Technology*, Taylor & Francis, New York.

[2] Kim, Y.W., and Metzger, D.E., 1995, “Heat Transfer and Effectiveness on Film Cooled Turbine Blade Tip Model,” ASME J. of Turbomachinery, **117** (1), pp. 12-21.

[3] Kim, Y.W., Downs, J.P., Soechting, F.O., Abdel-Messeh, W., Steuber, G.D., and Tanrikut, S., 1995, “A Summary of the Cooled Turbine Blade Tip Heat Transfer and Film Effectiveness Investigations Performed by Dr. D. E. Metzger,” ASME J. of Turbomachinery, **117** (1), pp. 1-11.

[4] Kwak, J.S., and Han, J.C., 2002, “Heat Transfer Coefficient and Film-cooling Effectiveness on a Gas Turbine Blade Tip,” ASME Paper GT-2002-30194.

[5] Kwak, J.S., and Han, J.C., 2002, “Heat Transfer Coefficient and Film-Cooling Effectiveness on the Squealer Tip of a Gas Turbine Blade,” ASME Paper GT-2002-30555.

[6] Ahn, J., Mhetras, S.P., and Han, J.C., 2004, “Film-Cooling Effectiveness on a Gas Turbine Blade Tip,” ASME Paper GT-2004-53249.

[7] Christophel, J.R., Thole, K.A., and Cunha, F.J., 2004, “Cooling the Tip of a Turbine Blade Using Pressure Side Holes – Part 1: Adiabatic Effectiveness Measurements,” ASME Paper GT-2004-53251.

[8] Christophel, J.R., Thole, K.A., and Cunha, F.J., 2004, “Cooling the Tip of a Turbine Blade Using Pressure Side Holes – Part 2: Heat Transfer Measurements,” ASME Paper GT-2004-53254.

[9] Mhetras, S.P., Yang, H., Gao, Z., and Han, J.C., 2005, “Film-Cooling Effectiveness On Squealer Rim Walls And Squealer Cavity Floor Of A Gas Turbine Blade Tip Using Pressure Sensitive Paint,” ASME Paper GT-2005-68387.

[10] Metzger, D.E., Dunn, M.G., and Hah, C., 1991, “Turbine Tip and Shroud Heat Transfer,” ASME J. of Turbomachinery, **113** (3), pp. 502-507.

[11] Dunn, M.G., and Haldeman, C.W., 2000, “Time-Averaged Heat Flux for a Recessed Tip, Lip, and Platform of a Transonic Turbine Blade,” ASME J. Turbomachinery, **122** (4), pp. 692-697.

[12] Rhee, D., Cho, H.H., 2006, “Local Heat/Mass Transfer Characteristics on a Rotating Blade with Flat Tip in a Low Speed Annular Cascade – Part I: Near Tip Surface,” ASME J. of Turbomachinery, **128** (1), pp. 96-109.

[13] Rhee, D., Cho, H.H., 2006, "Local Heat/Mass Transfer Characteristics on a Rotating Blade with Flat Tip in a Low Speed Annular Cascade – Part II: Tip and Shroud," ASME J. of Turbomachinery, **128** (1), pp. 110-119.

[14] Yang, T.T., and Diller, T.E., 1995, "Heat Transfer and Flow for a Grooved Turbine Blade Tip in a Transonic Cascade," ASME Paper No. 95-WA/HT-29.

[15] Bunker, R.S., Bailey, J.C., and Ameri, A.A., 2000, "Heat Transfer and Flow on the First Stage Blade Tip of a Power Generation Gas Turbine: Part 1: Experimental Results," ASME J. of Turbomachinery, **122** (2), pp. 263-271.

[16] Azad, GM. S., Han, J.C., Teng, S., and Boyle, R., 2000, "Heat Transfer and Pressure Distributions on a Gas Turbine Blade Tip," ASME J. of Turbomachinery, **122** (4), pp.717-724.

[17] Azad, GM. S., Han, J.C., and Boyle, R., 2000, "Heat Transfer and Pressure Distributions on the Squealer Tip of a Gas Turbine Blade," ASME J. of Turbomachinery, **122** (4), pp.725-732.

[18] Bunker, R. S., and Bailey, J. C., 2001, "Effect of Squealer Cavity Depth and Oxidation on Turbine Blade Tip Heat Transfer," ASME Paper 2001-GT-0155.

[19] Azad, GM S., Han, J.C., Bunker, R.S., and Lee, C.P., 2002, "Effect of Squealer Geometry Arrangement on a Gas Turbine Blade Tip Heat Transfer," ASME J. of Heat Transfer, **124** (3), pp. 452-459.

[20] Kwak, J.S., Ahn, J., Han, J.C., Lee, C.P., Bunker, R.S., Boyle, R., and Gaugler, R., 2002, "Heat Transfer Coefficients on Squealer Tip and Near Tip Regions of a Gas Turbine Blade with Single or Double Squealer," ASME Paper GT-2003-38907.

[21] Kwak, J.S., and Han, J.C., 2003, "Heat Transfer Coefficient on a Gas Turbine Blade Tip and Near Tip Regions," AIAA J. of Thermophysics and Heat Transfer, **17** (3), pp. 297-303.

[22] Kwak, J.S., and Han, J.C., 2003, "Heat Transfer Coefficient on the Squealer tip and Near Squealer Tip Regions of a Gas Turbine Blade," ASME J. of Heat Transfer, **125** (4), pp.669-677.

[23] Mayle, R.E., and Metzger, D.E., 1982, "Heat Transfer at the Tip of an Unshrouded Turbine Blade," *Proc., 7th International Heat Transfer Conference*, Hemisphere Publishing Corp., New York, pp 87-92.

[24] Heyes, F.J.G., Hodson, H.P., and Dailey, G.M., 1991, "The Effect of Blade Tip Geometry on the Tip Leakage Flow in Axial Turbine Cascades," ASME Paper 91-GT-135.

[25] Teng, S., Han, J.C., and Azad, GM S., 2001, "Detailed Heat Transfer Coefficient Distributions on a Large-Scale Gas Turbine Blade Tip," ASME J. of Heat Transfer, **123** (4), pp. 803-809.

[26] Papa, M., Goldstein, R.J., and Gori, F., 2003, "Effects of Tip Geometry and Tip Clearance on the Mass/Heat Transfer From a Large-Scale Gas Turbine Blade," ASME J. of Turbomachinery, **125** (1), pp. 90-96.

[27] Jin, P., and Goldstein, R. J., 2002, “Local Mass/Heat Transfer on a Turbine Blade Tip,” ASME Paper HT-ABS-012.

[28] Jin, P., and Goldstein, R. J., 2002, “Local Mass/Heat Transfer on Turbine Blade Near-Tip Surfaces”, ASME Paper 2002-GT-30556.

[29] Saxena, V., Nasir, H., and Ekkad, S.V., 2003, “Effect of Blade Tip Geometry on Tip Flow and Heat Transfer for a Blade in a Low Speed Cascade,” ASME Paper 2003-GT-38176.

[30] Ameri, A.A., Steinthorsson, E., and Rigby, D.L., 1999, “Effects of Tip Clearance and Casing Recess on Heat Transfer and Stage Efficiency in Axial Turbines,” ASME J. of Turbomachinery, **121** (4), pp. 683-693.

[31] Ameri, A.A., and Rigby, D.L., 1999, “A Numerical Analysis of Heat Transfer and Effectiveness on Film Cooled Turbine Blade Tip Models,” NASA/CR 1999-209165.

[32] Ameri, A.A., and Bunker, R.S., 2000, “Heat Transfer and Flow on the First Stage Blade Tip of a Power Generation Gas Turbine: Part 2: Simulation Results,” ASME J of Turbomachinery, **122** (2), pp. 272-277.

[33] Yang, H., Acharya, S., Ekkad, S.V., Prakash, C., and Bunker, R.S., 2002, “Flow and Heat Transfer Predictions for a Flat-Tip Turbine Blade,” ASME Paper 2002-GT-30190.

[34] Yang, H., Acharya, S., Ekkad, S.V., Prakash, C., and Bunker, R.S., 2002, “Numerical Simulation of Flow and Heat Transfer Past a Turbine Blade with a Squealer-Tip,” ASME Paper 2002-GT-30193.

[35] Acharya, S., Yang, H., Ekkad, S.V., Prakash, C., and Bunker, R.S., 2002, “Numerical Simulation of Film Cooling on the Tip of a Gas Turbine Blade,” ASME Paper 2002-GT-30553.

[36] Hohlfeld, E.M., Christophel, J.R., Couch, E.L., and Thole, K.A., 2003, “Predictions of Cooling Flow Dirt Purge Holes along the Tip of a Turbine Blade,” ASME Paper 2003-GT-38251.

[37] Yang, H., Chen, H.C., Han, J.C., 2004, “Numerical Prediction of Film Cooling and Heat Transfer with Different Film Hole Arrangements on the Plane and Squealer Tip of A Gas Turbine Blade,” ASME Paper 2004-GT-53199.

[38] Halila, E.E., Lenahan, D.T., and Thomas, T.T., 1982, “Energy Efficient Engine, High Pressure Turbine Test Hardware Detailed Design Report,” NASA CR-167955.

[39] McLachlan, B., and Bell, J., 1995, “Pressure-Sensitive Paint in Aerodynamic Testing,” Exp. Therm. Fluid Sci., **10**, pp. 470–485.

[40] Wright, L.M., Gao, Z., Varvel, T.A., and Han, J.C., 2005, “Assessment of Steady State PSP, TSP and IR Measurement Techniques for Flat Plate Film Cooling,” ASME Paper HT-2005-72363.

[41] Coleman, H.W., and Steele, W.G., 1989, *Experimentation and Uncertainty Analysis for Engineers*, John Wiley & Sons, New York, pp. 47-131.

[42] Dring, R.P., Blair, M.F., and Joslyn, H.D., 1980, "An Experimental Investigation of Film Cooling on a Turbine Rotor Blade," ASME J. of Engineering for Power, **102**, pp. 81-87.

[43] Takeishi, K., Aoki, S., and Sato, T., and Tsukagoshi, K., 1992, "Film Cooling on a Gas Turbine Rotor Blade," ASME J. of Turbomachinery, **114**, pp. 828-834.

[44] Abhari, R.S. and Epstein, A.H., 1994, "An Experimental Study of Film Cooling in a Rotating Transonic Turbine," ASME J. of Turbomachinery, **116**, pp. 63-70.

[45] Nirmalan, N.V. and Hylton, L.D., 1990, "An Experimental Study of Turbine Vane Heat Transfer with Leading Edge and Downstream Film Cooling," ASME J. of Turbomachinery, **112**, pp. 477-487.

[46] Abuaf, N., Bunker, R., and Lee, C.P., 1997, "Heat Transfer and Film Cooling Effectiveness in a Linear Airfoil Cascade," ASME J. of Turbomachinery, **119**, pp. 302-309.

[47] Camci, C., and Arts, T., 1985, "Experimental Heat Transfer Investigation around the Film Cooled Leading Edge of a High Pressure Gas Turbine Rotor Blade," ASME J. of Engineering for Gas Turbines and Power, **107**, pp. 1016-1021.

[48] Camci, C., and Arts, T., 1991, "Effect of Incidence on Wall Heating Rates and Aerodynamics on a Film Cooled Transonic Turbine Blade," ASME J. of Turbomachinery, **113**, pp. 493-500.

[49] Goldstein, R.J., and Chen, H. P., 1985, "Film Cooling on a Gas Turbine Blade near the Endwall," ASME J. of Engineering for Gas Turbines and Power, **107**, pp. 117-122.

[50] Mehendale, A.B., Ekkad, S.V., and Han, J.C., 1994, "Mainstream Turbulence Effect on Film Effectiveness and Heat Transfer Coefficient of a Gas Turbine Blade with Air and CO2 Film Injection," Intl. J. of Heat and Mass Transfer, **37**, pp. 2707-2714.

[51] Ou, S., and Han, J.C., 1994, "Unsteady Wake Effect on Film Effectiveness and Heat Transfer Coefficient from a Turbine Blade with One Row of Air and CO2 Film Injection," ASME J. of Heat Transfer, **116**, pp. 921-928.

[52] Mehendale, A.B., Han, J.C., Ou, S., and Lee, C.P., 1994, "Unsteady Wake Over a Linear Turbine Blade Cascade with Air and CO2 Film Injection. Part II: Effect on Film Effectiveness and Heat Transfer Distributions," ASME J. of Turbomachinery, **110**, pp. 730-737.

[53] Ekkad S.V., Mehendale, A.B., Han, J.C., and Lee, C.P., 1997, "Combined Effect of Grid Turbulence and Unsteady Wake on Film Effectiveness and Heat Transfer Coefficient of a Gas Turbine Blade with Air and CO_2 Film Injection," ASME J. of Turbomachinery, **119**, pp. 594-600.

[54] Du, H., Han, J.C., and Ekkad, S.V., 1998, "Effect of Unsteady Wake on Detailed Heat Transfer Coefficient and Film Effectiveness Distributions for a Gas Turbine Blade," ASME J. of Turbomachinery, **120**, pp. 808-817.

[55] Ames, F.E., 1998, “Aspects of Vane Film Cooling with High Turbulence. Part I: Heat Transfer,” ASME J. of Turbomachinery, **120**, pp. 768-776.

[56] Ames, F.E., 1998, “Aspects of Vane Film Cooling with High Turbulence. Part II: Adiabatic Effectiveness,” ASME J. of Turbomachinery, **120**, pp. 776-786.

[57] Drost, U., and Bolcs, A., 1999, “Investigation of Detailed Film Cooling Effectiveness and Heat Transfer Distributions on a Gas Turbine Airfoil,” ASME J. of Turbomachinery, **121**, pp. 233-242.

[58] Garg, V.K., 1999, “Heat Transfer on a Film-Cooled Rotating Blade,” NASA/CR 1999-209301.

[59] Heidmann, J.D., Rigby, D.L., and Ameri, A.A., 1999, “A Three-Dimensional Coupled Internal/External Simulation of a Film-Cooled Turbine Vane,” NASA/CR 1999-209078.

[60] Teng, S., Sohn, D.K., and Han, J.C., 2000, “Unsteady Wake Effect on Film Temperature and Effectiveness Distributions for a Gas Turbine Blade,” ASME J. of Turbomachinery, **122**, pp. 340-347.

[61] Teng, S., and Han, J.C., 2000, “Effect of Film-Hole Shape on Turbine Blade Heat Transfer Coefficient Distribution,” AIAA-2000-1035.

[62] Takeishi, K., and Aoki, S., 2001, “Contribution of Heat Transfer to Turbine Blades and Vanes for High Temperature Industrial Gas Turbines Part 1: Film Cooling,” Annals New York Academy of Sciences, **934**, pp. 305-312.

[63] Heidmann, J.D, Lucci, B.L., and Reshotko, E., 2001, “An Experimental Study of the Effect of Wake Passing on Turbine Blade Film Cooling,” ASME J. of Turbomachinery, **123**, pp. 214-221.

[64] Furukawa, T., and Ligrani, P.M., 2002, “Transonic Film Cooling Effectiveness from Shaped Holes on a Simulated Turbine Airfoil,” AIAA J. of Thermophysics and Heat Transfer, **16** (2), pp. 228-237.

[65] Cutbirth, J.M., and Bogard, D.G., 2002, “Thermal Field and Flow Visualization within the Stagnation Region of a Film Cooled Turbine Vane,” ASME J. of Turbomachinery, **124**, pp. 200-206.

[66] Cutbirth, J.M., and Bogard, D.G., 2003, “Effect of Coolant Density Ratio on Film Cooling Performance on a Vane,” ASME Paper GT-2003-38582.

[67] Sellers, J.P., 1963, “Gaseous Film Cooling with Multiple Ejection Stations,” AIAA Journal, **1** (9), pp. 2154-2156.

[68] Choe, H., Kays, W.M., and Moffat, R.J., 1974, “The Superposition Approach to Film Cooling,” ASME Paper 74-WA/HT-27.

[69] Muska, J.F., Fish, R.W., and Suo, M., 1976, “The Additive Nature of Film Cooling from Rows of Holes,” ASME J. of Engineering for Power, **98**, pp. 457-464.

[70] Polanka, M.D., Ethridge, M.I., Cutbirth, J.M., Bogard, D.G., 2000, “Effects of Showerhead Injection on Film Cooling Effectiveness for a Downstream Row of Holes,” ASME Paper 2000-GT-240.

[71] Cutbirth, J.M., and Bogard, D.G., 2002, “Evaluation of Pressure Side Film Cooling with Flow and Thermal Field Measurements – Part 1: Showerhead Effects,” ASME J. of Turbomachinery, **124**, pp. 670-677.

[72] Cutbirth, J.M., and Bogard, D.G., 2002, “Evaluation of Pressure Side Film Cooling with Flow and Thermal Field Measurements – Part 2: Turbulence Effects,” ASME J. of Turbomachinery, **124**, pp. 678-685.

[73] Schneider, M., Parneix, S., and Wolfersdorf, J., 2003, “Effect of Showerhead Injection on Superposition of Multi-Row Pressure Side Film Cooling with Fan-Shaped Holes,” ASME Paper GT-2003-38693.

[74] Gao, Z., Wright, L.M., and Han, J.C., 2005, “Assessment of Steady State PSP and Transient IR Measurement Techniques for Leading Edge Film Cooling,” ASME Paper IMECE-2005-80146.

[75] Kays, W.M., and Crawford, M.E., 2004, *Convective Heat and Mass Transfer*, 4th Edition, McGraw Hill, New York.

[76] Chyu, M.K., Yu, Y., Ding, H., Downs, J.P., and Soechting, F.O., 1997, “Concavity Enhanced Heat Transfer in an Internal Cooling Passage,” ASME Paper 97-GT-437.

[77] Moon, H.K., O.Connell, T., and Glezer, B., 1999, “Channel Height Effect on Heat Transfer and Friction in a Dimpled Passage,” ASME Paper 99-GT-163.

[78] Mahmood, G.I., Hill, M.L., Nelson, D.L., Ligrani, P.M., Moon, H.-K., and Glezer, B., 2001, “Local Heat Transfer and Flow Structure on and above a Dimpled Surface in a Channel,” ASME J. of Turbomachinery, **123**, pp. 115-123.

[79] Moon, S.W., and Lau, S.C., 2002, “Turbulent Heat Transfer Measurements on a Wall with Concave and Cylindrical Dimples in a Square Channel,” ASME Paper GT-2002-30208.

[80] Mahmood, G.I., and Ligrani, P.M., 2002, “Heat transfer in a dimpled channel: combined influences of aspect ratio, temperature ratio, Reynolds number, and flow structure,” Intl. J. of Heat and Mass Transfer, **45**, pp. 2011-2020.

[81] Burgess, N.K., Oliviera, M.M., and Ligrani, P.M., 2003, “Nusselt Number Behavior on Deep Dimpled Surfaces within a Channel,” ASME J. of Heat Transfer, **125**, pp. 11-18.

[82] Han, J.C., 1988, “Heat Transfer and Friction Characteristics in Rectangular Channels with Rib Turbulators,” ASME J. of Heat Transfer, **110**, pp. 321-328.

[83] Han, J.C., Zhang, P., and Lee, C.P., 1991, "Augmented Heat Transfer in Square Channels with Parallel, Crossed, and V-Shaped Angled Ribs," ASME J. of Heat Transfer, **113**, pp. 590-596.

[84] Han, J.C., and Zhang, P., 1992, "High Performance Heat Transfer Ducts with Parallel Broken and V-Shaped Broken Angled Ribs," Intl. J. of Heat and Mass Transfer, **35**, pp. 513-523.

[85] Kercher, D. M., and Tabakoff, W., 1970, "Heat Transfer by a Square Array of Round Air Jets Impinging Perpendicular to a Flat Surface Including the Effect of Spent Air," ASME Journal of Engineering for Power, **92**(1), pp. 73-82.

[86] Metzger, D. E., Florscheutz, L. W., Takeuchi, D. I., Behee, R. D., and Berry, R. A., 1979, "Heat Transfer Characteristics for Inline and Staggered Arrays of Circular Jets with Crossflow of Spent Air," ASME Journal of Heat Transfer, **101**, pp. 526-531.

[87] Florscheutz, L. W., Berry, R. A., and Metzger, D. E., 1980, "Periodic Streamwise Variations of Heat Transfer Coefficients for Inline and Staggered Arrays of Circular Jets with Crossflow of Spent Air," ASME Journal of Heat Transfer, **102**, pp. 132-137.

[88] Florscheutz, L. W., Truman, C. R., and Metzger, D. E., 1981, "Streamwise Flow and Heat Transfer Distributions for Jet Array Impingement with Crossflow," ASME J. of Heat Transfer, **103**, pp. 337-342.

[89] Chakroun, W.M., Al-Fahed, S.F., and Abdel-Rehman, A.A., 1997, "Heat Transfer Augmentation for Air Jet Impinged on Rough Surface," ASME Paper No. 97-GT-436.

[90] Azad, G.M., Huang, Y., and Han, J.C., 2002, "Jet Impingement Heat Transfer on Pinned Surfaces Using a Transient Liquid Crystal Technique," Intl. J. of Rotating Machinery, **8** (3), pp. 161-173.

[91] Azad, G.M., Huang, Y., and Han, J.C., 2000, "Jet Impingement Heat Transfer on Dimpled Surfaces Using a Transient Liquid Crystal Technique," AIAA J. of Thermophysics and Heat Transfer, **14** (2), pp. 186-193.

VITA

Shantanu Mhetras received his B.E. specializing in mechanical engineering from the University of Mumbai, India in 2000. He received his M.S. degree from Texas A&M University in August 2002. He attended the Ph.D. program from August 2002 to August 2006 in the Department of Mechanical Engineering at Texas A&M University where he received a Ph.D. degree in mechanical engineering in August 2006.

Shantanu may be contacted at his parent's permanent address:

Shantanu Mhetras
c/o Prakash Mhetras
11, Barretto Apts.
Opposite Paradise Cinema
634 off L.J. Road
Mahim, Mumbai 400016, INDIA
Phone: +91 (22) 446-2470.